SOME ASPECTS OF NEUTRINO MIXING AND OSCILLATIONS

THESIS SUBMITTED TO
THE UNIVERSITY OF CALCUTTA
FOR THE DEGREE OF
DOCTOR OF PHILOSOPHY (SCIENCE)

By

SANJIB KUMAR AGARWALLA

DEPARTMENT OF PHYSICS,
UNIVERSITY OF CALCUTTA,
92, ACHARYA PRAFULLA CHANDRA ROAD,

KOLKATA 700 009, INDIA

SEPTEMBER 2008

– To My Parents –

Acknowledgements

First and foremost, I would like to express my deepest respect and most sincere gratitude to my supervisor, Professor Amitava Raychaudhuri, for introducing me into the fascinating world of neutrinos and for being an excellent teacher and a perfect guide. I convey my regards to him not only for his continuous support and patience throughout this study, which was a great comfort, but also for the new dimensions he brought into my life. Without his inspiring discussions, invaluable guidance and exact encouragement, this accomplishment would have never been fulfilled. For almost everything I know about neutrino phenomenology, I owe to him. I consider myself very fortunate to have him as my supervisor who gave me immense freedom to pursue my interests and always encouraged me to take part in various summer schools, workshops, conferences in India and abroad from the very starting point of my research career. This was quite helpful in building my confidence to discuss physics issues with other scientists which most of the times culminated into fruitful collaborations. I am greatly indebted to his assistance and understanding in matters of non-academic concern which have helped me endure some difficult times during my study period. His suggestions will always help me in moving the things ahead in my future research career.

There are no words to describe such a great honour that I have the chance to convey my sincere gratefulness to my senior collaborator Dr. Sandhya Choubey with whom I have done most of my work. She has been my constant source of inspiration for gaining grounds in research work and I strongly feel indebted to her as nothing would have been possible without her support. I would like to thank her for her close daily guidance, her patience in assisting me during the course of this work, her kindness, and her opportune encouragements. Her commitment to research and dedication to physics, and even her unique style of language and her sense of humour have all greatly influenced me.

I am very much thankful to Dr. Srubabati Goswami, my senior collaborator, with whom a part of the research work contained in this thesis was done and whose extraordinary energy and enthusiasm for physics has set a great example for me.

I would like to thank Dr. Abhijit Samanta for my first successful collaboration and for helping me regarding the use of computers. He also shared his expertise on various issues related to the ICAL@INO detector simulation with me.

Mention must be made of my senior research colleague Dr. Rathin Adhikari, who extended a helping hand both in academic and non-academic issues whenever it was necessary.

I would like to thank Dr. Subhendu Rakshit for successful collaboration and providing a friendly environment for discussing physics.

I express my gratitude to Dr. Walter Winter and Dr. Patrick Huber for providing me useful informations regarding the simulations related to long baseline neutrino experiments at various stages of this work.

I would like to express my sincere gratitude and appreciation to Professor Mina Ketan Parida who introduced me to the topic of renormalization group evolution analysis during his stay at Harish-Chandra Research Institute and provided me an opportunity to collaborate with two big names in the field of neutrino physics - Professor R. N. Mohapatra and Professor G. Rajasekaran.

The constructive suggestions and useful comments from Professor Manfred Lindner, Professor A. Smirnov, Professor G. Raffelt, Professor Andre de Gouvea, Professor Mats Lindroos, Professor Mauro Mezzetto, Professor J. J. Gomez Cadenas, Dr. Andrea Donini, Dr. Pilar Hernandez, Dr. Osamu Yasuda and Dr. Francesco Terranova helped me a lot at different stages of this work.

I gratefully acknowledge generous helps offered by Professor Naba Kumar Mondal who is the spokesperson of the INO collaboration. At this stage I would like to extend my thanks to Professor Kamales Kar, Professor Sudeb Bhattacharya, Professor G. Rajasekaran, Professor H. S. Mani, Professor M. V. N. Murthy, Professor Raj Gandhi, Dr. Amol Dighe, Dr. D. Indumathi, Dr. Brajesh Choudhary, Dr. Gobinda Majumder, Dr. Debasish Majumdar, Dr. Ambar Ghosal, Dr. Satyajit Saha, Dr. Subhasish Chattopadhyay, Dr. Abhijit Bandhopadhyay for having useful discussions on INO. I also acknowledge the moral support from my friends Saikat Biswas, Tapasi Ghosh, Satyajit Jena who are working for the INO collaboration.

I benefitted from discussing physics with Professor Amitava Datta, Professor Ashoke Sen, Professor Rajesh Gopakumar, Professor Dileep Jatkar, Professor Biswarup Mukhopadhyaya, Professor Soumitra Sengupta, Professor Anjan S. Joshipura, Professor Sreerup Raychaudhuri, Professor Gautam Bhattacharyya, Dr. Subhendra Mohanty, Dr. C. S. Aulakh, Dr. Anindya Datta, Dr. Asesh Krishna Datta and Dr. Raghavan Rangarajan at various stages.

I am much obliged to Professor Tapan Kumar Das, Professor Subinay Dasgupta, Dr. Anirban Kundu, Dr. Parongama Sen and Dr. Gautam Gangopadhyay from Calcutta University who have helped me in various ways during this work.

I wish to thank Dr. Arunansu Sil who helped me at the initial stage of my research work to grab the basics of neutrino oscillations. I would also like to thank my friend Shashank Shalgar for sharing his insights in neutrino physics and computer related issues. I admire the moral support that I received from Swarup Majee.

My heartiest thanks to Soumitra Nandi, Biplob Bhattacharjee, Kamalika Basu Hazra, Anasuya Kundu, Pratap K. Das, Anjan Kumar Chandra from Calcutta University for providing me the moral support during the initial stage of this work. I also would like to thank Professor S. D. Adhikari, Dr. R. Thangadurai, Anamitra Mukherjee, Arijit Saha, Pomita Ghosal, Atashi Chatterjee, Kalpataru Pradhan, Sudhir Kumar Gupta, Subhaditya Bhattacharya, Priyotosh Bandyopadhyay, R. Srikanth H., Shailesh Lal, Mahender Singh for sharing light moments with me and for their constant encouragement during my stay at Harish-Chandra Research Institute.

I gratefully acknowledge the cluster facilities of Harish-Chandra Research Institute for computational work. I received help from Professor Jasjeet Singh Bagla regarding the use of this cluster facility. I would like to thank Mr. Sanjai Verma, Mr. Shahid Ali Farooqui and Mr. Chandan Kanaojia for providing help regarding computers at various stages during this work.

I would like to acknowledge support from the project (SP/S2/K-10/2001) of the Department of Science and Technology, India for providing the financial support during the initial part of this work. I also acknowledge support from the XIth Plan Neutrino Project of the Harish-Chandra Research Institute.

Last but not least with all my heart, my deepest thanks are devoted to my beloved family : my father, my mother and my brother, Rakesh, for their ever patience and constant support, their daily encouragements and boundless love. All these things I could do, just for them.

Department of Physics,
University of Calcutta.

Sanjib Kumar Agarwalla
September 2008.

ABSTRACT OF THE THESIS

Neutrino physics is a very intense field of research having implications in different branches of physics, such as high energy physics, quantum field theory, cosmology, astrophysics, nuclear physics and geophysics. Spectacular results on neutrino oscillations in the last several years have triggered a lot of interest in neutrinos, from experimental as well as theoretical point of view, and many future neutrino experiments are in preparation or under discussion to sharpen our understanding about these tiny particles. This thesis addresses several aspects of these issues.

We have studied the physics reach of an experiment where neutrinos produced in a beta-beam facility at CERN are observed in a large magnetized iron calorimeter (ICAL) at the India-based Neutrino Observatory (INO). The idea of beta-beam is based on the production of a pure, intense, collimated beam of electron neutrinos or their antiparticles via the beta decay of accelerated radioactive ions circulating in a storage ring. Interestingly, the CERN-INO distance of 7152 km happens to be tantalizingly close to the so-called "magic" baseline where the sensitivity to the neutrino mass ordering (sign of $\Delta m^2_{31} \equiv m^2_3 - m^2_1$) and more importantly, θ_{13}, goes up significantly, while the sensitivity to the unknown CP phase is absent. This permits such an experiment involving the golden $P_{e\mu}$ channel to make precise measurements of the mixing angle θ_{13} and neutrino mass hierarchy avoiding the issues of intrinsic degeneracies and correlations which plague other baselines.

We propound the possibility of using large matter effects in the survival channel, P_{ee}, at long baselines for determination of the neutrino mass ordering and the mixing angle θ_{13}. Matter effects in the transition probabilites $P_{e\mu}$ and $P_{e\tau}$ act in consonance to give an almost two-fold effect in the survival channel. In addition, the problem of spurious solutions due to the leptonic CP phase and the atmospheric mixing angle θ_{23} does not crop up. Thus a beta-beam enables one to exclusively study the P_{ee} survival probability with the help of proposed megaton class water detectors like UNO, HyperKamiokande, MEMPHYS.

We have also explored the possibility of detecting new physics signals in dedicated experiments using a near and a far detector and a beta-beam source. We focus on the possible impact of flavor-changing and flavor-diagonal neutral current interactions that might crop up at the production point, in the oscillation stage, or at the detection point when one will deal with these upcoming facilities. For an example, the R-parity violating Supersymmetric model allows these kind of interactions and long baseline neutrino oscillation experiments may well emerge as test beds for this kind of models.

Contents

List of Figures **xv**

List of Tables **xxi**

1 A Preamble to Neutrino Physics **1**

1.1 Neutrino In a Nutshell 2

1.2 Neutrino Odyssey 2

1.3 What are the Main Sources of Neutrinos? 3

1.3.1 Natural Sources of Neutrinos 3

1.3.2 Artificial Man-made Sources of Neutrinos 6

1.4 Neutrino : "NU" Horizons 11

1.5 Layout of the Doctoral Work 12

2 Neutrino Oscillations Revisited **15**

2.1 Neutrinos in the Standard Model 15

2.2 Oscillations in Vacuum 17

2.2.1 Two-Flavour case 19

2.2.2 Three-Flavour case 20

2.3 Oscillations in Matter 22

2.4 Present Status 24

2.5 Missing Links 25

2.6 Future Neutrino Road-Map 27

3 Neutrino mass ordering and θ_{13} with a magical Beta-beam experiment at INO 29

3.1 Introduction 29

3.2 The Beta-beam Fluxes 32

3.2.1 The Beta-decay Spectrum 33

3.2.2 Candidate Ions for the Beta-beam 33

3.3 Neutrino Propagation and the "Golden Channel" 36

3.3.1 The "Golden Channel" ($\nu_e \rightarrow \nu_\mu$) 36

3.3.2 Eight-fold Degeneracy 37

3.3.3 Remedy with "Magic" Baseline 37

3.3.4 Near-Resonant Matter Effects 39

3.3.5 The Benchmark Oscillation Parameters 40

3.3.6 Phenomenology with $P_{e\mu}$ 41

3.3.7 One Mass Scale Dominance 43

3.4 Event Rates in ICAL@INO 44

3.4.1 The ICAL Detector at INO 44

3.4.2 Oscillation Signal at ICAL@INO 46

3.4.3 Background Rejection 51

3.5 Details of the Statistical Method 54

3.6 Measurement of the Neutrino Mass Ordering 56

3.7 Measurement of $\sin^2 2\theta_{13}$ 61

3.7.1 $\sin^2 2\theta_{13}$ Sensitivity Reach 61

3.7.2 $\sin^2 2\theta_{13}$ Discovery Reach 63

3.7.3 $\sin^2 2\theta_{13}$ Precision 64

3.8 Summary and Conclusions 64

4 Neutrino parameters from matter effects in P_{ee} at long baselines 67

4.1 Introduction . . . 67

4.2 The $\nu_e \rightarrow \nu_e$ Survival Probability . . . 68

4.3 The Experimental Set-up . . . 70

4.3.1 Pure ν_e ($\bar{\nu}_e$) Source . . . 70

4.3.2 Water Čerenkov Detector . . . 70

4.3.3 Backgrounds . . . 70

4.4 Simulation Details and Event Rates . . . 71

4.5 Sensitivity to sgn(Δm^2_{31}) and θ_{13} . . . 72

4.6 Discussions and Conclusions . . . 74

5 Can R-parity violating supersymmetry be seen in long baseline Beta-beam experiments? 75

5.1 Introduction . . . 75

5.2 $\not R$ Supersymmetry . . . 76

5.3 Golden Channel Oscillations including NSI . . . 77

5.4 Results . . . 81

5.4.1 Extraction of θ_{13} and determination of hierarchy . . . 81

5.4.2 Constraining λ' . . . 82

5.4.3 Effect of λ . . . 83

5.5 Conclusions . . . 83

6 Probing Lepton Number Violating Interactions with Beta-beam using a Near-Detector 85

6.1 Introduction . . . 85

6.2 Beta-beam Flux at a Near-Detector . . . 86

6.2.1 Detector Simulation Study . . . 87

6.2.2 Neutrino Fluxes . . . 88

6.3 $\not R$ Processes . . . 90

6.3.1 ν_τ Production in Beta-decay via $\not{R}$ Interactions 90
6.3.2 τ production from ν_e via $\not{R}$ Interactions 91
6.4 Results 92
6.4.1 Choice of Ion Source and Detector 94
6.4.2 Alternative Set-ups 96
6.5 Discussion and Conclusion 97

7 Summary and Conclusions 99

Bibliography 101

List of Publications 109

List of Figures

1.1 The schematic layout of the neutrino factory set-up. The web address http://www.cap.bnl.gov/mumu/project/ISS/ is the source of this figure. 9

1.2 Left panel depicts the beta-decay process which is the source of pure beta-beam. The proposed schematic layout of the beta-beam set-up at CERN (http://beta-beam.web.cern.ch/beta-beam/task/index.asp) has been displayed in the right panel. 10

2.1 The two flavour ν_e to ν_μ oscillation probability (Eq. 2.14). The mixing angle θ governs the oscillation amplitude and the frequency depends on $\Delta m^2_{12} = m^2_2 - m^2_1$, where m_1 and m_2 are the masses of the mass eigenstates ν_1 and ν_2 respectively. 17

2.2 Feynman diagrams showing neutrino scattering inside the matter. Left panel depicts CC interactions whereas right panel describes NC processes. 22

2.3 The sign of $\Delta m^2_{31} = m^2_3 - m^2_1$ is not known. The neutrino mass spectrum can be normal or inverted hierarchical. 26

3.1 The unoscillated beta-beam flux spectrum arriving at ICAL@INO. The upper panels are for ^{8}B (left panel) and ^{8}Li (right panel), while lower panels are for ^{18}Ne (left panel) and ^{6}He (right panel). 34

3.2 Left panel shows the total unoscillated flux in $yr^{-1}m^{-2}$ expected at INO, as a function of the Lorentz factor γ. The solid (dashed) line corresponds to ^{8}B (^{8}Li) and we have assumed 1.1×10^{18} (2.9×10^{18}) useful ions decays per year. Right panel shows the energy at which the unoscillated flux peaks, as a function of γ. 35

3.3 The upper panel shows the constant line average density of the Earth for various baselines calculated using the Preliminary Reference Earth Model (PREM) [110] and the lower panel depicts the corresponding resonance energy (where $\theta^m_{13} = \pi/4$) at those baselines. The blue dashed vertical line is drawn at the CERN-INO baseline. 38

3.4 The transition probability $P_{e\mu}$ as a function of E for four values of the baseline L. The band reflects the effect of the unknown δ_{CP}. The dark (red) shaded band is for the NH while the light (cyan) shaded band is for the IH. We have taken $\sin^2 2\theta_{13} = 0.1$ and for all other oscillation parameters we assume the benchmark values given in Table 3.2. 41

3.5 The dark (red) shaded band is the same as in Fig. 3.4. The light (green) shaded band shows the corresponding $P_{e\mu}$ for $\sin^2 2\theta_{13} = 0.05$. Values of all the other oscillation parameters are same as in Fig. 3.4 and the hierarchy is assumed to be normal. 42

3.6 The values of $\sin^2 2\theta_{13}$ needed for the maximal matter effect (from Eq. 3.18 with $p = 0$) at different baselines using the constant line average density of the Earth. The blue dashed horizontal line shows the present upper bound on $\sin^2 2\theta_{13}$ which predicts that the maximal probability (= 0.5) can only be achieved for $L \geq 7880$ km (see the black dot-dashed vertical line). 43

3.7 Left panel shows the location of the India-based Neutrino Observatory. The schematic view of the 50 kton iron calorimeter detector consisting of three modules each having 140 layers of iron plates is given in the right panel. These figures are obtained from the official website of INO (http://www.imsc.res.in/∼ino/). . 45

3.8 The expected number of events in 5 years running time, as a function of $\sin^2 2\theta_{13}$. The value of γ and the hierarchy chosen corresponding to each curve is shown in the figure legend. 47

3.9 The iso-event curves in the δ_{CP}-$\sin^2 2\theta_{13}$ plane for four baselines are shown in the figure. The true values of δ_{CP} and $\sin^2 2\theta_{13}$ are assumed to be 0° and 0.043 respectively. Left- (right-) hand panel is for the ν_e ($\bar{\nu}_e$) beta-beam. The assumed hierarchy is mentioned in the figure. 48

3.10 Total number of expected events in five years as a function of the baseline L for the ^{8}B source with $\gamma = 500$ and for two values of $\sin^2 2\theta_{13}$ and assuming that the NH is true. The hatched areas show the expected uncertainty due to the CP phase. 49

3.11 Total number of events as a function of γ for the ^{8}B source, for different values of L are shown in the four panels. The black hatched area shows the uncertainty range due to the CP phase when NH is true, while the area between the maroon dashed lines shows the corresponding uncertainty when IH is true. For all cases we assume $\sin^2 2\theta_{13} = 0.05$. 50

3.12 Total number of events as a function of γ for the ^{8}B source, for different values of L are shown in the four panels. The black hatched area shows the uncertainty range in the events due to CP phase when $\sin^2 2\theta_{13} = 0.05$, while the red hatched area shows the corresponding uncertainty when $\sin^2 2\theta_{13} = 0.01$. For all cases we assume NH to be true. 51

3.13 Total number of events as a function of γ for the ^{8}B (solid lines) and the ^{8}Li (dashed lines) sources. Results for both normal and inverted hierarchies are shown. 52

3.14 The range of $\sin^2 2\theta_{13}$(true) for which the wrong hierarchy can be ruled out at the 3σ C.L., as a function of γ. The left panel is for NH as true, while the right panel is when IH is true. The red solid curves show the sensitivity when the γ is chosen to be the same for both the neutrino and the antineutrino beams. The blue dashed lines show the corresponding sensitivity when the γ for the antineutrinos is scaled down by a factor of 1.67 with respect to the γ of the neutrino beam. 56

3.15 Plots showing the impact of various factors on the mass hierarchy sensitivity of the CERN-INO beta-beam experiment. The top left panel shows the impact of changing the detector threshold. The lower left panel shows the effect of changing the background rejection factor. The top right panel shows the difference in the sensitivity between the rate and spectral analysis. The lower right panel shows how the density profile would impact the hierarchy sensitivity. 57

3.16 Effect of δ_{CP}(true) on the hierarchy sensitivity. The black dashed lines show the worst and best cases when we allow δ_{CP}(true) to take any value between 0 and 2π. The red solid curve corresponds to the reference case where $\delta_{CP}(\text{true}) = 0$. The left panel shows the case for true NH while the right panel is for true IH. . 58

3.17 The variation of the experimental sensitivity on the number of useful ion decays in the straight sections of the storage ring. Left panel shows sensitivity to the mass hierarchy assuming NH to be true. Right panel shows the $\sin^2 2\theta_{13}$ sensitivity reach. In both panels, the majenta solid vertical line corresponds to the reference value used in the rest of the analysis. 59

3.18 Left panel shows the 3σ sensitivity limit for $\sin^2 2\theta_{13}$. Right panel shows the 3σ discovery reach for $\sin^2 2\theta_{13}$(true). The red solid lines in the left and right panels show the sensitivity reach and discovery potential respectively, when the γ is assumed to be the same for both the neutrino and the antineutrino beams. The blue dashed lines show the corresponding limits when the γ for the ^{8}Li is scaled down by a factor of 1.67 with respect to the γ of the neutrino beam, which is plotted in the x-axis. 62

3.19 The precision with which $\sin^2 2\theta_{13}$ will be measured by the CERN-INO beta-beam experiment as a function of $\sin^2 2\theta_{13}$(true). Left panel shows the 3σ allowed range of $\sin^2 2\theta_{13}$ while the right panel shows the precision defined in the text. . 64

4.1 The survival probability P_{ee} in matter as a function of E for four different values of the baseline L. For each L, the plots are given for three different values of $\sin^2 2\theta_{13}$ (0.17, 0.1 and 0.05). Thick (thin) lines are for NH (IH). 69

4.2 Events in 5 years vs. $\sin^2 2\theta_{13}$ for NH (dashed line) and IH (solid line) for $L = 7500$ km and $\gamma = 500$. The inset shows the same but for $\gamma = 250$. 71

4.3 Sensitivity to hierarchy for $L = 7500$ (solid line) and 10000 km (dashed line) and $\gamma = 250$, as a function of $\sin^2 2\theta_{13}$(true). 72

4.4 The upper panel shows the range of $\sin^2 2\theta_{13}$(true) for which the wrong IH can be excluded at 90% and 3σ C.L. while the lower panel gives the sensitivity to $\sin^2 2\theta_{13}$ at various baselines at 90% and 3σ C.L., for two values of γ. 73

5.1 $P_{\nu_e \to \nu_\mu}$ for the NH and IH. SM corresponds to only standard electroweak interactions. The values of λ' are given in parentheses. m can take any value, $n = 2$ or 3. 80

5.2 Number of muon events for the NH (left panel) and IH (right panel) as a function of $\sin^2 2\theta_{13}$ for a five years of ICAL@INO run. The solid lines correspond to the absence of any NSI. The hatched area is covered if the λ' couplings are varied over their entire allowed range. 82

5.3 The number of events as a function of a coupling $|\lambda'|$, present singly, for the NH (left panel) and IH (right panel). The thick (thin) lines are for $|\lambda'_{331}|$ ($|\lambda'_{2m1}|$, $m = 2$, 3). The chosen $\sin^2 2\theta_{13}$ are indicated next to the curves. 83

5.4 Number of muon events for the NH (left panel) and IH (right panel) as a function of $\sin^2 2\theta_{13}$ for a five years of ICAL@INO run. The solid lines correspond to the absence of any NSI. The hatched area is covered if the λ couplings are varied over their entire allowed range. 84

6.1 A schematic diagram of the proposed detector (a part only). The incoming ν_e beam may have a very small contamination of neutrinos of other flavours in the presence of lepton flavour violating interactions. 86

6.2 Detector efficiency for $\gamma = 250, 350, 450$. The corresponding cuts on muon hits used are 6, 10 and 13 respectively. 88

6.3 Feynman diagrams for $\not{R}$ interactions during beta-decay through (a) $\lambda'\lambda'$ and (b) $\lambda\lambda'$ type trilinear product couplings. Substantial event rates are obtained in (a) when $k = 2, 3$. 90

6.4 Feynman diagrams for tau production from an incoming ν_e beta-beam through (a) $\lambda'\lambda'$ and (b) $\lambda\lambda'$ type trilinear product couplings. Substantial event rates are obtained in (a) when $k = 2, 3$. 91

6.5 Geometry integrated flux $\Phi(E; S, D, R, L)/g$ taking ^{8}B as the decaying ion is plotted against neutrino energy E for different γ for $S = 2500$ m, $D = 202.13$ m, $R = 1$ m, and $L = 200$ m. The vertical line at 3.5 GeV indicates the tau production threshold energy. 94

6.6 Expected number of $\not R$ muon events in five years for a 5 kton iron detector vs. the detector length for $\gamma = 250$, 350, and 450 for ^{8}B beta-beam flux. The left (right) panel is for the $\lambda'\lambda'$ ($\lambda\lambda'$) driven process. $k = 2, 3$. 95

6.7 Muon signal event rate in 5 years as a function of the detector (Fe) length for three different choices of base-length have been shown for ^{8}B beta-beam flux. The left (right) panel corresponds to the $\lambda'\lambda'$ ($\lambda\lambda'$) driven process. $k = 2, 3$. . . . 96

6.8 Bounds on $|\lambda'^{\star}_{31k}\lambda'_{11k}|$, $k = 2, 3$ ($|\lambda^{\star}_{231}\lambda'_{211}|$ or $|\lambda_{213}\lambda'^{\star}_{211}|$) versus detector size at 95% C.L. for zero observed events is depicted in left (right) panel for $\gamma = 250, 350, 450$. The bounds scale as $(\tilde{m}/100 \text{ GeV})^2$. The results are for a five-year run for a 5 kton Fe detector placed at a distance of 200 m from the front end of the storage ring for ^{8}B beta-beam flux. 97

6.9 Comparison of the muon signal event rates as a function of the detector length for a 5 kton iron calorimeter placed at a distance of 200 m from the storage ring for $\gamma = 800$ (250) with ^{18}Ne (^{8}B). The left and right panels correspond to $\lambda'\lambda'$ and $\lambda\lambda'$ driven processes, respectively. 98

List of Tables

1.1 Beta decay parameters: lifetime τ, electron total end-point energy E_0, f-value and decay fraction for various ions [74]. 10

2.1 Matter contents of the Standard Model with their corresponding gauge quantum numbers. $I = 1, 2, 3$ is the generation index. The electromagnetic charge listed in the last column is defined as $Q_{em} = T_3 + Y$. 16

2.2 The impact of matter potential in various mediums. 22

2.3 Best-fit values and $3\sigma(1$ d.o.f) constraints on the oscillation parameters under three-flavour scheme from global data including solar, atmospheric, reactor (KamLAND and CHOOZ) and accelerator (K2K and MINOS) experiments. This table has been taken from [79]. 24

3.1 Possibilities for long baselines from CERN. In the third column, the distances (in km) from CERN to various existing/proposed underground neutrino observatories spread over the entire world are given. The respective dip angles are also mentioned in the last column. The distance of INO from CERN is 7152 km with a dip angle of 34.0°. 39

3.2 Chosen benchmark values of oscillation parameters and their 1σ estimated errors. The last row gives the corresponding values for the Earth matter density. 40

3.3 The distances from INO to various accelerator based laboratories spread over the entire world. The corresponding dip angles are also noted. 45

3.4 Detector characteristics of ICAL@INO used in the simulations. The bin size is kept fixed, while the number of bins is varied according to the maximum energy. 46

3.5 Comparison of the variation of the detector sensitivity to mass hierarchy (columns 2 and 3) and $\sin^2 2\theta_{13}$ sensitivity (columns 4 and 5) with γ and N, the number of useful ion decays per year. 60

Neutrino of Love

I go undetected
In all my interactions
I cannot be seen
From any point of view
You won't know if I'm here
Except when I'm gone
I'm the neutrino of love
And I'm coming over you

You cannot keep me in a cage
No matter how thick the walls
I will escape
You cannot hold me in a box
Cannot bind me with a lock
Cannot keep me anyway
I'm not afraid of the dark
I'm the neutrino
Neutrino of love
I'm the neutrino
Neutrino of love

I go undetected
In all my interactions
I cannot be seen
From any point of view
You won't know if I'm here
Except when I'm gone
I'm the neutrino of love
And I'm coming over you

I'm the neutrino baby
Neutrino of love

Cannot inhibit my infiltration
Neutrino

Cannot prevent my penetration
Neutrino

I am the neutrino

Dylan Casey: guitar and vocals, 2001

Chapter 1

A Preamble to Neutrino Physics

The musical description of neutrinos by Dylan Casey in his song “Neutrino of Love” is really fantastic. Yes indeed, neutrinos are elusive, mysterious, yet abundant. Despite that (or because of that!), even after fifty years of it’s discovery, it still poses many mysteries and creates challenges to the physicists who want to detect it. Like electrons, they are elementary particles. F. Reines would narrate neutrino as, it is “...the most tiny quantity of reality ever imagined by a human being”.

Neutrino physics is a very intense and exciting field of research having wide range of implications in high energy physics, quantum field theory, cosmology, astrophysics, nuclear physics, and geophysics. Marvellous results on neutrino oscillations in the last several years have triggered a lot of enthusiasm and interest in neutrinos, from experimental as well as theoretical point of view. One of the most important facts is that neutrino physics is a data driven field - for several years now, new data are pouring at an outstanding rate. Our understanding of neutrinos has improved dramatically in the past ten years and there is no doubt that neutrino oscillation is an exclusive example of experimental evidence for physics beyond the Standard Model of particle physics. This success sets a fantastic example of a road-map in which both theoretical understanding and experimental achievements have walked hand in hand to provide us with the first evidence of physics beyond the Standard Model. These developments culminated in the Nobel prize for physics in the year 2002, which was awarded to two pioneers in neutrino physics. Masatoshi Koshiba was awarded the prize for the detection of neutrinos from a supernova and Ray Davis Jr. for his detection of solar neutrinos.

Neutrino physics is now poised to move into the precision regime. Active attempts are under way to commence the era of precision neutrino measurement science which will surely widen the horizon of our knowledge about neutrinos. A number of high-precision neutrino oscillation experiments have been contrived to sharpen our understanding about these tiny particles. This is the right time to ask how different planned/proposed next generation experiments in the coming decades would perform to explicate the nature of neutrinos and our thrust for new physics. This thesis is an effort to have a look on several aspects of these issues.

1.1 Neutrino In a Nutshell

Neutrinos are electrically neutral particles of spin $\frac{1}{2}$ with a very tiny mass, almost 500 000 times smaller than the mass of the electron, which itself is 2000 times smaller than the proton mass. There are at least three species (or flavours) of very light neutrinos, ν_e, ν_μ and ν_τ, which are left handed, and their antiparticles, $\bar{\nu}_e$, $\bar{\nu}_\mu$ and $\bar{\nu}_\tau$, which are right handed. After the photon, the neutrino is the most abundant particle in the Universe : each cubic meter of the Universe contains about 30 million neutrinos, which are remnant from the Big Bang, similar to the well known cosmic microwave background. It also arrives "unscathed" from the farthest reaches of the Universe, carrying information about its source. The interactions of neutrinos are mediated by heavy $W^\pm$ and Z^0 bosons and therefore at low energies they talk feebly with ordinary matter and pass through the Earth very much like light through a crystal. If a matter target as big as Earth is placed in front of 100 billion neutrinos, only one of them is likely to interact with it. The mean free path of a 1 MeV neutrino in lead is about 1 light year! Therefore neutrino detection requires very large detectors and/or very intense neutrino beams.

1.2 Neutrino Odyssey

Let us have a look at the incredible journey of discovery into one of Nature's most elusive particles. In a letter to colleagues on 4th December, 1930, Wolfgang Pauli [1] postulated the existence of neutrinos to guarantee the energy conservation in radioactive beta-decay. After the discovery of the neutron by James Chadwick two years later, it was first speculated that the particle predicted by Pauli could be the neutron. However, soon it was realized that Pauli's particle had to be much lighter than the neutron. In 1933, Enrico Fermi introduced the name neutrino, where he used the Italian syllable "-ino" to indicate "small neutron". More than two decades after Pauli's letter proposing the neutrino, in 1956, Clyde Cowan and Frederick Reines [2] observed the antineutrinos (the antimatter partners of neutrinos) emitted by a nuclear reactor. This neutrino is later determined to be the partner of the electron. In 1969, neutrinos produced by the Sun's burning were detected by Ray Davis with a detector based on Chlorine in an underground laboratory in the Homestake mine in USA. This experiment reported that less than half the expected neutrinos were detected. This originated the long-standing "solar neutrino problem". The scope that the missing electron neutrinos may have transformed into another type (undetectable to this experiment) was soon suggested, but the lack of our knowledge of the solar model on which the expected neutrino rates were based was initially considered a more likely explanation.

In 1987, neutrinos from a supernova in the Large Magellanic Cloud were also detected. Only 19 events were observed [3, 4, 5] and they established the standard picture of core-collapse supernovae. In recent years, several experiments could confirm the existence of neutrino oscillations. In 1998, the Super-Kamiokande experiment [6] reported the evidence for oscillations of atmospheric neutrinos. It was a crucial juncture for neutrino physics. Neutrino oscillation demands that neutrinos do have a mass and the observation of large mixing angle was completely beyond the range of our imagination because in analogy to the quark mixing, it was the common belief that if neutrinos mixed at all then the mixing should be small.

The year 2002 was a spectacular year for neutrino physics. The neutral current (NC) data of the SNO [7] solar neutrino experiment provided an independent determination of the total flux of active neutrinos from the Sun. The combined SNO and other solar neutrino data finally could establish an explanation of the longstanding solar neutrino problem in terms of neutrino oscillations. The KamLAND [8, 9] reactor neutrino experiment confirmed the oscillation hypothesis observing disappearance of $\bar{\nu}_e$ and constrained the mixing parameters to the so-called LMA-MSW [10] solution. The K2K [11] experiment is the first long baseline experiment which uses novel man-made accelerator beams. This experiment provided an independent confirmation of the explanation for the observed atmospheric neutrino anomaly by supplying the data which is consistent with it's oscillation interpretation.

All the results from these dedicated experiments forced us to recall the pioneering work by Gribov and Pontecorvo [12, 13]. In 1968, they showed that flavour conversions can arise if neutrinos are massive and mixed. Neutrino oscillation is the only phenomenon which can describe the outcome of all these experiments and it can easily explain the disappearance of both atmospheric ν_μ's and solar ν_e's. There are two recent very good reviews [14, 15] on this topic in general which can give us more insight.

1.3 What are the Main Sources of Neutrinos?

Neutrinos are the most common matter particles in the universe. Neutrinos are produced via weak interactions (like beta-decays in atomic nuclei). In number, they exceed the constituents of ordinary matter (electrons, protons, neutrons) by a factor of ten billion. We have used neutrinos from many different origins with different energy ranges to study neutrino oscillations and the properties of neutrino sources. Mainly we can classify the neutrino sources into two categories :

1. **Natural sources of neutrinos.**
2. **Artificial man-made sources of neutrinos.**

1.3.1 Natural Sources of Neutrinos

The Sun

One of the strongest neutrino sources is our Sun. The Sun shines not only in light but also in electron neutrinos produced in the thermonuclear reactions which generate the solar energy. These reactions take place via two main chains, the *pp* chain and the CNO cycle. There are five reactions which produce ν_e in the *pp* chain and three in the CNO cycle. Both chains result in the overall fusion of protons into ^{4}He :

$$4p \rightarrow ^4 \mathrm{He} + 2\mathrm{e}^+ + 2\nu_\mathrm{e} + \gamma, \tag{1.1}$$

where the energy released in the reaction, $Q = 4m_p - m_{^4He} - 2m_e \simeq 26$ MeV, is mostly radiated through the photons and the neutrinos carry only a small fraction of it, $\langle E_{2\nu_e} \rangle = 0.59$ MeV. Hence, the observation of solar neutrinos provides direct evidence for the nuclear process in the center of the sun. Moreover, current solar neutrino data allow a quantitative test of the Standard Solar Model (SSM) [16]. By the measurement of the solar neutrino flux the temperature in the center of the sun can be determined with the impressive accuracy of 1%.

The Sun emits about 2×10^{38} electron neutrinos per second, leading to the neutrino flux at the surface of the earth of $\sim 6 \times 10^{10}$ $cm^{-2}s^{-1}$ in the energy range $E \leq 0.42$ MeV and $\sim 5 \times 10^6$ $cm^{-2}s^{-1}$ in the energy range 0.8 MeV $\lesssim E \leq 15$ MeV. The detection mechanism of solar neutrinos is very sophisticated and involves mainly the radiochemical processes (Homestake, Gallex, Sage, GNO detectors) [17, 18] and the water Čerenkov techniques (Kamiokande, SuperKamiokande, SNO detectors) [6, 7, 19, 20].

The Earth's Atmosphere

Earth's atmosphere is another crucial source of electron and muon neutrinos and their antiparticles which are created in the hadronic showers induced by primary cosmic rays. Atmospheric neutrinos were first detected in the 1960's by the Kolar Gold Field experiment in India [21] and the underground experiments in South Africa [22]. The following chain of reactions depicts the main mechanism of production of the atmospheric neutrinos :

$$\begin{array}{lcccl} p(\alpha, ...) + Air & \rightarrow & \pi^\pm(K^\pm) & + & X \\ & & \pi^\pm(K^\pm) & \rightarrow & \mu^\pm + \nu_\mu(\bar{\nu}_\mu) \\ & & & & \mu^\pm \rightarrow e^\pm + \nu_e(\bar{\nu}_e) + \bar{\nu}_\mu(\nu_\mu) \end{array} \tag{1.2}$$

Atmospheric neutrinos can be directly detected in large mass underground detectors predominantly by means of their charged current (CC) interactions :

$$\begin{array}{l} \nu_e(\bar{\nu}_e) + A \rightarrow e^-(e^+) + X \, , \\ \nu_\mu(\bar{\nu}_\mu) + A \rightarrow \mu^-(\mu^+) + X \, . \end{array} \tag{1.3}$$

Atmospheric neutrinos cover a wide range of energy starting from few MeV to hundreds of GeV. The typical flux of atmospheric neutrinos at the earth's surface is $\sim 10^{-1}$ $cm^{-2}s^{-1}$. These neutrinos are observed in underground experiments with bigger and better detectors using different detection techniques and leading to different type of events depending on their energy. In the last ten years, the high precision and large statistics data from the Super-Kamiokande [6] experiment (using water Čerenkov detectors) has played an important role to solve the atmospheric neutrino puzzle through the concept of neutrino oscillation. It has received important confirmation from the iron calorimeter detectors Soudan2 [23] and MACRO

[24]. In June 1998, in the Neutrino98 conference, Super-Kamiokande collaboration presented evidence of ν_μ oscillations based on the angular distribution for their contained event data sample.

Recently, in India, to observe atmospheric neutrinos, the proposal for a large magnetized iron calorimeter detector (ICAL) with charge identification capability is being evaluated by the INO [25] collaboration. We will discuss about this detector in detail later.

The Earth's Crust

The Earth contains a certain amount of natural radioactivity, and the decay of these radioactive elements is an important and perhaps main source of geothermal heat. These same decays also generate particles known as geoneutrinos. "Geoneutrinos" are electron antineutrinos produced by beta-decays of the unstable, radioactive nuclei in the decay chains of ^{238}U, ^{232}Th, ^{40}K. The amount of neutrinos coming from this natural radioactivity is huge : about 6 millions per second and per cm^2 with the energy E $\lesssim$ 1 MeV.

A careful observation of the arrival directions of neutrinos generated in the decay of natural radioactive elements in the Earth's interior can give us a three-dimensional view of the Earth's composition and shell structure. This will provide a new and detailed understanding of the origin of the Earth's geothermal heat, and will finally answer the question of how much heat comes from radioactive decays, and how much is "primordial" heat leftover from the birth of the Earth. The mapping of the Earth's interior might also help give answers to such questions as "What powers the magnetic field of the Earth?" and "What dominates the geodynamo?". To actually take a neutrino picture of the Earth is quite challenging technically, but not impossible.

Recently the KamLAND experiment, which was primarily designed to measure anti-neutrinos from nuclear reactors, reported 9 events [26] due to geoneutrinos. This marks the first detection of neutrinos from the Earth's interior, and already demonstrates that radioactivity is an important heat source for the Earth.

The Supernovae within our galaxy

The life of a star ends often with a huge explosion called Supernova, which can be even brighter than a whole galaxy. However, only a tiny amount of the total released energy is emitted as light. About 99% of the energy is released in the form of neutrinos having energies in the range 10-30 MeV. Roughly, they emit $\sim 6 \times 10^{58}$ neutrinos and antineutrinos of all flavours over the time interval of about ten seconds. The neutrino luminosity of a gravitational collapse-driven supernova is typically 100 times its optical luminosity. The neutrino signal emerges from the core of a star promptly after core collapse, whereas the photon signal may take hours or days to emerge from the stellar envelope. The neutrino signal can therefore give information about the very early stages of core collapse, which is inaccessible to other kinds of astronomy.

In 1987, there was a Supernova in the Large Magellanic Cloud within our galaxy. Indeed, about 19 neutrinos have been observed, which confirmed our basic understanding of the Supernova explosion mechanism. Neutrinos from gravitational collapse can be detected in various ways. For water Čerenkov detectors, such as Super-Kamiokande, the most important detection reaction is the absorption of electron antineutrinos on protons :

$$\bar{\nu}_e + p \rightarrow n + e^+. \tag{1.4}$$

The positron from this reaction, which retains most of the energy of the incoming neutrino, is detected from it's Čerenkov light.

The Big-Bang

The most extraordinary explosion of all, the Big Bang, created more neutrinos than any other source which has existed since. The "standard" model of the Big-Bang predicts, like for the photons, a cosmic background of neutrinos. These relic neutrinos still exist, have a number density of about 110 cm^{-3} for each neutrino species and a black-body spectrum with the average energy of about 0.0005 eV. The energy of these neutrinos is too small so that no experiment, even very huge, has been able to detect them.

The Ultra-High Energetic Cosmic Neutrino Sources

Astrophysical neutrinos can also be produced with remarkably high energies. Neutrinos born in the center of an active galaxy can arrive on Earth with more energy than we will ever be able to create with a terrestrial accelerator. Gamma-ray bursts (GRB) and active galactic nuclei (AGN) jets have been suggested as sources of high-energy, $> 10^{14}$ eV, neutrinos, with fluxes that may be detectable in a kilometer-squared effective area telescope [27].

1.3.2 Artificial Man-made Sources of Neutrinos

The Nuclear Reactors (Power Plants)

Electron antineutrinos with $E \sim$ MeV are produced copiously in the process of generating electrical power in nuclear power plants using controlled fission technique. A 3 GW plant releases about 7.7×10^{20} $\bar{\nu}_e$ per second and creates a flux of $\sim 6 \times 10^{11}$ $cm^{-2}s^{-1}$ at 100 m. Due to the low energy, e's are the only charged leptons which can be produced in the neutrino CC interaction. If the $\bar{\nu}_e$ oscillated to another flavour, its CC interaction would not be observed. Therefore only disappearance experiments can be performed with reactors.

The KamLAND experiment [8], a 1000 ton liquid scintillation detector, is currently in operation in the Kamioka mine in Japan. This underground site is located at an average distance of 150-210 km from several Japanese nuclear power stations. This experiment has played a crucial role to establish the fact that the solar neutrino puzzle can be explained by the so-called LMA-MSW [10] solution. Gosgen [28], Krasnoyarsk [29], Bugey [30], CHOOZ [31] and Palo Verde [32] are the examples of reactor experiments which are performed at relatively short or intermediate baselines. It is worth-while to mention here that none of these experiments find a positive evidence of flavour mixing.

The Particle Accelerators

Now neutrino physics has entered into precision age from discovery era. Only in a well tuned, fully optimized environment will it be possible to perform precision measurements of neutrino oscillation parameters. A high intensity neutrino source with known spectrum is most desirable for precision measurements, the consensus direction for the future. Man-made accelerator based neutrino beams of the energy ranging typically between 30 MeV to 30 GeV are the novel, intense sources of neutrinos, an important tool for studying neutrino properties. Beam shape parameters play a very key role for the measurement of oscillation length, while the absolute normalization is crucial for the determination of the mixing angle. One of the most important features of the neutrino beam is that one can control the flux of the produced neutrinos and can tune the main parameters that govern the systematic uncertainties on the neutrino fluxes. Currently, there are three widely different schemes for producing neutrino beams and they mainly differ from each other on the issue of what particle is decaying (pion decay, muon decay and radioactive ion decay) to give rise to the neutrinos. For a detailed discussion of future beams and their comparison see [33, 34] and references therein.

1. Conventional Neutrino Beams

Conventional neutrino beams are produced by shooting a target with as many protons as can be provided, and then focusing the produced mesons (mostly pions and some kaons) into an evacuated decay pipe where they are allowed to decay. The mesons will decay primarily to muons and muon neutrinos. This decay chain is quite similar in nature to the decay process through which the atmospheric neutrinos are produced. But one should keep in mind that the energy spectrum of the conventional neutrino beam is quite different compared to that of atmospheric one. From meson decay (two-body decay) kinematics it follows that the neutrino energy is given by

$$E_\nu = \frac{m^2_{\pi(K)} - m^2_\mu}{m^2_{\pi(K)}} \frac{E_{\pi(K)}}{(1+\gamma^2\theta^2)}, \tag{1.5}$$

where γ is the Lorentz boost of the parent meson, $E_{\pi(K)}$ it's energy and θ the angle of the neutrino with respect to the meson flight direction. The polarity of the focusing device has to be reversed to produce a beam of $\bar{\nu}_\mu$. In both the cases, there is always some contamination of ν_e or $\bar{\nu}_e$ due to the three-body decays of the kaons and daughter muons.

We can classify the conventional neutrino beams into three categories : the Wide Band Beams (WBB), the Narrow Band Beams (NBB) and the Off-Axis Beams (OAB).

The main feature of WBB is that they have wide energy spectrum with high neutrino flux. They are perfectly suited to make discoveries. But they have some limitations. In a WBB, the irreducible fraction of ν_e originating from the meson decays is quite significant and these ν_e produce electrons inside the detector which play the role of intrinsic beam related background when we try to extract interesting results using the $\nu_\mu \to \nu_e$ appearance channel. Another problem is that WBB comes with a tail of high energy neutrinos and often these neutrinos produce π^0 inside the detector via NC process. Now, the early showering of gamma's from the π^0 decay can be misidentified for a ν_e CC interaction. If the signal corresponds to a small part of the energy spectrum, it could be overwhelmed by the beam induced background coming from the region which is outside the signal.

The NBB are quite opposite in nature. This facility can provide us almost monochromatic energy spectra by judiciously choosing a small momentum bite of the parent π and K. However, the neutrino yield is quite suppressed which causes problem for oscillation searches.

The OAB [35] is a classic example of a neutrino beam with high flux and a narrow energy spectrum. This technique requires designing a beam-line which can produce and focus a wide range of mesons in a given direction (as in the WBB case), but then placing the detectors at an angle with respect to that direction. Since the pion decay is a two-body process (see Eq. 1.5), we can obtain neutrinos of a given energy at a given angle between the pion direction and the detector location. But the most important feature to be noted that at this given angle, the energy of the neutrino produced in the decay of the pion becomes practically independent of the boosted pion energy. Now, if we place a detector at this particular angle with respect to the decay pipe then it will see a neutrino beam with a very narrow energy spread compared to the on-axis beam. Furthermore, this off-axis technology helps us to reduce the background coming from the intrinsic ν_e contamination in the beam and a smaller fraction of high energy tails reduces the background from NC events. As a result, it improves the signal-to-background ratio a lot.

But it is important to mention that, independent of the adopted solution, all conventional neutrino beams have some common problems. The first major drawback is that the hadron production in the proton-target interaction has large uncertainties due to lack of data and theoretical difficulties in describing hadronic processes. It creates obstacles in predicting the neutrino flux and spectrum with good accuracy. Secondly, in addition to the dominant flavour in the beam (typically ν_μ) there is a contamination (at the few percent level) from other flavours ($\bar{\nu}_\mu$, ν_e and $\bar{\nu}_e$) resulting into a "multiflavour" neutrino beam.

A recently terminated conventional beam experiment is the K2K experiment [11] where a neutrino beam was directed towards the Super-Kamiokande detector from the KEK accelerator. This experiment has already confirmed the disappearance of ν_μ as predicted by atmospheric neutrino data. The MINOS [36] experiment in US, and the CERN to Gran Sasso (CNGS) experiment OPERA [37] are the two conventional beam experiments which are collecting data now. Another CNGS experiment ICARUS [38] will start taking data soon.

2. **SuperBeams**

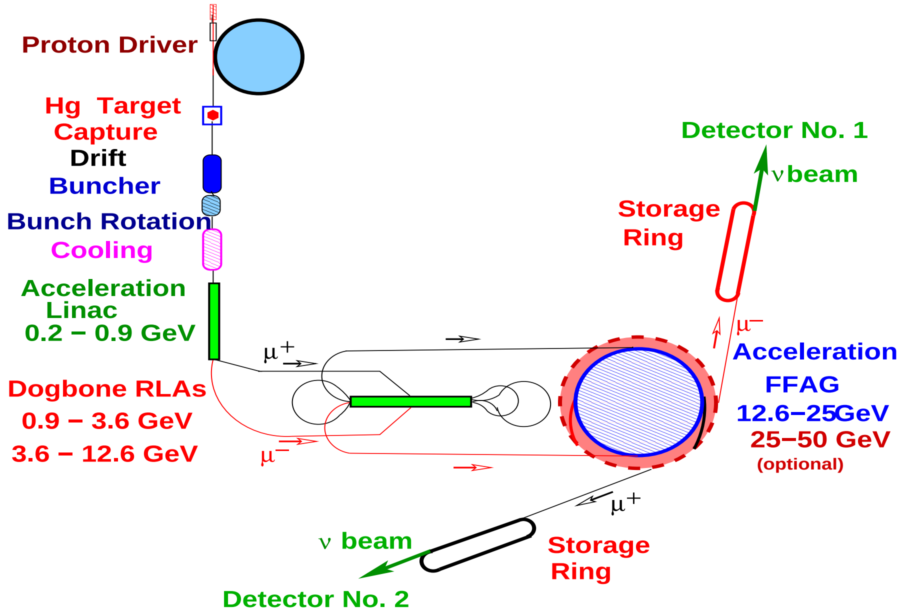
Proton Driver
Hg Target
Capture
Drift
Buncher
Bunch Rotation
Cooling
Acceleration
Linac
0.2 – 0.9 GeV
Dogbone RLAs
0.9 – 3.6 GeV
3.6 – 12.6 GeV
μ+
μ−
Detector No. 1
ν beam
Storage
Ring
μ−
Acceleration
FFAG
12.6–25GeV
25–50 GeV
(optional)
μ+
ν beam
Storage
Ring
Detector No. 2

Figure 1.1: The schematic layout of the neutrino factory set-up. The web address http://www.cap.bnl.gov/mumu/project/ISS/ is the source of this figure.

The technology of conventional beam experiments with some technical upgrades is known as superbeam. These experiments are 'super' in the sense that they will use proton beams of unprecedented strength around 1 - 4 MW and detectors with large fiducial mass. All superbeams use a near detector for a better control of the systematics. The most advanced superbeam proposals are the J-PARC to Super-Kamiokande experiment (T2K) [39] in Japan, and the NuMI off-axis experiment (NOνA) [40], using a neutrino beam produced at Fermilab in US.

3. **Neutrino Factory**

The term "neutrino factory" [41] has been associated to describe neutrino beams created by the decays of high energy muons which are circulated in a storage ring with long straight sections. The decay of muons in these straight sections produces an intense, well known and pure beam of ν_μ and $\bar{\nu}_e$. If μ^+ are stored, $\mu^+ \to e^+\nu_e\bar{\nu}_\mu$ decays generate a beam consisting of equal numbers of ν_e and $\bar{\nu}_\mu$. The overall layout is shown in Fig. 1.1. The muons are obtained via pion decay. To make a muon beam which can be accelerated, first the muons have to be cooled in phase space with the help of ionization cooling technique which is being studied by the MICE experiment [42]. There are other ways also being examined to tackle this problem. Several design studies have been performed in this direction in Europe, the United States and Japan [33, 43]. Typical neutrino factories are being considered with muon energies ranging from 20 GeV to 50 GeV with $\sim 10^{21}$ useful muon decays per year inside the storage ring.

In a neutrino factory experiment with stored μ^-, the appearance channel, $\bar{\nu}_e \to \bar{\nu}_\mu$ give rise to μ^+ in the detector via CC deep inelastic scattering. These anti-muons are called wrong

Ion	τ (s)	E_0 (MeV)	f	Decay fraction	Beam
${}^{18}_{10}$Ne	2.41	3.92	820.37	92.1%	ν_e
${}^{6}_{2}$He	1.17	4.02	934.53	100%	$\bar{\nu}_e$
${}^{8}_{5}$B	1.11	14.43	600872.07	100%	ν_e
${}^{8}_{3}$Li	1.20	13.47	425355.16	100%	$\bar{\nu}_e$

Table 1.1: Beta decay parameters: lifetime τ, electron total end-point energy E_0, f-value and decay fraction for various ions [74].

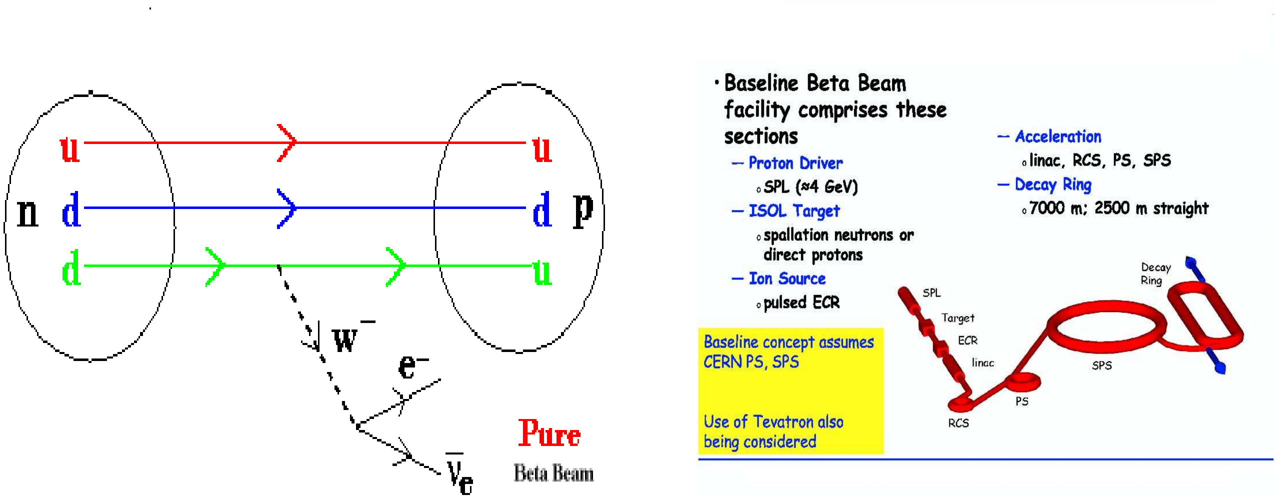

- Baseline Beta Beam facility comprises these sections
  - Proton Driver
    - SPL (≈4 GeV)
  - ISOL Target
    - spallation neutrons or direct protons
  - Ion Source
    - pulsed ECR
  - Acceleration
    - linac, RCS, PS, SPS
  - Decay Ring
    - 7000 m; 2500 m straight

Baseline concept assumes CERN PS, SPS

Use of Tevatron also being considered

Figure 1.2: Left panel depicts the beta-decay process which is the source of pure beta-beam. The proposed schematic layout of the beta-beam set-up at CERN (http://beta-beam.web.cern.ch/beta-beam/task/index.asp) has been displayed in the right panel.

sign muon events, since they have the opposite charge relative to the muons produced by the ν_μ in the beam itself. These wrong sign muons have to be cleanly separated inside the detector from the muons created by the surviving ν_μ. This charge identification can be achieved with a magnetized iron calorimeter detector like the proposed ICAL@INO [25].

Muon decay is well known and it will provide the neutrino flux and spectrum with minimal systematic uncertainties, compared to conventional neutrino beams. Radiative effects on the muon decay is negligible. Ultimately, the flux from a neutrino factory is expected to be known with a precision of the order of 10^{-3}. Another vital point to be noted is that a neutrino factory beam has a sharp cut-off at the energy of the stored muons which reduces the background from NC events. In a neutrino factory, the neutrinos with higher energy opens up the possibility to study the oscillation channels like $\nu_\mu \rightarrow \nu_\tau$ and $\nu_e \rightarrow \nu_\tau$ because one can produce tau leptons inside the detector [44].

4. **Beta-beam**

Zucchelli [45] put forward the novel idea of a beta-beam [46, 47, 48, 49, 50, 51, 52, 53, 54, 55, 56, 57, 58, 59, 60, 61, 62, 63, 64, 65, 66, 67], which is based on the concept of creating a pure, well understood, intense, collimated beam of ν_e or $\bar{\nu}_e$ through the beta-decay (see left panel of Fig. 1.2) of completely ionized radioactive ions. Firstly, radioactive nuclides are created by impinging a target by accelerated protons. These unstable nuclides are collected, fully ionized, bunched, accelerated and then stored in a decay ring (see for e.g. [68, 69]). The decay of these highly boosted ions in the straight sections of the decay ring [70] produces the so-called beta-beam. Feasibility of this proposal and its physics potential is being studied in depth [71], and will take full advantage of the existing accelerator complex at CERN and/or FNAL (Fermi National Accelerator Laboratory). The proposed schematic layout of the beta-beam set-up at CERN[1] is given in the right panel of Fig. 1.2. The main future challenge lies in building an intense proton driver and the hippodrome-shaped decay ring which are essential for this programme.

It has been proposed to produce ν_e beams through the decay of highly accelerated ^{18}Ne ions ($^{18}_{10}\text{Ne} \rightarrow {}^{18}_{9}\text{F} + e^{+} + \nu_e$) and $\bar{\nu}_e$ from ^{6}He ($^{6}_{2}\text{He} \rightarrow {}^{6}_{3}\text{Li} + e^{-} + \bar{\nu}_e$) [45, 70]. More recently, ^{8}B ($^{8}_{5}\text{B} \rightarrow {}^{8}_{4}\text{Be} + e^{+} + \nu_e$) and ^{8}Li ($^{8}_{3}\text{Li} \rightarrow {}^{8}_{4}\text{Be} + e^{-} + \bar{\nu}_e$) [72, 73] with much larger end-point energy have been suggested as alternate sources since these ions can yield higher energy ν_e and $\bar{\nu}_e$ respectively, with lower values of the Lorentz boost γ [49, 50, 52, 53, 54, 55, 61, 66]. Details of the four beta-beam candidate ions can be found in Table 1.1. It may be possible to store radioactive ions producing beams with both polarities in the same ring. This will enable running the experiment in the ν_e and $\bar{\nu}_e$ modes simultaneously.

In the low γ design of beta-beams, the standard luminosity taken for the ^{18}Ne and ^{6}He are 1.1×10^{18} (ν_e) and 2.9×10^{18} ($\bar{\nu}_e$) useful decays per year, respectively [75]. We will discuss about this newly proposed facility later in great detail.

1.4 Neutrino : "NU" Horizons

We live in an exciting time when the light of new discoveries is breaking apart our long-held picture of the Standard Model. This revolution began in part with the widely confirmed assertion that neutrinos have mass, and it will continue to be waged by upcoming neutrino experiments. Spectacular results from a series of experiments over the last four decades [6, 8, 11, 17, 18, 19, 31, 36, 76, 77, 78, 79] have firmly established the phenomenon of neutrino oscillation and paved the way for the "golden" age of neutrino physics. Since neutrino oscillations can occur only if there is a mass difference between at least two neutrinos, an observation of this effect proves that at least one non-zero neutrino mass exists.

Neutrinos are strictly massless in the Standard Model of particle physics and the finite neutrino masses required by the experimental data provide the first hint for physics beyond the Standard Model, and make an extension of the theory necessary. No doubt that this has put the Standard Model in a paradoxical situation. Moreover, the fact that neutrino masses are so tiny (very much smaller than that of any other known fermion) should find an explanation in the new theory.

---

[1] A detailed R&D on this issue is being pursued by Mats Lindroos and his collaborators.

Recent discoveries on neutrinos might provide unique information on a more complete theory of elementary particles. The sensitivity of neutrino experiments to very tiny mass scales might provide the scope to learn something about physics at very high energy scales (i.e., at very small distances), which will never be accessible in particle accelerator experiments. Therefore, information from neutrinos is complementary to the one from accelerator experiments, and it may provide a key to a so-called Grand Unified Theory, in which the electromagnetic, the weak and the strong interactions are unified to one fundamental force.

Another puzzle of modern physics is the origin of matter. In the so-called Leptogenesis mechanism the origin of matter in the very first moments after the Big Bang is related to neutrinos. In that theory the small asymmetry between matter and anti-matter is generated by processes involving neutrinos in the early stage of the Universe. In this way a theory of neutrino may even provide the reason for our existence. Neutrinos have played a key role in shaping the Universe as we see today. We have just started our journey in the mysterious world of neutrinos, a tiny creature of Nature. A long journey is waiting for us ahead and many experimental approaches are required to get the full view. In the near future, the Large Hadron Collider (LHC) will start it's quest for Higgs and it is expected that the LHC will explore the mechanism of electroweak symmetry breaking and provide clues of new heavy degrees of freedom. This will certainly boost up the future road map of the neutrino physics programme and it is for sure that neutrino physics, a bit player on the physics stage in yesteryears, has now donned a central role and will play a crucial part in the high energy physics programme.

1.5 Layout of the Doctoral Work

We organize the description of the doctoral work in the following way. The first part of chapter 2 deals with the basic introduction to the quantum mechanics of neutrino oscillation in vacuum under both two and three flavour frameworks. Then we discuss the importance of matter effects in neutrino oscillations. In the second half of chapter 2 we take a look at our present understanding of neutrino parameters and we identify the major unknowns in the neutrino sector. Finally we close chapter 2 by giving a brief note on the future neutrino road-map based on long baseline experiments. In chapter 3 we underscore in detail the physics advantage of an experimental set-up where neutrinos produced in a beta-beam facility at CERN would be observed in the proposed large magnetized iron calorimeter detector (ICAL) at the India-based Neutrino Observatory (INO). The CERN-INO beta-beam set-up offers an excellent avenue to use the "Golden" channel ($\nu_e \to \nu_\mu$) oscillation probability for a simultaneous determination of the neutrino mass ordering and θ_{13}. The merit of the earth matter effects in the $\nu_{\rm e} \to \nu_{\rm e}$ survival probability at long baselines in order to cleanly determine the third leptonic mixing angle θ_{13} and the sign of the atmospheric neutrino mass squared difference, Δm^2_{31}, using a beta-beam as a ν_e source has been discussed in chapter 4. In chapter 5 we study the possibility of detecting new physics signals in a dedicated neutrino beta-beam experiment with the source at CERN and the detector at the proposed INO. These new physics signals arise in the R-parity violating supersymmetric models (RPVSM) [80] due to the flavor-changing neutral current (FCNC) and flavor-diagonal neutral current (FDNC) interactions of neutrinos with matter in the oscillation stage. In chapter 6 we show that a detector placed near a beta-beam storage ring can probe lepton number violating interactions that might crop up at the production and the detection point, as predicted by supersymmetric theories with R-parity non-conservation. Finally we end with the conclusion and an outlook in chapter 7.

Chapter 2

Neutrino Oscillations Revisited

This chapter is organized as follows. In the first section we discuss the role of neutrinos in the Standard Model. An introduction to the basic formalism of neutrino oscillations in vacuum has been given in the subsequent section. We consider both two and three flavour frameworks. In the following section we concentrate on the importance of matter effects in neutrino oscillations. Then we turn our focus on the present global understanding of the neutrino mass-mixing parameters. This is to set the stage for the next section where we take a drive to the unknown territories of the neutrino sector. Finally we take a look at the future neutrino road-map.

2.1 Neutrinos in the Standard Model

The Standard Model is a quantum field theory and it unifies strong, weak and electromagnetic interactions. The Standard Model is based on the gauge group $SU(3)_C \times SU(2)_L \times U(1)_Y$, broken spontaneously by the Higgs mechanism to $SU(3)_C \times U(1)_{em}$. The transformation groups $SU(3)_C$, $SU(2)_L$ and $U(1)_Y$ correspond to quantum numbers called colour, weak isospin and weak hypercharge (Y) respectively. Experimental observations suggest that the matter fields are fermionic, consisting of leptons and quarks. In the Standard Model, these leptons and quarks are chiral fermions :

$$\psi_{R,L} = \frac{1}{2}(1 \pm \gamma_5)\psi, \tag{2.1}$$

where $\psi = \psi_L + \psi_R$. The left-handed components transform as doublets under $SU(2)_L$, whereas the right-handed components are $SU(2)_L$ singlets. Within the framework of the Standard Model there are no right-handed neutrinos or left-handed antineutrinos. The particle content of the Standard Model is depicted in Table 2.1. It can be readily seen from Table 2.1 that neutrinos do not take part in strong and electromagnetic interactions and they only undergo weak interactions, that is, they are singlets of $SU(3)_C \times U(1)_{em}$. Precision data of the Z-decay width at the e^+e^- collider at LEP indicate that there are three neutrinos which take part in weak interactions. These are called the *active* neutrinos. Often a scenario with four neutrinos is discussed. So this fourth neutrino, if it exists, should be *sterile* to weak interactions. This

Particles	**Notation**	$SU(3)_C$	$SU(2)_L$	$U(1)_Y$	$U(1)_{em}$
Leptons	$l_L^I \equiv \begin{pmatrix} \nu^I \\ e^I \end{pmatrix}_L$	**1**	**2**	$-1/2$	**0** -1
	e_R^I	**1**	**1**	-1	-1
Quarks	$q_L^I \equiv \begin{pmatrix} u^I \\ d^I \end{pmatrix}_L$	**3**	**2**	$1/6$	$2/3$ $-1/3$
	u_R^I	**3**	**1**	$2/3$	$2/3$
	d_R^I	**3**	**1**	$-1/3$	$-1/3$

Table 2.1: Matter contents of the Standard Model with their corresponding gauge quantum numbers. $I = 1, 2, 3$ is the generation index. The electromagnetic charge listed in the last column is defined as $Q_{em} = T_3 + Y$.

sterile neutrino does not have any Standard Model interactions and passes undetected through the experimental set up.

In weak interactions, parity is maximally violated and only the left-handed states do couple with the gauge bosons $W^{\pm}$ while the right-handed states do not, unlike in the case of electromagnetism where both the states couple to the photon with the same strength. The unbroken electromagnetic gauge symmetry ensures the masslessness of photon. But no such fundamental principle predicts the neutrino to be massless. In the mass-term, the left- and right-handed chiral states are coupled to each other in the following way :

$$m\bar{\psi}\psi = m(\bar{\psi}_L\psi_R + \bar{\psi}_R\psi_L), \tag{2.2}$$

which can be easily obtained with the help of Eq. 2.1 and using the properties of γ_5. Therefore the existence of both left-handed and right-handed chiral components is mandatory to have a nonzero mass of a fermion. But within the Standard Model there is no right-handed neutrino and as a consequence the neutrino does not have any mass. So non-zero neutrino mass, as required by the neutrino oscillation data, indicates the existence of physics beyond the Standard Model.

As we have already mentioned, the Standard Model has three active neutrinos accompanying the charged lepton mass eigenstates, e, μ and τ. Therefore there is a possibility of weak CC interactions between the neutrinos and their corresponding charged leptons which is given by :

$$-\mathcal{L}_{CC} = \frac{g}{\sqrt{2}} \sum_I \bar{\nu}_{LI} \gamma^{\mu} \ell^-_{LI} W^+_{\mu} + h.c.. \tag{2.3}$$

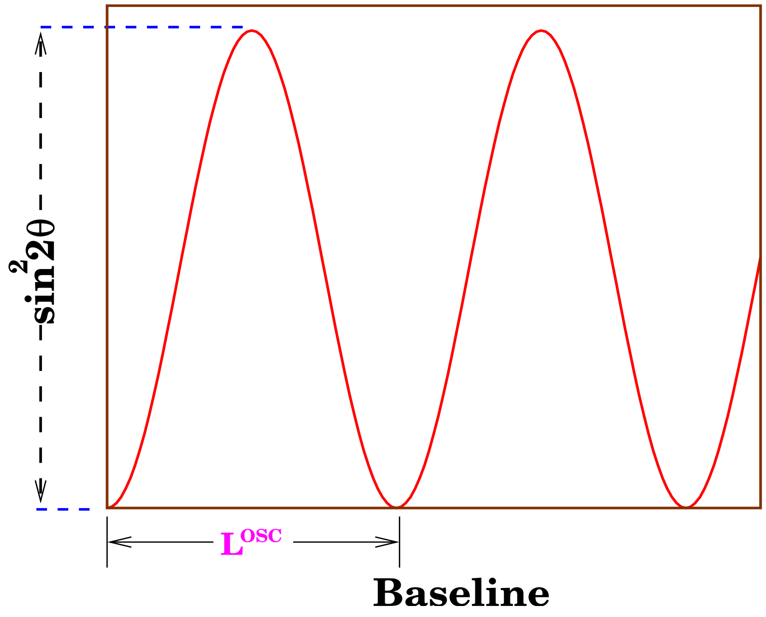

Figure 2.1: The two flavour ν_e to ν_μ oscillation probability (Eq. 2.14). The mixing angle θ governs the oscillation amplitude and the frequency depends on $\Delta m^2_{12} = m_2^2 - m_1^2$, where m_1 and m_2 are the masses of the mass eigenstates ν_1 and ν_2 respectively.

The Standard Model neutrinos also have NC interactions :

$$-\mathcal{L}_{NC} = \frac{g}{2\cos\theta_W}\sum_I \bar{\nu}_{LI}\gamma^\mu \nu_{LI} Z^0_\mu. \tag{2.4}$$

Thus, within the Standard Model, all the neutrino interactions are described by Eqs. 2.3 and 2.4.

2.2 Oscillations in Vacuum

Neutrino oscillation is a simple quantum mechanical phenomenon in which neutrino changes flavour as it propagates. In 1957, Pontecorvo [81] gave the concept of neutrino oscillation based on a two-level quantum system. This phenomenon arises if neutrinos have masses and there is mixing.

In the course of time evolution of a stationary state $|\Psi_k\rangle$ (which is one of the eigenstates of the hamiltonian of a system with the energy eigenvalue E_k), it will remain in the same state and will be associated with a phase in the form ($\hbar = c = 1$) :

$$|\Psi_k(t)\rangle = e^{-iE_k t}|\Psi_k(0)\rangle. \tag{2.5}$$

Now if we deal with an arbitrary non-stationary state of the system which is a superposition of say two eigenstates (with eigenenergies E_1 and E_2) of the hamiltonian of the system, then it will not be in the same state after time evolution. The chances that the system will remain in it's initial state will be an oscillatory function of time with frequency $(E_2 - E_1)$.

In order to implement this mechanism in case of neutrinos, we consider the fact that neutrinos $(\nu_e, \nu_\mu, \nu_\tau)$ are produced or detected via weak interactions and therefore they are referred to as weak-eigenstate neutrinos (denoted as ν_α) that means they are the weak doublet-partners of e^-, μ^-, τ^- respectively. In such a scenario, if we assume that neutrinos are massive, then in general, it is not mandatory that the mass-matrix of neutrinos written in this weak (flavour) basis will have to be diagonal. So, it follows that the mass eigenstate neutrinos $\nu_i, i = 1, 2, 3$ (the basis in which the neutrino mass matrix is diagonal) are not identical to the weak or flavour basis[1] and we have for n number of light neutrino species

$$|\nu_\alpha\rangle = \sum_{i=1}^{n} U^*_{\alpha i}|\nu_i\rangle, \tag{2.6}$$

where U is the unitary leptonic mixing matrix known as the Pontecorvo-Maki-Nakagawa-Sakata (PMNS) matrix [82]. This matrix is analogous to the CKM matrix in the quark sector. Because of Eq. 2.6, the probability of finding a neutrino created in a given flavour state to be in the same state (or any other flavour state) oscillates with time. Suppose a given source is producing a neutrino flux of given flavour $|\nu_\alpha\rangle$ at $t = x = 0$, the neutrino state at a later time t is then

$$|\nu_\alpha(t)\rangle = \sum_{i=1}^{n} U^*_{\alpha i}|\nu_i(t)\rangle = \sum_{i=1}^{n} U^*_{\alpha i} e^{-iE_i t}|\nu_i(0)\rangle, \tag{2.7}$$

and propagates as an admixture of the mass eigenstates. The neutrino oscillation probability, i.e. the transformation probability of a flavour eigenstate neutrino $|\nu_\alpha\rangle$ into another one $|\nu_\beta\rangle$ is then

$$P_{\alpha\beta} = |\langle\nu_\beta|\nu_\alpha(t)\rangle|^2 = |\sum_{i=1}^{n}\sum_{j=1}^{n} U^*_{\alpha i}U_{\beta j}\langle\nu_j|\nu_i(t)\rangle|^2 . \tag{2.8}$$

To obtain the oscillation probability for antineutrinos one has to replace U by U^*. For ultra-relativistic neutrinos with small mass one can assume $p_i \simeq p_j \equiv p \simeq E$ and we have

$$E_i = \sqrt{p_i^2 + m_i^2} \simeq p + \frac{m_i^2}{2E}, \tag{2.9}$$

where E_i and m_i are, respectively, the energy and the mass of the neutrino mass eigenstate ν_i.

Now using the orthogonality relation $\langle\nu_j|\nu_i\rangle = \delta_{ij}$ and with the help of Eq. 2.9, we obtain the transition probability that an initial ν_α of energy E gets converted to a ν_β after traveling a distance $L(= t)$ in vacuum as

$$\begin{aligned} P_{\alpha\beta} = \delta_{\alpha\beta} \quad &- \quad 4\sum_{i<j}^{n} \mathrm{Re}[U^*_{\alpha i}U^*_{\beta j}U_{\beta i}U_{\alpha j}] \sin^2 X_{ij} \\ &+ \quad 2\sum_{i<j}^{n} \mathrm{Im}[U^*_{\alpha i}U^*_{\beta j}U_{\beta i}U_{\alpha j}] \sin 2X_{ij} \,, \end{aligned} \tag{2.10}$$

---

[1] The charged lepton mass-matrix is diagonal in this basis.

where

$$X_{ij} = \frac{(m_i^2 - m_j^2)L}{4E} = 1.27\,\frac{\Delta m_{ij}^2}{eV^2}\,\frac{L/E}{m/MeV}\,. \tag{2.11}$$

$\Delta m_{ij}^2 = m_i^2 - m_j^2$ is known as the mass splitting and neutrino oscillations are only sensitive to this mass squared difference but not to the absolute neutrino mass scale. The transition probability (depicted by Eq. 2.10) has an oscillatory behaviour with oscillation lengths

$$L_{ij}^{osc} = \frac{4\pi E}{\Delta m_{ij}^2} \simeq 2.48\ m\,\frac{E\,(\mathrm{MeV})}{\Delta m_{ij}^2\,(\mathrm{eV}^2)} = 2.48\ km\,\frac{E\,(\mathrm{GeV})}{\Delta m_{ij}^2\,(\mathrm{eV}^2)} \tag{2.12}$$

and the amplitudes are proportional to the elements in the mixing matrix. Since neutrino oscillations can occur only if there is a mass difference between at least two neutrinos, an observation of this effect proves that at least one non-zero neutrino mass exists.

In general, to construct a unitary $n \times n$ matrix we need $n(n-1)/2$ angles and $n(n+1)/2$ phases. If neutrinos are Dirac type in nature then $2n-1$ phases can be absorbed by a proper re-phasing of the left-handed fields, leaving $(n-1)(n-2)/2$ physical phases. Therefore CP violation is only possible in the case of $n \geq 3$ generations. In the Majorana case there is no freedom to re-phase the neutrino fields; only n phases can be removed using the charged lepton fields, leaving $n(n-1)/2$ physical phases. Out of these $(n-1)(n-2)/2$ are the usual Dirac phases, while $n-1$ are specific to the Majorana case and are called Majorana phases. The latter do not lead to any observable effects in neutrino oscillations and are not discussed further in this thesis.

2.2.1 Two-Flavour case

In a simple case with only two families of neutrinos, the mixing matrix depends on a single parameter θ (known as the mixing angle),

$$U = \begin{pmatrix} \cos\theta & \sin\theta \\ -\sin\theta & \cos\theta \end{pmatrix} \tag{2.13}$$

and there is a single mass-squared difference Δm^2. Using this form of U in Eq. 2.10, one obtains

$$P_{\nu_\alpha \to \nu_\beta} = \sin^2 2\theta\ \sin^2(1.27\Delta m^2 \frac{L}{E}), \tag{2.14}$$

$$P_{\nu_\alpha \to \nu_\alpha} = 1 - \sin^2 2\theta\ \sin^2(1.27\Delta m^2 \frac{L}{E}), \tag{2.15}$$

where Δm^2 is in eV^2, L is in m (km) and E in MeV (GeV). In the above equations, θ and Δm^2 (these are fundamental constants like the electron mass or the Cabibbo-angle) determine the oscillation amplitude and frequency respectively (see figure 2.1). The various neutrino sources like the Sun, the atmosphere, reactors and accelerators (discussed in the previous chapter) provide neutrinos with average energy varying in a wide range and the distances between the sources and the detectors are also quite different which offer the possibility to probe various oscillation frequencies. In order to penetrate a given value of Δm^2, the experiment has to be performed with $E/L \approx \Delta m^2$ which is equivalent to $L \sim L^{osc}$.

In an oscillation experiment, if we search for a new flavour then we call it an appearance experiment. On the other hand if we look for a reduction in the neutrino flux from the source then it is known as a disappearance experiment. In both the cases, the measurement of Δm^2 and θ are correlated with each other. Therefore an error in measuring one of the parameters causes an additional uncertainty on the other one. To locate the position of the peak clearly, we need an experiment with good enough energy resolution ($\Delta E \ll L\Delta m^2$) otherwise the information on Δm^2 gets blurred and the experimental signal becomes energy independent ($\sim \frac{1}{2}\sin^2 2\theta$). The proper energy calibration of the detector (it provides the absolute energy scale) is also a very crucial issue while measuring the mass splitting. We can probe very small values of θ with an appearance experiment because the measurement is done relative to zero. On the contrary, a disappearance experiment measures relative to unity. Therefore the impact of certain systematical errors is quite different in both the cases. In an appearance experiment, the signal is proportional to θ and therefore an accurate understanding of the level of background is very vital while measuring small values of θ. But in case of a disappearance measurement the issue of total normalization is crucial because a large normalization error makes it tough to detect deviations from unity.

2.2.2 Three-Flavour case

Let us now consider the case of three neutrino flavours. In a three neutrino framework, the 3×3 unitary mixing matrix U depends on three mixing angles θ_{12}, θ_{13} and θ_{23} and one CP-violating phase δ_{CP} (ignoring Majorana phases). The mixing matrix U can be parameterized as

$$U = V_{23} W_{13} V_{12}, \tag{2.16}$$

where

$$V_{12} = \begin{pmatrix} c_{12} & s_{12} & 0 \\ -s_{12} & c_{12} & 0 \\ 0 & 0 & 1 \end{pmatrix}, W_{13} = \begin{pmatrix} c_{13} & 0 & s_{13}e^{-i\delta_{CP}} \\ 0 & 1 & 0 \\ -s_{13}e^{i\delta_{CP}} & 0 & c_{13} \end{pmatrix}, V_{23} = \begin{pmatrix} 1 & 0 & 0 \\ 0 & c_{23} & s_{23} \\ 0 & -s_{23} & c_{23} \end{pmatrix}. \tag{2.17}$$

$c_{ij} = \cos\theta_{ij}$ and $s_{ij} = \sin\theta_{ij}$. The neutrino mixing matrix takes the form

$$U = \begin{pmatrix} c_{12}c_{13} & s_{12}c_{13} & s_{13}e^{-i\delta_{CP}} \\ -s_{12}c_{23} - c_{12}s_{23}s_{13}e^{i\delta_{CP}} & c_{12}c_{23} - s_{12}s_{23}s_{13}e^{i\delta_{CP}} & s_{23}c_{13} \\ s_{12}s_{23} - c_{12}c_{23}s_{13}e^{i\delta_{CP}} & -c_{12}s_{23} - s_{12}c_{23}s_{13}e^{i\delta_{CP}} & c_{23}c_{13} \end{pmatrix}. \tag{2.18}$$

The probabilities of oscillations between various flavour states are given by Eq. 2.10. For three neutrino species, one can identify $\Delta m^2_{\odot} = \Delta m^2_{21} > 0$ as the neutrino mass squared difference responsible for the solar neutrino oscillations and the dominant atmospheric neutrino oscillations are caused by the $|\Delta m^2_A| = |\Delta m^2_{31}| \cong |\Delta m^2_{32}| \gg \Delta m^2_{21}$. $\theta_{12} = \theta_\odot$ and $\theta_{23} = \theta_A$ are the solar and atmospheric neutrino mixing angles, respectively. The angle θ_{13} is the so-called "CHOOZ mixing angle" which connects the solar sector with the atmospheric one and determines the impact of the three flavour effects. Three flavour effects leave their imprints in an experiment which is sensitive to both the mass splittings. It is true that for the precision measurements of the mass squared differences or the two large mixing angles, these effects are not that vital but they can play a key role in the determination of the small mixing angle and in many cases, they decide the fate of an experiment. Like in the quark sector, in the case of three generations there can be CP-violation in the neutral lepton sector provided that θ_{13} and the CP phase δ_{CP} are non-zero. If CP is not conserved, the oscillation probabilities for neutrinos are different from those for antineutrinos. The CP-odd asymmetries are defined as

$$\Delta P_{\alpha\beta} \equiv P(\nu_\alpha \to \nu_\beta;\, L) - P(\bar{\nu}_\alpha \to \bar{\nu}_\beta;\, L)\,. \tag{2.19}$$

CPT invariance ensures that $\Delta P_{\alpha\beta} = -\Delta P_{\beta\alpha}$. With the help of Eq. 2.18 we have

$$\Delta P_{e\mu} = \Delta P_{\mu\tau} = \Delta P_{\tau e} = 4 J_{CP} \times \left[\sin\left(\frac{\Delta m^2_{21}}{2E} L\right) + \sin\left(\frac{\Delta m^2_{32}}{2E} L\right) + \sin\left(\frac{\Delta m^2_{13}}{2E} L\right) \right]\,, \tag{2.20}$$

where

$$J_{CP} = \frac{1}{8} \cos\theta_{13}\, \sin 2\theta_{13}\, \sin 2\theta_{23}\, \sin 2\theta_{12}\, \sin\delta_{CP} \tag{2.21}$$

which is known as Jarlskog CP-odd invariant [83]. One can easily draw the following conclusions by observing Eq. 2.20.

1. The CP-odd asymmetry vanishes if δ_{CP} is zero or 180° and it comes with full strength if δ_{CP} equals to 90° or 270°.
2. It vanishes if any of the mixing angles θ_{12}, θ_{13} or θ_{23} is zero or 90°. This indicates that we need at least three generations to observe CP-violation which is suppressed by the smallest of the mixing angles, θ_{13}.
3. The mass squared differences satisfy the relation $\Delta m^2_{21} + \Delta m^2_{32} + \Delta m^2_{13} = 0$. Therefore, if any one of the Δm^2_{ij} is zero then the CP-odd asymmetry vanishes immediately. It ensures the fact that the three flavour effects are essential for probing the leptonic CP-violation.

There is no doubt that it would be of great importance if we can establish the CP-nonconservation in the leptonic sector and future long baseline neutrino oscillation experiments will provide a crucial hint along this direction.

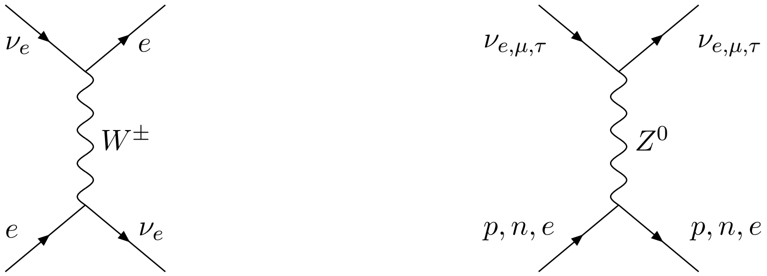

Figure 2.2: Feynman diagrams showing neutrino scattering inside the matter. Left panel depicts CC interactions whereas right panel describes NC processes.

Medium	**Matter Density**	V_{CC}
Solar core	~ 100 g/cm^3	$\sim 10^{-12}$ eV
Earth core	~ 10 g/cm^3	$\sim 10^{-13}$ eV
Supernova	$\sim 10^{14}$ g/cm^3	$\sim$ eV

Table 2.2: The impact of matter potential in various mediums.

2.3 Oscillations in Matter

Neutrino propagation through matter can modify oscillations significantly. When neutrinos travel through matter (*e.g.* in the Sun, Earth or a supernova), the weak interaction couples the neutrinos to matter and besides few hard scattering events there is also coherent forward elastic scattering of neutrinos with matter particles they encounter along the way. This motion of neutrinos can be compared with the visible light traveling through glass. The crucial point to be noted here is that the coherent forward elastic scattering amplitudes are not the same for all neutrino flavours. The ordinary matter consists of electrons, protons and neutrons but it does not contain any muons or tau-leptons. One can readily see from the right panel of Fig. 2.2 that neutrinos of all three flavours (ν_e, ν_μ and ν_τ) interact with the electrons, protons and neutrons of matter through flavour independent NC interaction mediated by Z^0 bosons and these contributions are same for neutrinos of all three flavours and therefore these interactions do not have any impact on neutrino oscillation probabilities. Interestingly, the electron neutrinos have an additional contribution due to their CC interactions (see left panel of Fig. 2.2) with the ambient electrons of the medium which are mediated by the $W^{\pm}$ exchange. This extra matter potential comes in the form

$$A = \pm 2\sqrt{2} G_F N_e E \,, \tag{2.22}$$

where G_F is the Fermi coupling constant, N_e is the electron number density inside the Earth and E is the neutrino energy. The $+$ sign refers to neutrinos while the $-$ to antineutrinos. The electron density (N_e) is connected to the matter density (ρ) in the following way

$$V_{CC} = \sqrt{2} G_F N_e \simeq 7.6 Y_e \frac{\rho}{10^{14}\mathrm{g/cm^3}} \mathrm{eV} \,, \tag{2.23}$$

where $Y_e = \frac{N_e}{N_p+N_n}$ is the relative number density. N_p, N_n are the proton and neutron densities in Earth matter respectively. In an electrically neutral, isoscalar medium, we have $N_e = N_p = N_n$ and Y_e comes out to be 0.5. The strength of V_{CC} inside the Sun, Earth and a supernova is given in Table 2.2. If we compare V_{CC} with $\Delta m^2/2E$ then we can evaluate the importance of matter effects on neutrino oscillations. If we consider a neutrino of 5 GeV passing through the core of the Earth then V_{CC} is comparable with $\Delta m^2/2E$ ($= 2.5 \times 10^{-13}$ eV if $\Delta m^2 = 2.5 \times 10^{-3}$ eV^2).

Staying in the two-flavour formalism, the time evolution of the flavour eigenstates in matter is given by the following Schrödinger equation

$$i\frac{d}{dt}\begin{pmatrix}\nu_\alpha\\ \nu_\beta\end{pmatrix} = \frac{1}{2E}\left[U\begin{pmatrix}m_1^2 & 0\\ 0 & m_2^2\end{pmatrix}U^\dagger + \begin{pmatrix}A(t) & 0\\ 0 & 0\end{pmatrix}\right]\begin{pmatrix}\nu_\alpha\\ \nu_\beta\end{pmatrix}, \tag{2.24}$$

where U is the mixing matrix defined by Eq. 2.13. In the constant matter density case the problem boils down to a stationary one and a trivial diagonalization of the Hamiltonian is required to obtain the solution. In the presence of matter, the vacuum oscillation parameters are mapped to the new parameters[2] in the following way

$$\begin{aligned}(\Delta m^2)^m &= \sqrt{(\Delta m^2\cos 2\theta - A)^2 + (\Delta m^2 \sin 2\theta)^2},\\ \sin 2\theta^m &= \sin 2\theta\ \Delta m^2/(\Delta m^2)^m.\end{aligned} \tag{2.25}$$

The so-called MSW-resonance [10] condition is met at

$$\Delta m^2 \cos 2\theta = A. \tag{2.26}$$

At MSW-resonance, $\sin 2\theta^m = 1$ (from Eq. 2.25 and 2.26) which immediately signifies that independent of the value of the vacuum mixing angle θ, the mixing in matter is maximal *i.e.* $\theta^m = \pi/4$. This resonance occurs for neutrinos (antineutrinos) if Δm^2 is positive (negetive). So the sign of Δm^2 determines the oscillation probability. From Eq. 2.26, the resonance energy can be expressed as

$$E_{res} = 11.16\text{GeV}\left[\frac{|\Delta m^2|}{2.5\times 10^{-3}\text{eV}^2}\right]\cdot\left[\frac{\cos 2\theta}{0.95}\right]\cdot\left[\frac{2.8\ \text{g/cm}^3}{\rho}\right]. \tag{2.27}$$

In course of neutrino propagation through the upper Earth mantle with $\rho = 2.8$ g/cm^3, the resonance occurs at roughly 11.2 GeV provided that $|\Delta m^2| = 2.5 \times 10^{-3}$eV^2 and $\cos 2\theta = 0.95$. The matter effect arises due to matter and not anti-matter and this fact is responsible for the observed asymmetry between neutrino and antineutrino oscillation probabilities even in the two neutrino case.

In the presence of three neutrinos the time evolution of flavour eigenstates in matter can be written as

$$i\frac{d}{dt}\begin{pmatrix}\nu_e\\ \nu_\mu\\ \nu_\tau\end{pmatrix} = \frac{1}{2E}\left[U\begin{pmatrix}m_1^2 & 0 & 0\\ 0 & m_2^2 & 0\\ 0 & 0 & m_3^2\end{pmatrix}U^\dagger + \begin{pmatrix}A(t) & 0 & 0\\ 0 & 0 & 0\\ 0 & 0 & 0\end{pmatrix}\right]\begin{pmatrix}\nu_e\\ \nu_\mu\\ \nu_\tau\end{pmatrix}, \tag{2.28}$$

---

[2] The new parameters in matter carry a superscript m.

Parameter	Best fit	3σ (1 d.o.f)
Δm^2_{21} [10^{-5} eV^2]	7.6	7.1–8.3
$\|\Delta m^2_{31}\|$ [10^{-3} eV^2]	2.4	2.0–2.8
$\sin^2\theta_{12}$	0.32	0.26–0.40
$\sin^2\theta_{23}$	0.50	0.34–0.67
$\sin^2\theta_{13}$	0.007	≤ 0.050

Table 2.3: Best-fit values and 3σ(1 d.o.f) constraints on the oscillation parameters under three-flavour scheme from global data including solar, atmospheric, reactor (KamLAND and CHOOZ) and accelerator (K2K and MINOS) experiments. This table has been taken from [79].

where U is the mixing matrix defined by Eq. 2.18. Even in the constant matter density case, it is very tough to obtain the analytical solution of the above equation. Under certain approximations, it is possible to obtain some expressions which are quite useful in explaining the underlying physics. In the next chapter, we will discuss a few such cases in detail. In the case of three flavours, besides the genuine CP asymmetry caused by the CP phase δ_{CP}, we also have fake CP asymmetry induced by matter which causes obstacles in extracting the information on δ_{CP}. Now let us see what is our current understanding of these various neutrino mass-mixing parameters?

2.4 Present Status

Neutrino physics has entered the precision era, with the thrust now shifting to detailed understanding of the structure of the neutrino mass matrix, accurate reconstruction of which would shed light on the underlying new physics that gives rise to neutrino mass and mixing. The full mass matrix is given in terms of nine parameters, the three neutrino masses, the three mixing angles and the three CP violating phases. Neutrino oscillation experiments are sensitive to only two mass squared differences, all the three mixing angles and the so-called Dirac CP phase. The remaining parameters, comprising of the absolute neutrino mass scale and the two so-called Majorana phases, have to be determined elsewhere. We already have very good knowledge on the two mass squared differences and two of the three mixing angles. Results from solar neutrino experiments [17, 19] which have been collecting data for more than four decades have now culminated in choosing the Large Mixing Angle (LMA) solution. The latest addition to this huge repertoire of experimental data is the result from the on-going Borexino experiment [18], and this result is consistent with the LMA solution. This conclusion from solar neutrino experiments has been corroborated independently by the KamLAND reactor antineutrino experiment [8, 9], and a combined analysis of the solar and KamLAND data gives as best-fit $\Delta m^2_{21} = 7.6 \times 10^{-5}$ eV^2 and $\sin^2\theta_{12} = 0.32$ [9, 78, 79]. The other mass squared difference Δm^2_{31} and mixing angle θ_{23} are now pretty well determined by the zenith angle dependent atmospheric ν_μ data in SuperKamiokande [6, 19, 84] and the long baseline experiments K2K [11, 77] and MINOS [36]. The combined data from the atmospheric and long baseline experiments have pinned down $|\Delta m^2_{31}| = 2.4 \times 10^{-3}$ eV^2 and $\sin^2 2\theta_{23} = 1$. Our knowledge on the third mixing angle θ_{13} is restricted to an upper bound of $\sin^2\theta_{13} < 0.033$ from the global analysis of all solar, atmospheric, long baseline and reactor data, including the CHOOZ [31, 76] results in particular. We do not have any information on δ_{CP} and it is fully unconstrained yet. All the best-fit values and 3σ(1 d.o.f) constraints on the oscillation parameters under a three-flavour scheme from global data including solar, atmospheric, reactor (KamLAND and CHOOZ) and accelerator (K2K and MINOS) experiments have been summarized in Table 2.3. Recent cosmological observations (WMAP 5-year and other data) predict that the sum of three neutrino masses would be less than 0.19 eV [85]. In the next section, we will focus on the major unknowns in the neutrino sector that we would like to resolve in the next ten to fifteen years down the line.

2.5 Missing Links

Despite the spectacular achievements in the last ten years or so, a lot of information is still required to complete our understanding of the neutrino sector. In the following, we have to tried to list them up :

- Are the neutrinos Dirac or Majorana particles?
- How many neutrino species are there? Do sterile neutrinos exist? Are three-flavour oscillations enough?
- What is the mass scale of the neutrinos? Why are neutrino masses so small?
- Does the neutrino have a non-zero magnetic moment?
- Why is the pattern of the neutrino mixing so different from that of the quarks? Is there any connection between quarks and leptons?
- What are the precise values of Δm^2_{21} and $\sin^2\theta_{12}$?
- What is the precise value of $|\Delta m^2_{31}|$? What is the sign of Δm^2_{31} or the character of the neutrino mass hierarchy?
- Is the ordering of the neutrino mass states hierarchical or quasi-degenerate?
- Is $\sin^2 2\theta_{23}$ exactly maximal (= 1)? If $\sin^2 2\theta_{23} \neq 1$, what is its octant?
- How tiny is $\sin^2 2\theta_{13}$? Is it zero? If it is non-zero then what is the precise value of θ_{13}?
- Does the behaviour of neutrinos violate CP? Can we probe the existence of the three CP odd phases?
- Is there any link between the low energy CP violation in the neutral lepton sector and the observed matter anti-matter asymmetry (baryon asymmetry) in the universe ?

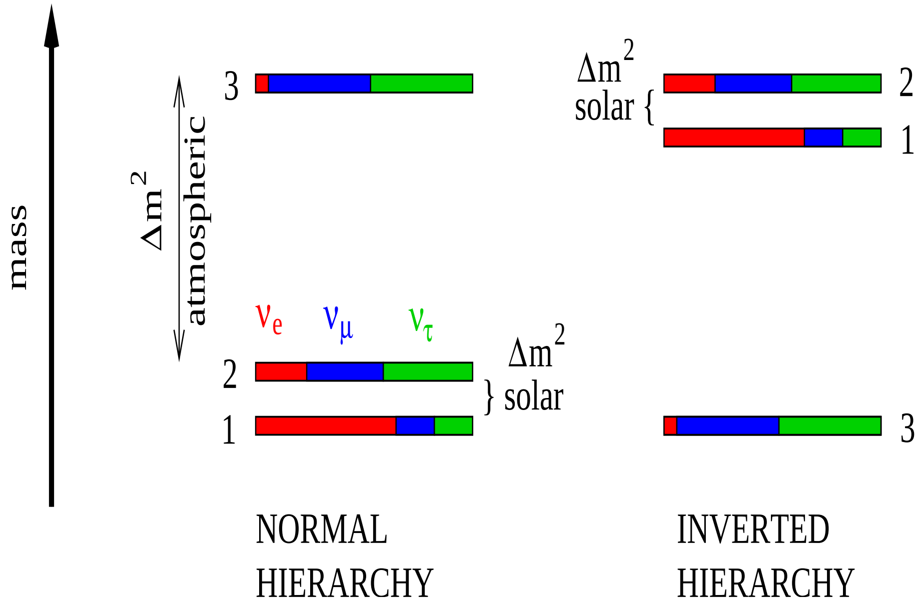

Figure 2.3: The sign of $\Delta m_{31}^2 = m_3^2 - m_1^2$ is not known. The neutrino mass spectrum can be normal or inverted hierarchical.

- Can we probe the sub dominant effects due to possible new physics in the next generation high precision neutrino oscillation experiments?
- What is the importance of neutrino physics in our understanding of dark matter and dark energy?
- Is there any connection between neutrino mass and leptogenesis and galaxy-cluster formation?
- What is the role of neutrinos in connecting the predictions at the grand-unification scale with low energy phenomena in the framework of see-saw mechanism and supersymmetric extensions of the Standard Model?

Out of these several unanswered questions (listed above), there are several issues which can be answered in the future dedicated long baseline neutrino oscillation experiments. Let us discuss a few of them. While the solar neutrino data have confirmed that $\Delta m_{21}^2 > 0$ at a C.L. of more than 6σ, we still do not know what is the sign of Δm_{31}^2, *i.e.*, the neutrino mass hierarchy[3]. Knowing the ordering of the neutrino masses is of prime importance, because it dictates the structure of the neutrino mass matrix, and hence could give vital clues towards the underlying theory of neutrino masses and mixing. Knowing the $sgn(\Delta m_{31}^2)$ could have other far-reaching phenomenological consequences. For instance, if it turns out the $\Delta m^2_{31} < 0$ and yet neutrino-less double beta-decay is not observed even in the very far future experiments, that would be a strong hint that the neutrinos are not Majorana particles (see for *e.g.* [86] and references therein). A vital task to be undertaken in the immediate future is the determination of the hitherto unknown mixing angle θ_{13}. Discovery of a non-zero value for θ_{13} would open up the possibility of observing CP-violation in the lepton sector. Non-zero θ_{13} also brings in the possibility of large Earth matter effects [10, 87] for GeV energy accelerator neutrinos traveling over long distances. Effect of matter on neutrino oscillations depends on the $\text{sgn}(\Delta m^2_{31})$ and is opposite for neutrinos and antineutrinos. For a given $\text{sgn}(\Delta m^2_{31})$ it enhances the oscillation probability in one of the channels and suppresses it in the other. Therefore, comparing the neutrino signal against the antineutrino signal in very long baseline experiments gives us a powerful tool to determine $\text{sgn}(\Delta m^2_{31})$. A way to judge the merit of an experiment is by observing it's limiting reach in the small mixing angle θ_{13} where it is still sensitive to the mass ordering and the leptonic CP-violation.

---

[3] Though we call this the neutrino mass *hierarchy*, what we mean is basically the *ordering* of the neutrino mass states (see Fig. 2.3). Therefore, our discussions are valid for both hierarchical as well as quasi-degenerate mass spectra. We define $\Delta m_{ij}^2 = m_i^2 - m_j^2$ and refer to $sgn(\Delta m_{31}^2)$ as the neutrino mass hierarchy – $sgn(\Delta m_{31}^2) > 0$ is called "normal hierarchy" (NH) while $sgn(\Delta m_{31}^2) < 0$ is called "inverted hierarchy" (IH).

2.6 Future Neutrino Road-Map

Determining the unknown mixing angle θ_{13}, the CP phase δ_{CP}, and the neutrino mass ordering have emerged as the next frontiers in this field. All these three quantities can be probed by experimentally measuring the so-called "golden" channel [88] oscillation probability $P_{e\mu}$ ($\nu_e \to \nu_\mu$) or its T-conjugate channel $P_{\mu e}$. A series of ambitious projects are under discussion which plan to use this oscillation channel. The on-going and near future experiments include the MINOS experiment in the US [36], and the CNGS experiments ICARUS [38] and OPERA [37] in Europe. Next experiments in line will be T2K in Japan [39] and NOνA in US [40]. All these experiments will use muon neutrino beams from conventional accelerator sources in order to observe $P_{\mu e}$. Collectively and in combination with short-baseline reactor experiments, such as Double Chooz [89], these experiments are expected to improve the bound on θ_{13} to about $\sin^2 2\theta_{13} < 0.01$ (90% CL) [90]. The mass hierarchy and CP violation, though in principle accessible using the combined data from the T2K and NOνA experiments, can be determined only for values[4] of $\sin^2 2\theta_{13}(\text{true})$ close to the current bound and for some fraction of the possible values of the CP phase $\delta_{CP}(\text{true})$. The sensitivity of these experiments is mainly restricted by statistics, while for larger luminosity set-ups, the intrinsic ν_e background poses a natural limitation for experiments sensitive to ν_μ oscillations into ν_e. Therefore, if Nature has not been very kind we will need larger sophisticated experiments to complete our understanding of the neutrinos, possibly using an alternate smart technology with powerful, well measured neutrino beams from upgraded accelerator facilities and improved detector technologies. The beta-beam and neutrino factory can play a crucial role in this direction in future. A summary of the potential of selected neutrino factory and beta-beam set-ups have been compiled by the physics working group of the International Scoping Study for a future neutrino Factory, superbeam and beta-beam, in their report [71]. In the next chapter, we will expound in detail the physics reach of an experimental set-up in which the proposed large magnetized iron detector at the India-based Neutrino Observatory (INO) [25] would serve as the far detector for a CERN-based monoflavour beta-beam [45].

---

[4] We distinguish between the "true" values of the oscillation parameters, which are the values chosen by Nature, and their fitted values. Throughout this work we denote the true value of a parameter by putting "(true)" after the symbol for the parameter.

Chapter 3

Neutrino mass ordering and θ_{13} with a magical Beta-beam experiment at INO

3.1 Introduction

The most promising avenue for the determination of θ_{13}, the CP phase δ_{CP} and sgn(Δm^2_{31}) is the $\nu_e \to \nu_\mu$ oscillation channel $P_{e\mu}$ (or its T-conjugate $P_{\mu e}$), often referred to in the literature as the "golden channel" [88]. The $P_{e\mu}$ channel can be studied in experiments which use an initial ν_e (or $\bar{\nu}_e$) beam and a detector which can efficiently see muons[1]. Also in order to probe small values of $\sin^2 2\theta_{13}$, one needs the following :

1. **Low backgrounds**

   As far as the low background requirement is concerned, it is an advantage to use a pure flavor neutrino beam without any intrinsic beam contamination. A beta-beam [45] is well suited for this purpose. An alternative approach is the so-called neutrino factory [41]. The detector backgrounds coming mainly from neutral current interactions and mis-identification of particles, can be reduced by imposing intelligent cuts. The atmospheric neutrino backgrounds, which can be important for beta-beams at lower energies, can be suppressed using timing and directional information.

2. **Large statistics**

   Statistics can be increased by a higher beam power and the size and efficiency of the detector.

3. **Reduced systematical uncertainties**

---

[1] This is complementary to the standard accelerator beams where the initial (anti)neutrino flux consists of ν_μ (or $\bar{\nu}_\mu$) and where the relevant channel is the probability $P_{\mu e}$. Produced from decay of accelerated pions, these conventional (anti)neutrino beams suffer from an additional hurdle of an intrinsic ν_e ($\bar{\nu}_e$) contamination, which poses a serious problem of backgrounds. A beta-beam is comprised of pure ν_e (or $\bar{\nu}_e$).

Beam-related systematic uncertainties can be reduced to a large extent by working with a two detector set-up, one very close to the beam line and another serving as the far detector. The systematic uncertainties coming from the lack of knowledge of the neutrino-nucleus interaction cross-sections are another important source of error. These can be controlled to some degree by the near-far two detector set-up, but they cannot be canceled completely [91].

For a beta-beam, a variety of plausible set-ups have been proposed in the literature [46, 47, 48, 49, 50, 51, 52, 53, 54, 55, 56, 57, 58, 59, 60, 61, 62, 63, 64, 65, 66, 67]. The proposal which poses minimal challenge for the beta-beam design, is the commonly called CERN-MEMPHYS project [47, 58, 59]. It proposes to use the EURISOL ion source to produce the radioactive source ions ^{18}Ne and ^{6}He, and demands a Lorentz boost factor $\gamma \simeq 100$ for them, which can be produced using the existing accelerator facilities at CERN. The far detector MEMPHYS, a megaton water detector with fiducial mass of 440 kton, will have to be built in the Fréjus tunnel, at a distance of 130 km from CERN. Another possible beta-beam set-up using water detector but higher boost factors and an intermediate baseline option was put forth in [62, 63] (see also [66]). In these papers authors have used a high γ ^{18}Ne and ^{6}He beta-beam option at CERN and 440 kton fiducial volume water detector at GranSasso or Canfranc, which corresponds to $L =$ 730 and 650 km respectively. Excellent sensitivity to θ_{13} and CP violation is expected [62, 63] from this proposal. Set-ups with a neutrino beam from CERN to GranSasso or CanFranc [60], from CERN to Boulby mine [67] and from Fermilab [64] ($L \sim 300$ km) have also been proposed, and their sensitivity reach has been explored. Set-up with two sets of source ions with different boost factor for each set but with the same baseline was proposed in [66]. In [61] the authors consider the complementary situation where they take only one set of source ions, ^{8}B and ^{8}Li, with $\gamma = 350$ and two different baselines, $L = 2000$ km and 7000 km. Very high gamma beta-beam options have been studied in [48, 63, 65]. The physics potential of the low energy beta-beam option was probed in [92]. A comparison of the physics reach among different beta-beam experimental proposals can be found in [46, 56]. Here we would like to discuss the the possibility of measuring to a very high degree of accuracy the mixing angle θ_{13} and sgn(Δm^2_{31}) *aka*, the neutrino mass ordering, in an experimental set-up [48, 49, 50, 52, 53] where a pure and intense multi-GeV ν_e (using ^{8}B ion) and/or $\bar{\nu}_e$ (using ^{8}Li ion) beta-beam with the Lorentz boost γ between 250 and 650 is shot from CERN to the India-based Neutrino Observatory (INO) [25] where a large magnetized iron calorimeter (ICAL) detector is expected to come-up soon.

Even if both neutrinos and antineutrinos are used, a serious complication with all long baseline experiments involving the golden $P_{e\mu}$ channel arises from discrete degeneracies which manifest in three forms:

1. $\boxed{\textbf{the } (\theta_{13}, \delta_{CP}) \textbf{ intrinsic degeneracy [93],}}$
2. $\boxed{\textbf{the } (\mathrm{sgn}(\Delta m^2_{31}),\ \delta_{CP}) \textbf{ degeneracy [94],}}$
3. $\boxed{\textbf{the } (\theta_{23}, \pi/2 - \theta_{23}) \textbf{ degeneracy [95].}}$

This leads to an eight-fold degeneracy [96], with several spurious or “clone” solutions in addition to the true one and severely deteriorates the sensitivity of any experiment. It has been shown [96, 97] that the problem of clone solutions due the first two types of degeneracies can be evaded by choosing the baseline of the experiment equal to the characteristic refraction length due to the matter inside Earth [10, 96, 97, 98, 99]. This special value goes by the colloquial name “magic baseline” [97]. As we will discuss in detail later, at this baseline the sensitivity to the mass hierarchy and, more importantly, θ_{13}, goes up significantly [52, 97, 100], while the sensitivity to δ_{CP} is absent.

Interestingly, the CERN-INO distance of 7152 km happens to be tantalizingly close to the magic baseline ($\sim$ 7500 km). This large baseline also enhances the matter effect and requires traversal through denser regions of the Earth. Thus, for neutrinos (antineutrinos) with energies in the range 3-8 GeV sizable matter effects are induced if the mass hierarchy is normal (inverted). A unique aspect of this set-up is the possibility of observing near-resonant matter effects in the $\nu_e \rightarrow \nu_\mu$ channel. In fact, to our knowledge, what we propose here is the only experimental situation where near-resonant matter effects can be effectively used in a long baseline experiment to study the neutrino mass matrix. We show in this work that the presence of this near-maximal Earth matter effect not only maximizes the sensitivity to the neutrino mass hierarchy, it also gives the experiment an edge in the determination of the mixing angle θ_{13}. The increase in the probability $P_{e\mu}$ due to near-resonant matter effects, compensates for the fall in the beta-beam flux due to the very long baseline, so that one can achieve sensitivity to θ_{13} and mass hierarchy which is comparable, even better, than most other proposed experimental set-ups. Therefore a beta-beam experiment with its source at CERN and the detector at INO could emerge as a powerful tool for a simultaneous determination of the neutrino mass hierarchy and θ_{13}.

In [48] such an experimental set-up was considered for the first time and the physics potential explored. It was demonstrated that both the neutrino mass hierarchy as well as θ_{13} may be probed through such a set-up. The ions considered for the beta-beam in that work were the most commonly used ^{18}Ne (for ν_e) and ^{6}He (for $\bar{\nu}_e$). One requires very high values of the Lorentz boost for these ions ($\gamma \sim 10^3$) because the energy E of the beam has to be in the few GeV range for achieving near-resonant matter effects and to enable detection in the ICAL detector, which is expected to have a threshold of about 1 GeV. Such high values of γ, although possible in principle, might turn out to be very difficult to realize. Subsequently, two other ions, ^{8}B (for ν_e) and ^{8}Li (for $\bar{\nu}_e$), have been projected as viable options for the beta-beam source [72, 73]. The main advantage that these ions offer is their substantially higher end-point energy, E_0. This allows one to access $E \sim$ few GeV very easily with medium values of γ, that could be possible to achieve with either the existing CERN technology, or with the projected upgrades.

In this chapter we will mainly present our results with ^{8}B and ^{8}Li as the candidate ions for the beta-beam source at CERN and ICAL@INO as the far detector. We perform a detailed χ^2 analysis of the projected data in a future CERN-INO beta-beam experiment and show our results with γ ranging between 250 and 650. We begin in section 3.2 with a brief description of the beta-beam produced at the source. In section 3.3 we discuss the oscillation probability and highlight the importance of the magic baseline and the near-resonant matter effects in the $P_{e\mu}$ channel. Section 3.4 contains the results for the event rates expected in the ICAL detector and a discussion addressing the issue of background rejection capability of ICAL. In section 3.5 we present the details of the statistical analysis used. In section 3.6 we focus on the sensitivity to the neutrino mass hierarchy. The sensitivity of the results on the mixing angle θ_{13} are presented in section 3.7. We end in section 3.8 with our conclusions.

3.2 The Beta-beam Fluxes

Very pure and intense ν_e and/or $\bar{\nu}_e$ beams can be produced by the decay of highly accelerated radioactive beta unstable ions, circulating in a storage ring [70]. This is what is called a "beta-beam" (see section 1.3.2) and was first proposed by Piero Zucchelli [45]. The selection of the beta unstable parent ion is determined by a variety of factors essential for efficiently producing, bunching, accelerating and storing these ions in the storage ring. A beta-beam comes with the following novel features :

1. **This neutrino beam would be very suitable for precision experiments because it is pure and mono-flavor and hence beam related backgrounds are almost absent.**
2. **The neutrino spectrum depends only on the beta decay total end-point energy E_0 and the Lorentz boost of the radioactive ions γ. The spectral shape can therefore be very well determined which makes it almost free of systematic uncertainties.**
3. **The flux normalization is determined by the number of useful ion decays in the straight section of the beam.**
4. **The source is very intense.**
5. **The beam divergence is controlled by the Lorentz boost γ. Hence by increasing γ, we can produce a higher beam collimation and increase the beam intensity along the forward direction $\propto \gamma^2$.**
6. **The ν_e and $\bar{\nu}_e$ beta-beam fluxes could be produced simultaneously in distinct bunches from the storage ring. Therefore, in principle, it should be straightforward to distinguish the neutrino from the antineutrino events at any detector using the nano-second time resolution that most detectors possess and the presence of magnetic field is not mandatory.**
7. **It can be built using the existing CERN facilities.**

3.2.1 The Beta-decay Spectrum

In the rest frame of the radioactive ion the beta-decay spectrum is given by

$$\frac{d^2\Gamma^*}{d\Omega^* dE^*} = \frac{1}{4\pi\, m_e^5\, f\, \tau}(E_0 - E^*)E^*\sqrt{(E_0 - E^*)^2 - m_e^2}, \tag{3.1}$$

where m_e is the electron mass, E_0 the electron total end-point energy, E^* and τ are the neutrino energy and lifetime of the decaying ion respectively in the latter's rest frame and f is a function of m_e/E_0. In the lab frame, the flux of the unoscillated beta-beam at the detector is given by

$$\phi_{\nu_e}(E,\theta) = \frac{1}{4\pi L^2}\frac{N_\beta}{m_e^5\, f}\frac{1}{\gamma(1-\beta\cos\theta)}(E_0 - E^*)E^{*2}\sqrt{(E_0 - E^*)^2 - m_e^2}, \tag{3.2}$$

where L is the distance between the source and detector, N_β are the number of useful decays in the storage ring per unit time, θ is the angle between the neutrino flight direction and the direction in which the ions are boosted[2] and γ is the Lorentz boost such that $E^* = \gamma E(1 - \beta\cos\theta)$, E being the neutrino energy in the lab frame. The maximum energy of neutrinos produced by a beta-beam with a Lorentz factor γ is given by

$$E_{\max} = \frac{(E_0 - m_e)}{\gamma(1-\beta\cos\theta)}. \tag{3.3}$$

3.2.2 Candidate Ions for the Beta-beam

From Eq. (3.2) it is seen that the total flux and energy of the beta-beam at the far detector depends mainly on the end point energy E_0 of the beta-decay ion and the Lorentz boost factor γ. The flux increases as both E_0 and γ increase. Larger γ results in better collimation of the impinging flux, thereby increasing the statistics. The spectrum also shifts to larger energies as E_0 and γ increase. The neutrino cross section in the detector increases with energy, so for the same total flux a harder spectrum further enhances the statistics. Since the flux falls as $1/L^2$ as the source-detector distance increases, high values of either E_0 or γ or both are needed to have sizable number of events at the far detector. E_0 is an intrinsic property of the decaying ion while γ is restricted by the nature of the accelerators and the machine design. The other desired properties which the ion should have include high production yield, large decay fraction, and a lifetime that is long enough to allow the ions to be adequately accelerated. It is also easier to store larger number of lower-Z isotopes in the storage ring [101]. The characteristic features of the four different ions which have been discussed in the literature as possible candidates for the beta-beam have already been shown in Table 1.1 (section 1.3.2). While ^{18}Ne and ^{8}B are β^+ emitters (producing a ν_e beam), ^{6}He and ^{8}Li are β^- emitters (producing a $\bar{\nu}_e$ beam). They all have comparable lifetimes, conducive to the requirements necessary for the beta-beam, very high (or maximal) decay fraction and very low A/Z ratio. The point to be noted that the end-point energies, E_0, for ^{8}B and ^{8}Li are much larger than those for ^{18}Ne and ^{6}He.

---

[2] We work with the on-axis flux for which $\theta = 0$.

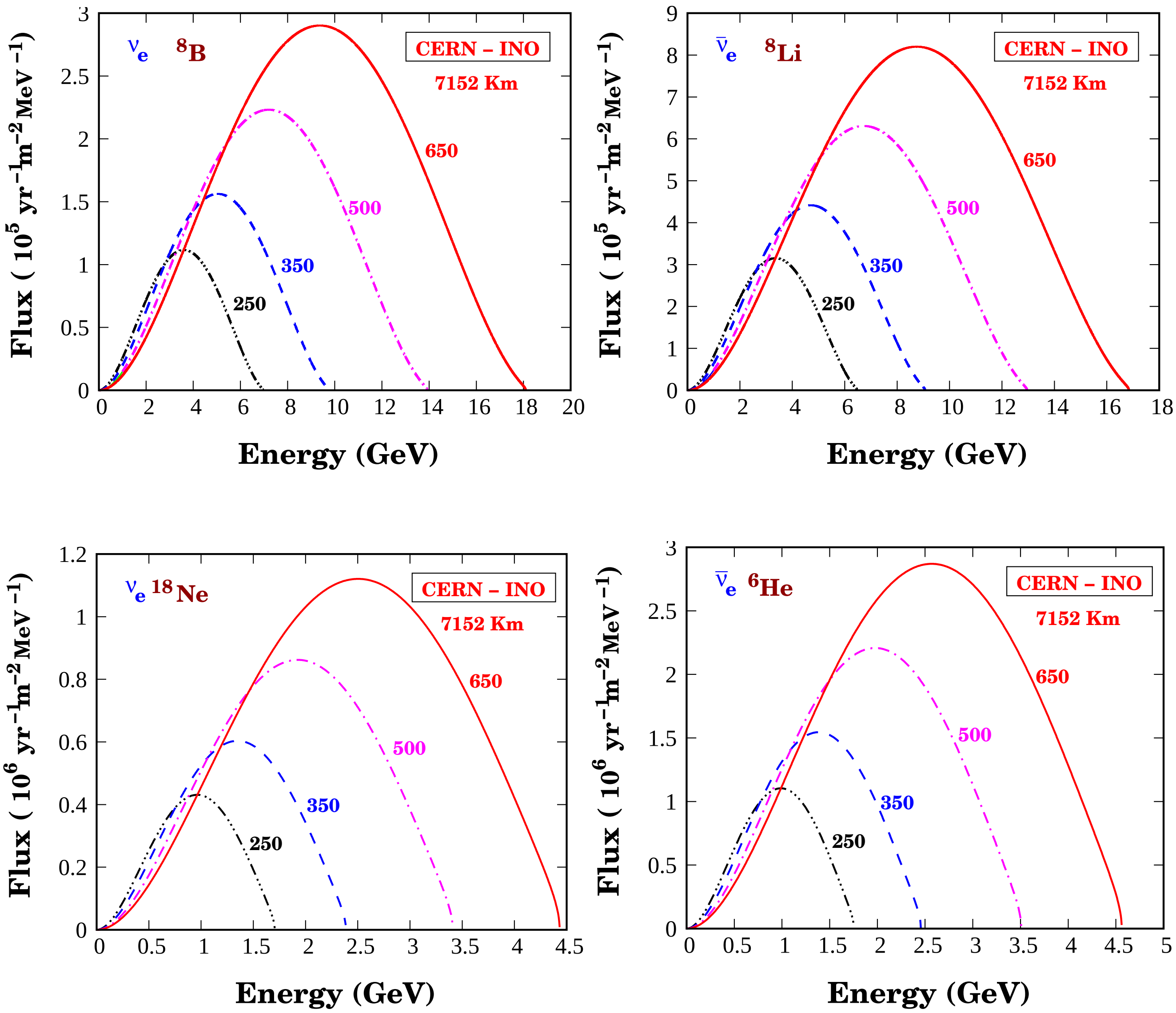

Figure 3.1: The unoscillated beta-beam flux spectrum arriving at ICAL@INO. The upper panels are for ^{8}B (left panel) and ^{8}Li (right panel), while lower panels are for ^{18}Ne (left panel) and ^{6}He (right panel).

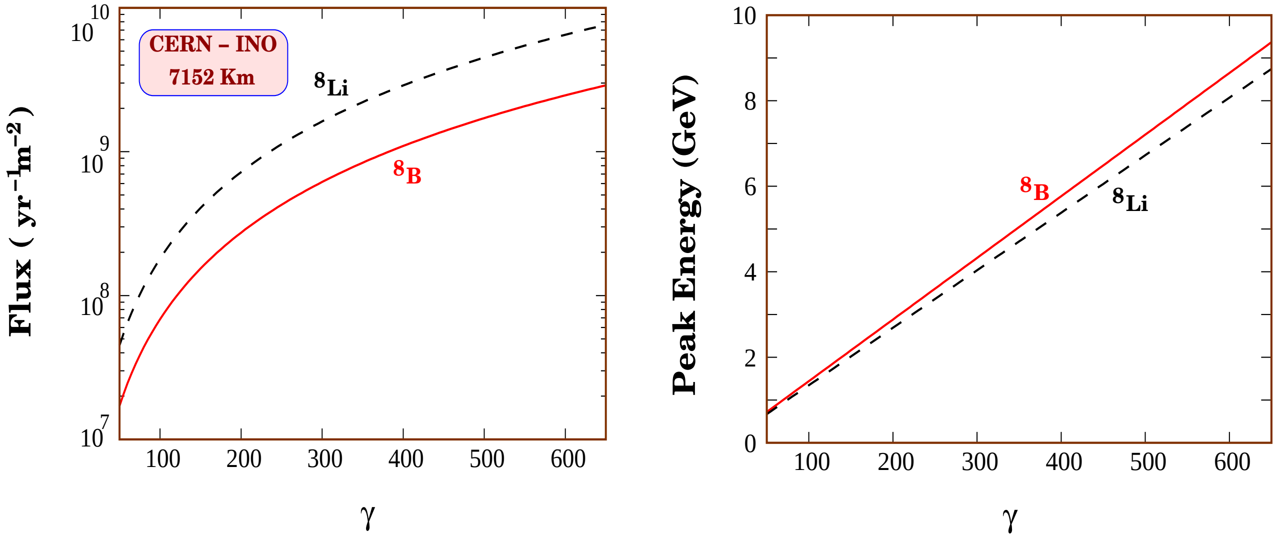

Figure 3.2: Left panel shows the total unoscillated flux in $yr^{-1}m^{-2}$ expected at INO, as a function of the Lorentz factor γ. The solid (dashed) line corresponds to ^{8}B (^{8}Li) and we have assumed 1.1×10^{18} (2.9×10^{18}) useful ions decays per year. Right panel shows the energy at which the unoscillated flux peaks, as a function of γ.

In this work we are interested in the physics potential of an experimental set-up with a beta-beam at CERN and a large magnetized iron detector in India. For such a large baseline, one needs a very high value of γ, both to cross the detector energy threshold as well as to get reasonable statistics in the detector. In particular, with ^{6}He (or ^{18}Ne) as the source ion, one needs $\gamma \gtrsim 1000$. Such high values of γ can only be achieved by using the LHC itself. As noted above, E_0 for the alternative options for the radioactive ion source (^{8}B and ^{8}Li) is higher by a factor of more than 3. This means that it should be possible to produce high intensity, high energy beams with ^{8}B and ^{8}Li for a much lower boost factor[3]. In the low γ design, the standard numbers taken for the ^{18}Ne and ^{6}He are 1.1×10^{18} (ν_e) and 2.9×10^{18} ($\bar{\nu}_e$) useful decays per year, respectively [75]. Earlier, only these ions were considered because it was believed that ^{8}B could not be produced with the standard ISOLDE techniques. Since most exercises focused on observation of CP-violation, it was necessary to have both ν_e and $\bar{\nu}_e$ beams with similar spectra, so ^{8}Li (though considered in [101]) was also generally ignored. Interest in both these ions have been rekindled recently [72, 73, 66], as it appears that having intense ^{8}B and ^{8}Li fluxes should be feasible using the ionization cooling technique [72, 73]. In what follows, we will vary the value of γ to test the physics potential of the CERN beta-beam INO-ICAL set-up and, following the current practice, assume that it is possible to get 2.9×10^{18} useful decays per year[4] for ^{8}Li and 1.1×10^{18} for ^{8}B for all values of γ. Note, however, that new ideas suggest luminosities higher even by a factor of ten or so, depending on the isotopes used, by using a recirculating ring to improve the performance of the ion source [72, 73]. Studies have shown that it is possible to accelerate ^{6}He to $\gamma \lesssim 250$ with the existing facilities at CERN, while $\gamma = 250 - 600$ should be accessible with the "Super-SPS", an upgraded version of the SPS with super-conducting magnets [60, 62, 63]. The Tevatron at FNAL could in principle also be used to produce a beta-beam with $\gamma < 600$.

---

[3] The loss in collimation is not significant as we show later.

[4] Wherever not explicitly mentioned, these reference numbers of useful ion decays for ν_e and $\bar{\nu}_e$ are chosen.

The upper panels of Fig. 3.1 depict the unoscillated ^{8}B (left-hand panel) and ^{8}Li (right-hand panel) beta-beam flux expected at ICAL@INO, for four different benchmark values of γ. The lower panels of Fig. 3.1 show the corresponding spectra for the ^{18}Ne (left-hand panel) and ^{6}He (right-hand panel) beta-beam. Note that even though apparently it might seem from the figures that the ν_e ($\bar{\nu}_e$) flux is larger for ^{18}Ne (^{6}He), in reality, for a given γ, the total flux is given by the area under the respective curves. One can easily check that for a fixed γ this is same for both the ions as expected, since we have assumed equal number of decays for both ^{18}Ne and ^{8}B for ν_e (^{6}He and ^{8}Li for $\bar{\nu}_e$)[5]. Also note that even though the total ν_e ($\bar{\nu}_e$) flux remains the same for both the ions for a given γ, we would expect that the number of events produced in the detector is much enhanced for the ^{8}B (^{8}Li) beam since the energy of the beam is larger and the CC cross sections increase with the neutrino energy. In the left panel of Fig. 3.2 we show the energy integrated total number of unoscillated neutrinos in units of $yr^{-1}m^{-2}$ arriving at ICAL@INO, as a function of the Lorentz boost γ. The solid (dashed) line corresponds to ^{8}B (^{8}Li). The figure shows that the energy integrated flux arriving at the detector increases almost quadratically with γ. Note that with the same accelerator, the Lorentz boost acquired by ^{8}B is 1.67 times larger than that by ^{8}Li, determined by the charge to mass ratios of the ions. The right panel of Fig. 3.2 depicts the energy at which the unoscillated flux peaks, as a function of the Lorentz boost γ. It turns out that this peak energy is roughly half the maximum energy of the beam, which is given as $E_{\max} \simeq 2(E_0 - m_e)\gamma$ (see Eq. 3.3).

3.3 Neutrino Propagation and the "Golden Channel"

In this section we will very briefly review some issues related to the neutrino oscillation probability.

3.3.1 The "Golden Channel" ($\nu_e \to \nu_\mu$)

The expression for $P_{e\mu}$ in matter [10, 87], up to second order terms in the small quantities θ_{13} and $\alpha \equiv \Delta m^2_{21}/\Delta m^2_{31}$, is given by[6] [88, 102]

$$\begin{aligned} P_{e\mu} &\simeq \sin^2 2\theta_{13}\, \sin^2\theta_{23} \frac{\sin^2[(1-\hat{A})\Delta]}{(1-\hat{A})^2} \\ &\pm \alpha \sin 2\theta_{13}\, \xi \sin\delta \sin(\Delta) \frac{\sin(\hat{A}\Delta)}{\hat{A}} \frac{\sin[(1-\hat{A})\Delta]}{(1-\hat{A})} \end{aligned}$$

---

[5] Of course, the on-axis flux increases with γ because of better collimation of the beam.

[6] This particular low order expansion of the transition probability is valid only in the range of L and E where the resonance condition $\hat{A} = 1$ is never reached. For the E and L range that we consider in this work, this condition is satisfied and Eq. (3.4) fails, as we discuss later in this section. Nonetheless, we present this expression to illustrate the effect of the magic baseline.

$$+ \quad \alpha \sin 2\theta_{13}\, \xi \cos\delta \cos(\Delta) \frac{\sin(\hat{A}\Delta)}{\hat{A}} \frac{\sin[(1-\hat{A})\Delta]}{(1-\hat{A})}$$

$$+ \quad \alpha^2 \cos^2\theta_{23} \sin^2 2\theta_{12} \frac{\sin^2(\hat{A}\Delta)}{\hat{A}^2}, \tag{3.4}$$

where

$$\Delta \equiv \frac{\Delta m^2_{31} L}{4E}, \tag{3.5}$$

$$\xi \equiv \cos\theta_{13}\, \sin 2\theta_{12}\, \sin 2\theta_{23}, \tag{3.6}$$

$$\hat{A} \equiv \frac{A}{\Delta m^2_{31}}. \tag{3.7}$$

Above, A is the matter potential (see Eq. 2.22). The Eq. 3.4 has been derived under the constant matter density approximation. The first term of Eq. (3.4) can be used to extract information about the value of θ_{13}. This is also the term which has the largest Earth effect and this effect of matter can be used to determine the sign of Δm^2_{31}. In Eq. (3.4) the second term has the CP violating part. This term is positive for neutrinos and negative for antineutrinos. The third term, though δ_{CP} dependent, is CP conserving. The last term is independent of both θ_{13} and δ_{CP} and depends mainly on the solar parameters Δm^2_{21} and θ_{12}. In very long baseline experiments, this term has sizable matter effects and if the true value of θ_{13} turns out to be zero (or nearly zero), this would be the only surviving term in $P_{e\mu}$ which could still be used to study matter enhanced oscillations [103]. While we will use this formula to discuss our results in some cases, our simulation is based on the exact probabilities.

3.3.2 Eight-fold Degeneracy

Despite its advantage in determining the most interesting oscillation parameters, this channel is, however, rife with the problem of "degeneracies" – the (θ_{13} - δ_{CP}) intrinsic degeneracy [93], the ($sgn(\Delta m^2_{31})$ - δ_{CP}) degeneracy [94] and the octant of θ_{23} degeneracy [95] – leading to an overall eight-fold degeneracy in the parameter values [96], of which, obviously, only one is true. These degeneracies always deteriorate the performance of an experiment.

3.3.3 Remedy with "Magic" Baseline

To tackle these problems, there are various schemes suggested in the literature which can be broadly categorized in the following fashion :

1. combine data from several experiments observing the golden channel, but with different baselines L and neutrino energies E [93, 104, 105],

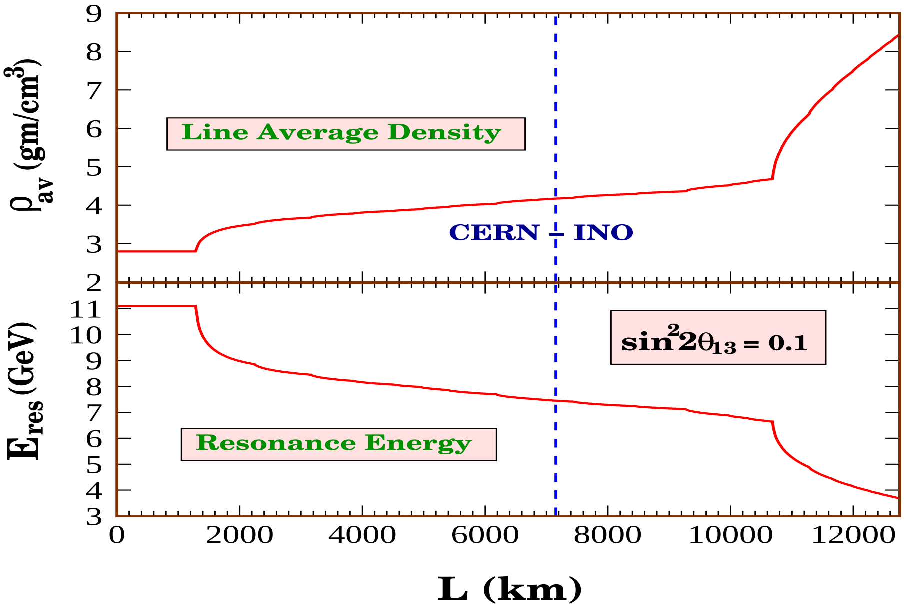

Figure 3.3: The upper panel shows the constant line average density of the Earth for various baselines calculated using the Preliminary Reference Earth Model (PREM) [110] and the lower panel depicts the corresponding resonance energy (where $\theta_{13}^m = \pi/4$) at those baselines. The blue dashed vertical line is drawn at the CERN-INO baseline.

2. combine data from accelerator experiments observing different oscillation channels [106, 107, 51],
3. combine the golden channel data with those from atmospheric neutrino experiments [108, 47],
4. combine the golden channel data with those from reactor antineutrino experiments [109],
5. kill the spurious clone solutions at the "magic baseline" [97].

Now let us see how the concept of "magic" baseline works. A particularly interesting scenario arises when the condition

$$\sin(\hat{A}\Delta) = 0 \tag{3.8}$$

is satisfied. In such an event, the last three terms in Eq. (3.4) drop out and the $P_{e\mu}$ channel enables a clean determination of θ_{13} and $sgn(\Delta m^2_{31})$.

Since $\hat{A}\Delta = AL/4E$ by definition, the first non-trivial solution of Eq. 3.8 comes in the form $\rho L = \sqrt{2}\pi/G_F Y_e$. This gives

$$\frac{\rho}{[\mathrm{gm/cm^3}]}\frac{L}{[\mathrm{km}]} \simeq 32725\ . \tag{3.9}$$

Source Location	**Detector Location**	**Distance**	**Dip Angle**
CERN	Fréjus	132 km	0.6°
	Canfranc	657 km	3.0°
	Gran Sasso	730 km	3.2°
	Boulby Mine	1050 km	4.7°
	Pyhäsalmi	2283 km	10.3°
	Canary Islands	2763 km	12.5°
	Baksan	2910 km	13.2°
	Soudan Mine	6557 km	31.0°
	Ash-River	6575 km	31.0°
	INO	**7152 km**	**34.0°**
	Homestake	7346 km	35.2°
	Henderson	7743 km	37.4°
	Super-K	8732 km	43.2°

Table 3.1: Possibilities for long baselines from CERN. In the third column, the distances (in km) from CERN to various existing/proposed underground neutrino observatories spread over the entire world are given. The respective dip angles are also mentioned in the last column. The distance of INO from CERN is 7152 km with a dip angle of 34.0°.

From the upper panel of Fig. 3.3, one can immediately observe that the above condition is satisfied for the "magic baseline" [97]

$$L_{\text{magic}} \simeq 7690 \text{ km}, \tag{3.10}$$

where the constant line average density of the Earth[7] estimated from the PREM profile [110] comes out to be 4.25 gm/cm^3. An enlightening discussion on the physical meaning of the magic baseline is given in [98].

Table 3.1 depicts the distances (in km) and the corresponding dip angles (in degree) from CERN to various existing/proposed underground neutrino observatories spread over the entire world. The CERN-INO distance corresponds to $L = 7152$ km, which is tantalizingly close to the magic baseline. We therefore expect that the beta-beam experiment we consider here should give an essentially degeneracy-free measurement of both θ_{13} and $sgn(\Delta m^2_{31})$.

3.3.4 Near-Resonant Matter Effects

The large CERN-INO baseline, of course, results in very significant Earth matter effects in the $P_{e\mu}$ channel. In fact one can readily see from the upper panel of Fig. 3.3 that for the baseline of 7152 km, the line average Earth matter density calculated using the PREM profile is $\rho_{av} = 4.17$

---

[7] We use the full PREM profile in our simulation without any approximations.

Benchmark Values	1σ estimated error
$\lvert\Delta m^2_{31}(\text{true})\rvert = 2.5 \times 10^{-3}$ eV^2	$\sigma(\lvert\Delta m^2_{31}\rvert) = 1.5\%$
$\sin^2 2\theta_{23}(\text{true})\rvert = 1.0$	$\sigma(\sin^2 2\theta_{23}) = 1\%$
$\Delta m^2_{21}(\text{true}) = 8.0 \times 10^{-5}$ eV^2	$\sigma(\Delta m^2_{21}) = 2\%$
$\sin^2 \theta_{12}(\text{true}) = 0.31$	$\sigma(\sin^2 \theta_{12}) = 6\%$
$\rho(\text{true}) = 1$ (PREM)	$\sigma(\rho) = 5\%$

Table 3.2: Chosen benchmark values of oscillation parameters and their 1σ estimated errors. The last row gives the corresponding values for the Earth matter density.

gm/cm^3, for which the resonance occurs at (see the lower panel of Fig. 3.3)

$$E_{res} \equiv \frac{|\Delta m^2_{31}| \cos 2\theta_{13}}{2\sqrt{2} G_F N_e} \tag{3.11}$$

$$= 7.45 \text{ GeV} , \tag{3.12}$$

for $|\Delta m^2_{31}| = 2.5 \times 10^{-3}$ eV^2 and $\sin^2 2\theta_{13} = 0.1$. One can check (cf. Fig. 3.1) that this is roughly in the ballpark where we expect good enough beta-beam flux using ^{8}B and ^{8}Li ions with the γ in the range 350-650. The resonance energy is $\propto \cos 2\theta_{13}$ and therefore it depends on θ_{13} mildly. At the CERN-INO baseline, the resonance energy can vary within a very small range of 7.1 to 7.85 GeV depending on the present allowed span of θ_{13}.

3.3.5 The Benchmark Oscillation Parameters

Note that the low order expansion of the probability $P_{e\mu}$ given by Eq. (3.4) is valid only for values of E and Earth matter density ρ (and hence L) where flavour oscillations are far from resonance, *i.e.*, $\hat{A} \ll 1$. In the limit $\hat{A} \sim 1$, one can check that even though the analytic expression for $P_{e\mu}$ given by Eq. (3.4) remains finite, the resultant probability obtained is incorrect [111]. We reiterate that Eq. (3.4) was presented only in order to elucidate the importance of the magic baseline. For all the numerical results presented in this thesis, we calculate the exact three generation oscillation probability using the full realistic PREM [110] profile for the Earth matter density. Unless stated otherwise, we have generated our simulated data for the benchmark values in the first column of Table 3.2. These values have been chosen in conformity with the status of the oscillation parameters in the light of the current neutrino data [78]. The values of $\sin^2 2\theta_{13}(\text{true})$, $\delta_{CP}(\text{true})$ and mass hierarchy which are allowed to vary in our study, will be mentioned wherever applicable. When we fit this simulated data, we marginalize over all the oscillation parameters, the Earth matter density, as well as the neutrino mass ordering, as applicable. We expect to have a better knowledge of all the parameters mentioned in Table 3.2 when the Beta-beam facility comes up. In particular, we assume that the 1σ error on them will be reduced to the values shown in the second column of Table 3.2 [90, 112, 113]. Therefore, we impose "priors" on these quantities, with the corresponding 1σ error.

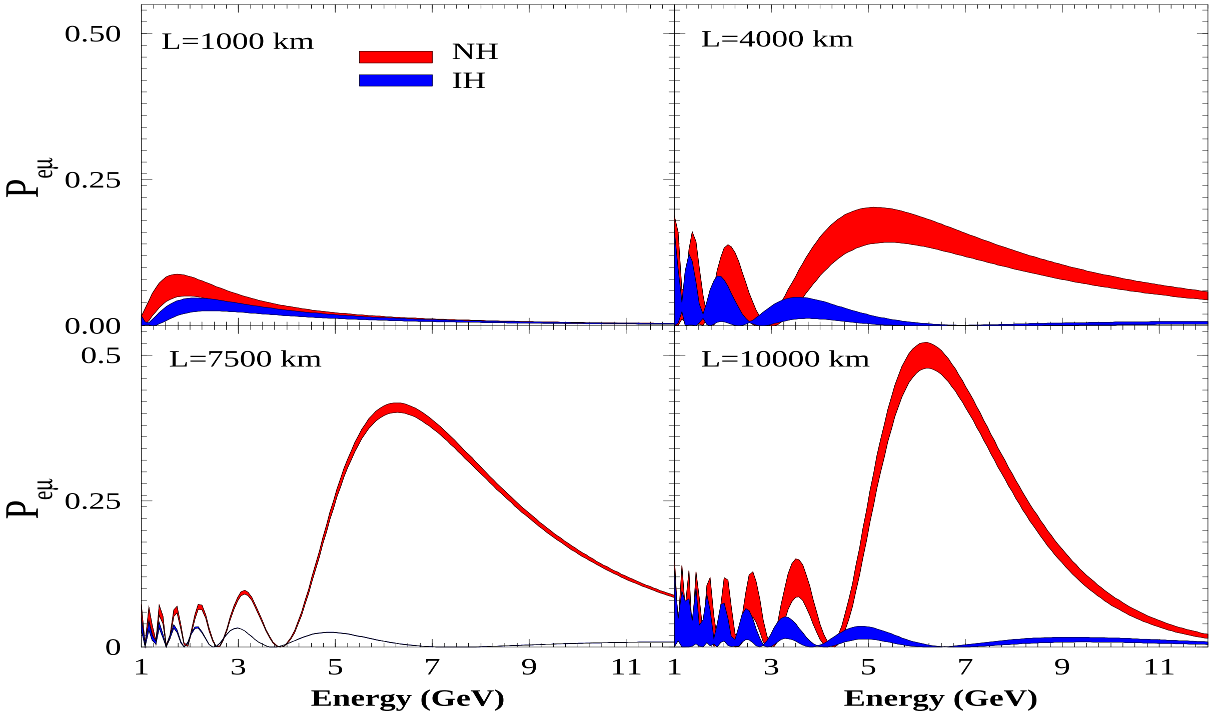

Figure 3.4: The transition probability $P_{e\mu}$ as a function of E for four values of the baseline L. The band reflects the effect of the unknown δ_{CP}. The dark (red) shaded band is for the NH while the light (cyan) shaded band is for the IH. We have taken $\sin^2 2\theta_{13} = 0.1$ and for all other oscillation parameters we assume the benchmark values given in Table 3.2.

In the fit, we allow for a 5% uncertainty in the PREM profile and take it into account by inserting a prior and marginalizing over the density normalization. We analyze the full spectral data from both the neutrino (^{8}B) and antineutrino (^{8}Li) run expected in the CERN-INO beta-beam set-up.

3.3.6 Phenomenology with $P_{e\mu}$

The exact neutrino transition probability using the full PREM density profile is given in Fig. 3.4 as a function of the neutrino energy, for four different baselines (four panels). We allow δ_{CP} to take on all possible values between 0-360 degrees and the resultant probability is shown as a band, with the thickness of the band reflecting the effect of δ_{CP} on $P_{e\mu}$. The figure is drawn assuming the benchmark values of the oscillation parameters given in Table 3.2 and $\sin^2 2\theta_{13} = 0.1$. We show the probability for both the NH (dark band) as well as the IH (light band). As discussed in detail above, for $L = 7500$ km, which is close to the magic baseline, the effect of the CP phase is seen to be almost negligible, while for all other cases the impact of δ_{CP} on $P_{e\mu}$ is seen to be appreciable. In fact, for $L = 1000$ km, the probability corresponding to the NH and IH become almost indistinguishable due to the uncertainty arising from the unknown

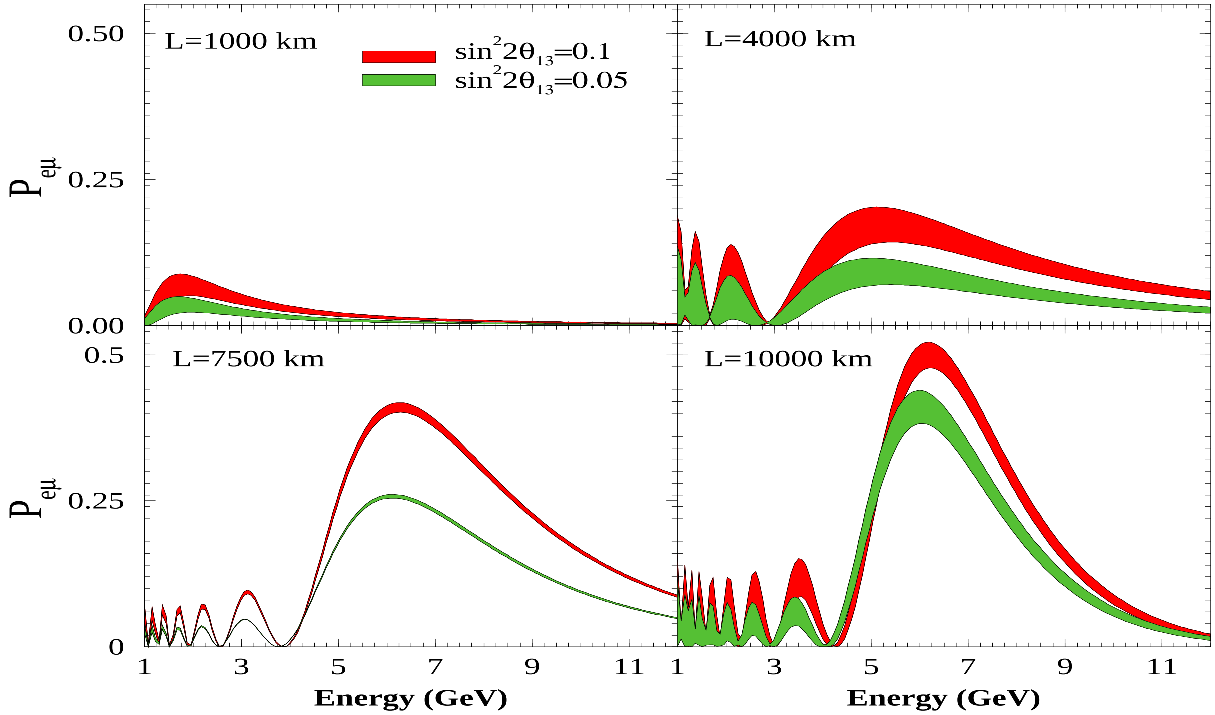

Figure 3.5: The dark (red) shaded band is the same as in Fig. 3.4. The light (green) shaded band shows the corresponding $P_{e\mu}$ for $\sin^2 2\theta_{13} = 0.05$. Values of all the other oscillation parameters are same as in Fig. 3.4 and the hierarchy is assumed to be normal.

value of δ_{CP}. As the baseline is increased, Earth matter density increases, enhancing the impact of matter effects. The probability for NH is hugely enhanced for the neutrinos, while for the IH matter effects do not bring any significant change. This difference in the predicted probability, evident in the panels corresponding to $L = 4000$, 7500 and 10000 km of Fig. 3.4, can be used to determine the neutrino mass ordering.

In Fig. 3.5 we display the dependence of the neutrino probability $P_{e\mu}$ on the mixing angle θ_{13} for four different baselines. The dark bands, as in Fig. 3.4, are for NH and $\sin^2 2\theta_{13} = 0.1$ with full variation of δ_{CP}, while the light bands are for NH and $\sin^2 2\theta_{13} = 0.05$. The impact of matter effect in increasing the θ_{13} sensitivity of a given experimental set-up is evident from the figure. The θ_{13} sensitivity for $L = 1000$ km can be seen to be much weaker than for the other cases, since matter effects are smaller. However, the most striking feature seen in Fig. 3.5 is the effect of the magic baseline in enhancing the sensitivity of the experiment to θ_{13}. The figure clearly shows that the difference in the predicted $P_{e\mu}$ for the two values of $\sin^2 2\theta_{13}$ is largest for $L = 7500$ km (since effect of δ_{CP} is the least) and thus an experiment at this baseline is most suitable for probing θ_{13}. Figs. 3.4 and 3.5 therefore reinforce our choice of the near-magic baseline as one of the best options for determining the neutrino mass hierarchy and θ_{13}, since both these parameters are directly related to large matter effects and the uncertainty of δ_{CP} could prove to be a hindrance in their measurement at non-magic baselines.

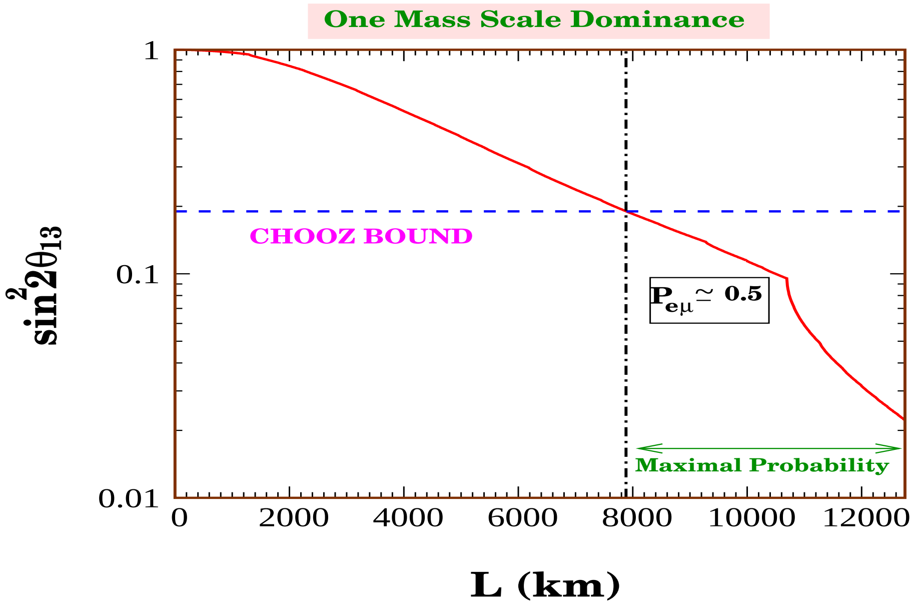

Figure 3.6: The values of $\sin^2 2\theta_{13}$ needed for the maximal matter effect (from Eq. 3.18 with p = 0) at different baselines using the constant line average density of the Earth. The blue dashed horizontal line shows the present upper bound on $\sin^2 2\theta_{13}$ which predicts that the maximal probability (= 0.5) can only be achieved for $L \geq 7880$ km (see the black dot-dashed vertical line).

3.3.7 One Mass Scale Dominance

Now let us discuss the "Golden" channel oscillation probability in the approximation where the solar mass squared difference Δm^2_{21} can be neglected. This is known as one mass scale dominance (OMSD) approximation. Under this condition with the constant matter density approximation, the probability $P_{e\mu}$ can be expressed as

$$P_{e\mu} = \sin^2\theta_{23}\sin^2 2\theta^m_{13}\sin^2\left[1.27(\Delta m^2_{31})^m L/E\right], \tag{3.13}$$

where $\sin^2 2\theta^m_{13}$ and $(\Delta m^2_{31})^m$ are given by Eq. 2.25. The probability $P_{e\mu}$ would be largest (= 0.5, assuming $\theta_{23} = \pi/4$) if the conditions

$$\sin^2 2\theta^m_{13} = 1 \tag{3.14}$$

and

$$\sin^2\left[1.27(\Delta m^2_{31})^m L/E\right] = 1 \tag{3.15}$$

are satisfied simultaneously. The first condition is achieved at the resonance energy. The second condition gives the energy where the $(\Delta m^2_{31})^m$ driven oscillatory term is maximal,

$$E^m_{max} = \frac{1.27(\Delta m^2_{31})^m L}{(2p+1)\pi/2},\ p = 0, 1, 2.. \tag{3.16}$$

Maximum matter effect is obtained when [114, 115, 116]

$$E_{res} = E^m_{max}, \tag{3.17}$$

which gives (using Eqs. 2.25 & 3.11),

$$(\rho L)^{max} = \frac{(2p+1)\pi \times 5.18 \times 10^3}{\tan 2\theta_{13}} \text{ km gm/cm}^3. \tag{3.18}$$

Although both E_{res} and E^m_{max} depend on the value of Δm^2_{31}, the distance at which we get the maximum matter effect is independent of Δm^2_{31}. However, it is controlled by θ_{13} very sensitively. In Fig. 3.6, we have plotted the values of $\sin^2 2\theta_{13}$ required for the maximal matter effect at different baselines using the constant line average density of the Earth as predicted by the PREM profile. For $p = 0$, we can have maximal matter effect only if $L \geq 7880$ km because of the upper bound of 0.19 on $\sin^2 2\theta_{13}$ [31, 78]. At $L = 7152$ km, for maximal matter effect $\sin^2 2\theta_{13} \simeq 0.23$, which is already ruled out by the present constraint. Therefore at the CERN-INO baseline, maximal matter effect cannot be achieved and the oscillation probability peaks roughly at 6 GeV (see the Figs. 3.4 & 3.5) instead of 7.45 GeV

3.4 Event Rates in ICAL@INO

3.4.1 The ICAL Detector at INO

The proposed large magnetized iron calorimeter at the India-based Neutrino Observatory [25] is planned to have a total mass of 50 kton at startup, which might be later upgraded to 100 kton. The left panel of Fig. 3.7 shows the location of the INO facility which is expected to come up at PUSHEP (lat. North 11.5°, long. East 76.6°), situated close to Bangalore in southern India. The distances and the corresponding dip angles from INO to various existing accelerator based laboratories are given in Table 3.3. The JAERI (Japan Atomic Energy Research Institute) to INO distance is 6477 km with a dip angle of 30.5°. The distances from INO to CERN and RAL (Rutherford Appleton Laboratory) are 7152, and 7653 km, respectively. These baselines are quite close to the magic baseline. In this sense, the location of INO is ideal for futuristic long baseline experiments. The BNL (Brookhaven National Laboratory) and the FNAL are the two major accelerator based facilities in US and they constitute the baselines of 11081, and 11306 km, respectively from INO with the dip angles > 60°. The first phase of this detector (starting around 2012) will focus on atmospheric neutrino measurements. The ICAL detector will have a modular structure with a total lateral size of 48m × 16m, divided into three modules of 16m × 16m each (see the right panel of Fig. 3.7). Each of these modules will have 140 horizontal layers of ∼ 6 cm thick iron plates, separated from each other by a gap of ∼ 2.5 cm to hold the active detector material, giving a total height of 12 m for the full detector. The active detector elements will be 2 cm thick glass resistive plate chambers (RPC) and will be filled with a suitable gas mixture, which will be recycled with approximately one volume change per day. An external magnetic field of ∼ 1.3 Tesla would be applied over the entire

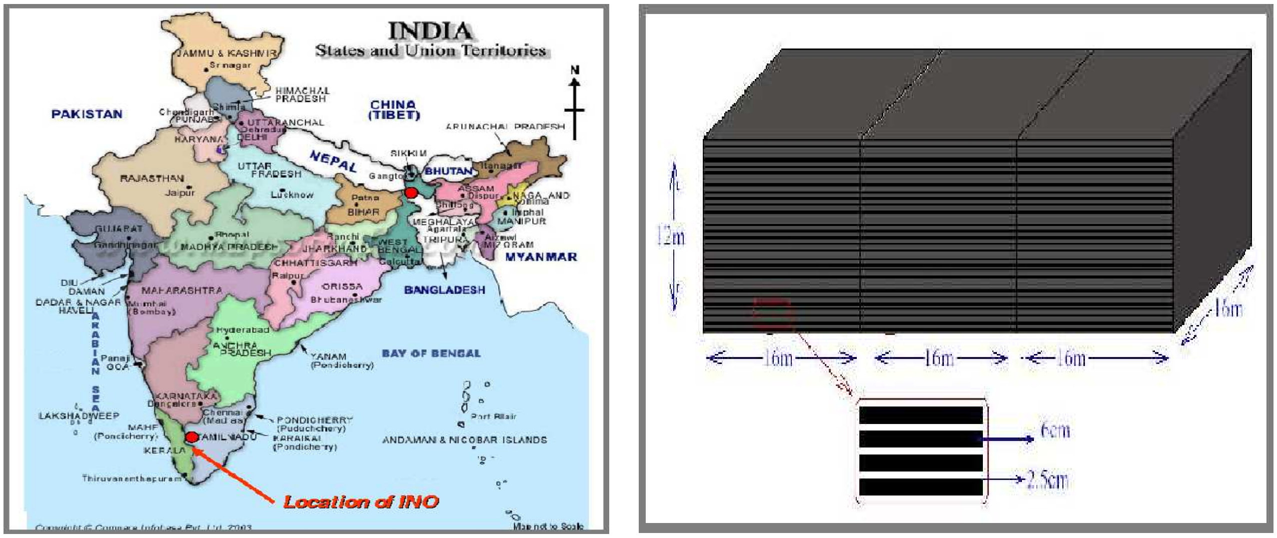
INDIA
States and Union Territories
N
PAKISTAN
CHINA (TIBET)
NEPAL
BHUTAN
MYANMAR
BANGLADESH
BAY OF BENGAL
ARABIAN SEA
JAMMU & KASHMIR
HIMACHAL PRADESH
PUNJAB
HARYANA
DELHI
UTTARANCHAL
RAJASTHAN
UTTAR PRADESH
BIHAR
SIKKIM
ARUNACHAL PRADESH
ASSAM
NAGALAND
MANIPUR
MEGHALAYA
TRIPURA
MIZORAM
GUJARAT
MADHYA PRADESH
JHARKHAND
WEST BENGAL
CHHATTISGARH
ORISSA
MAHARASHTRA
ANDHRA PRADESH
GOA
KARNATAKA
TAMIL NADU
KERALA
LAKSHADWEEP
PONDICHERRY
ANDAMAN & NICOBAR ISLANDS
Location of INO
12m
16m
16m
16m
16m
6cm
2.5cm

Figure 3.7: Left panel shows the location of the India-based Neutrino Observatory. The schematic view of the 50 kton iron calorimeter detector consisting of three modules each having 140 layers of iron plates is given in the right panel. These figures are obtained from the official website of INO (http://www.imsc.res.in/∼ino/).

Detector Location	**Source Location**	**Distance**	**Dip Angle**
INO	JAERI	6477 km	30.5°
	CERN	7152 km	34.0°
	RAL	7653 km	36.8°
	BNL	11081 km	60.3°
	FNAL	11306 km	62.4°

Table 3.3: The distances from INO to various accelerator based laboratories spread over the entire world. The corresponding dip angles are also noted.

detector. The detector will be surrounded by an external layer of scintillator or proportional gas counters which will act both as veto to identify external muon backgrounds as well as to identify partially contained events.

We are interested in measuring the golden channel probability $P_{e\mu}$. Since we have a ν_e ($\bar{\nu}_e$) flux in the beam, we need a detector which is sensitive to muons (antimuons). The detector should have a suitable energy threshold, depending on the energy spectrum of the beta-beam. In addition, it should have a good energy resolution and low backgrounds. According to the ongoing detector simulation study performed by the INO collaboration, the detector energy threshold for $\mu^{\pm}$ is expected to be around ~ 1 GeV and charge identification efficiency[8] will

---

[8] In case of a beta-beam, the neutrino and antineutrino events produced in distinct bunches can be distinguished from each other using the nano-second time resolution of the detector. The charge identification efficiency is incorporated since that helps in reducing the neutral current backgrounds.

Total Mass	50 kton
Energy threshold	1 GeV
Detection Efficiency (ϵ)	80%
Charge Identification Efficiency (f_{ID})	95%
Energy Resolution (σ) (GeV)	0.15E(GeV)
Bin Size	1 GeV
Background Rejection	0.0001
Signal error	2.5%
Background error	5%

Table 3.4: Detector characteristics of ICAL@INO used in the simulations. The bin size is kept fixed, while the number of bins is varied according to the maximum energy.

be about 95%. The detection efficiency of ICAL after cuts is expected to be about 80%. In what follows, we will present our numerical results assuming an energy threshold of 1 GeV, detector charge identification efficiency as 95% and detection efficiency as 80% for $\mu^\pm$ (cf. Table 3.4). However, we will also show the impact of changing the threshold. We have seen that our results remain unaffected if the energy threshold is raised to 2 GeV for the entire range of assumed Lorentz boost factor $\gamma = 250 - 650$. For $\gamma > 350$ the threshold can be even 3 GeV, while for $\gamma > 500$ one can work with an energy threshold of 4 GeV, without changing the final results. This can be seen from Fig. 3.1; for $\gamma = 350(500)$, the majority of neutrinos arriving at INO-ICAL would have $E > 3(4)$ GeV. The energy resolution of the detector is expected to be reasonable and we assume that the neutrino energy will be reconstructed with an uncertainty parameterized by a Gaussian energy resolution function with a HWHM $\sigma_E = 0.15E$, where E is the energy of the neutrino. We will present and compare the sensitivity of this experimental set-up with and without the full spectral analysis using both the neutrino (^{8}B) and antineutrino (^{8}Li) run.

3.4.2 Oscillation Signal at ICAL@INO

The ν_μ induced μ^- event spectrum at INO is estimated using

$$N_i = T\, n_n\, f_{ID}\, \epsilon \int_0^{E_{\max}} dE \int_{E_{A_i}^{\min}}^{E_{A_i}^{\max}} dE_A\, \phi_{\nu_e}(E)\, \sigma_{\nu_\mu}(E)\, R(E, E_A)\, P_{e\mu}(E)\,, \tag{3.19}$$

where T is the total running time (taken as five years), $\phi_{\nu_e}(E)$ (given by Eq. 3.2) is the unoscillated beta-beam flux at the detector, ϵ is the detector efficiency, n_n are the number of target nucleons in the detector, f_{ID} is the charge identification efficiency and $R(E, E_A)$ is the energy resolution function of the detector, for which we assume a Gaussian function. The quantities E and E_A are the true and reconstructed neutrino energy respectively. $E^{\max}$ is the maximum energy of the neutrinos for a given Lorentz factor γ (given by Eq. (3.3)) and $P_{e\mu}$ is the $\nu_e \rightarrow \nu_\mu$ oscillation probability. For muon events, σ_{ν_μ} is the neutrino interaction cross-

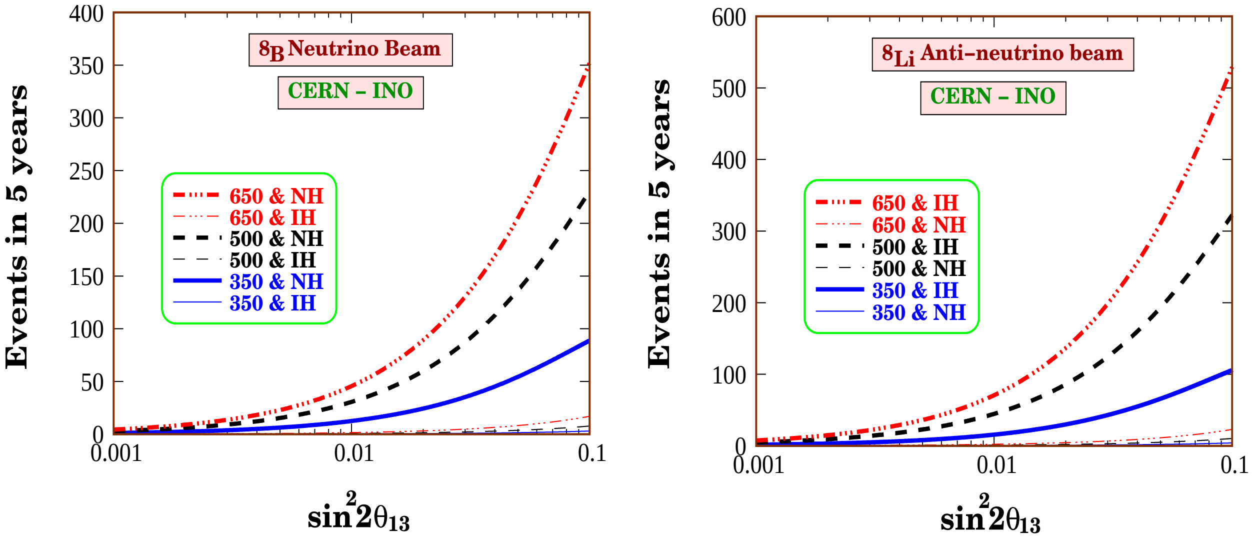

Figure 3.8: The expected number of events in 5 years running time, as a function of $\sin^2 2\theta_{13}$. The value of γ and the hierarchy chosen corresponding to each curve is shown in the figure legend.

section. The expression for the μ^+ signal in the detector from a $\bar{\nu}_e$ beta-beam flux is given by replacing ϕ_{ν_e} by $\phi_{\bar{\nu}_e}$, σ_{ν_μ} by $\sigma_{\bar{\nu}_\mu}$ and $P_{e\mu}$ by $P_{\bar{e}\bar{\mu}}$. For the neutrino-nucleon interaction we consider quasi-elastic scattering, single-pion production and deep inelastic scattering and use the cross sections given in the Globes package [117] which are taken from [118, 119].

1. $\boxed{\textbf{Event Rates vs. } \sin^2 2\theta_{13}}$

   Fig. 3.8 portrays the number of events expected in INO-ICAL from 5 years exposure of an ^{8}B (for ν_e, shown in the left-hand panel) or ^{8}Li (for $\bar{\nu}_e$, shown in the right-hand panel) beta-beam from CERN. The expected number of events is presented as a function of $\sin^2 2\theta_{13}$ for both NH and IH for three benchmark values of the boost factor γ. Large resonant matter effects in the neutrino channel for NH drives the number of expected events to very large values, compared to what would be expected for IH. Similarly, in the antineutrino channel we have resonant matter effects for IH and the number of predicted events is many times larger than for NH[9]. This difference in the number of events is seen to increase with $\sin^2 2\theta_{13}$.

   From the left-hand panel of Fig. 3.8 it can be noted that for $\gamma = 500$ and $\sin^2 2\theta_{13} = 0.05$, the predicted number of neutrino events for NH is 137, while that for IH is only 4. This implies that if the NH was true, we could comprehensively rule out the wrong IH using the neutrino run. If IH is true then antineutrino run will be very useful (see the right panel of Fig. 3.8) to rule out the wrong NH. Note that while the interaction cross section for the $\bar{\nu}_e$s are smaller, the flux itself is larger owing to the (assumed) larger number of

---

[9] In fact, matter effects are seen to suppress the oscillation probability for neutrinos (antineutrinos) compared to that in vacuum when the hierarchy is inverted (normal).

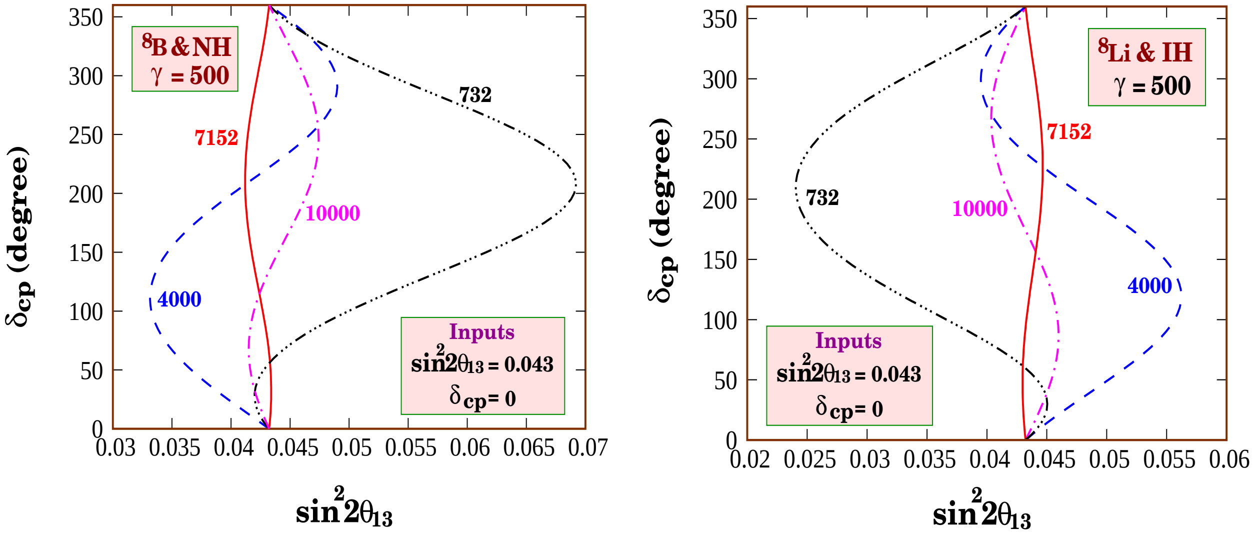

Figure 3.9: The iso-event curves in the δ_{CP}-$\sin^2 2\theta_{13}$ plane for four baselines are shown in the figure. The true values of δ_{CP} and $\sin^2 2\theta_{13}$ are assumed to be 0° and 0.043 respectively. Left- (right-) hand panel is for the ν_e ($\bar{\nu}_e$) beta-beam. The assumed hierarchy is mentioned in the figure.

decays per year for ^{8}Li. Thus the statistics expected in both the neutrino as well as the antineutrino channel is comparable. As discussed above, resonant matter effects in the neutrino (antineutrino) channel for the normal (inverted) hierarchy, results in substantial enhancement in the observed number of events. In particular, we note from Fig. 3.8 that the number of events in the near-resonant channels depends strongly on the value of $\sin^2 2\theta_{13}$, since the extent of matter effects is dictated directly by θ_{13}. We can see from the figure that the dependence of the event rate on $\sin^2 2\theta_{13}$ is much enhanced due to matter effects.

2. **Iso-event Curves in the $\sin^2 2\theta_{13}$-δ_{CP} plane**

   Fig. 3.9 shows the effect of δ_{CP} on the variation of the measured rate with the value of the mixing angle θ_{13}, for four different baselines 732 km, 4000 km, 7152 km and 10000 km. The left-hand panel shows the results for the ν_e beta-beam assuming a normal mass hierarchy, while the right-hand panel gives the same for the $\bar{\nu}_e$ beta-beam flux with IH. For all cases in any panel, a 50 kton magnetized iron calorimeter as the far detector and the same flux created at the source have been considered. Each curve gives the sets of values of $\{\sin^2 2\theta_{13}, \delta_{CP}\}$ which give the same observed rate in the detector as the set $\{\sin^2 2\theta_{13} = 0.04, \delta_{CP} = 0°\}$. In other words, if the true value of $\sin^2 2\theta_{13}$ and δ_{CP} were 0.04 and 0° respectively, then every point on a given curve would also be a solution for that experiment. It is clear from this figure that combining results from experiments at different baselines helps solve/reduce the problem. However, the most important issue exemplified here is the fact that for the baseline 7152 km, which is the CERN-INO distance, the effect of the unknown value of δ_{CP} on the measurement of θ_{13} and the mass hierarchy, is very small. This happens because this distance corresponds

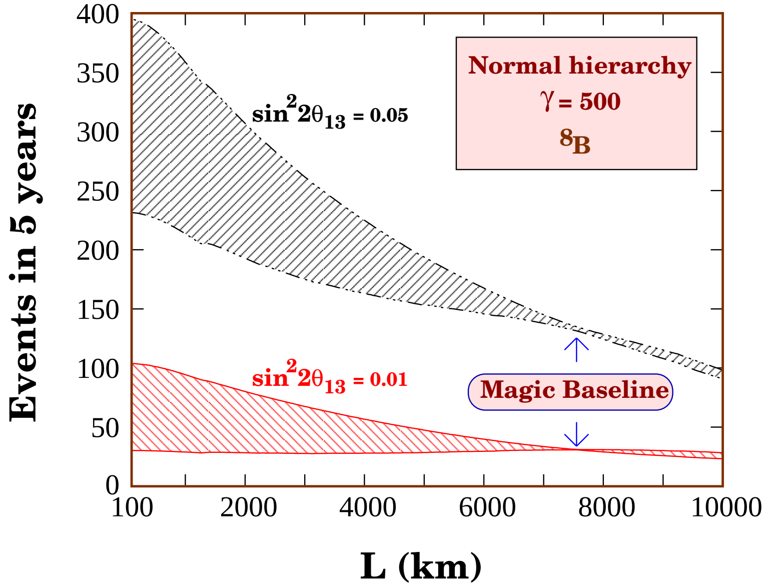

Figure 3.10: Total number of expected events in five years as a function of the baseline L for the ^{8}B source with $\gamma = 500$ and for two values of $\sin^2 2\theta_{13}$ and assuming that the NH is true. The hatched areas show the expected uncertainty due to the CP phase.

to a near-magic baseline for which, as noted earlier, the δ_{CP} dependent terms are almost vanishing.

3. **Event Rates vs. L**

   Fig. 3.10 depicts the number of events expected in five years as a function of the baseline L, if we run the experiment in the neutrino mode with $\gamma = 500$. A similar figure is expected for the antineutrino beam. The upper black hatched area shows the events for $\sin^2 2\theta_{13} = 0.05$ and the lower red hatched area corresponds to $\sin^2 2\theta_{13} = 0.01$. For each baseline L, the range covered by the hatched area shows the uncertainty in the expected value of the number of events due to the completely unknown δ_{CP}, which could take any value from 0 to 2π. The baseline L where the width of this band reduces to (almost) zero is the magic baseline. We see from the figure that the magic baseline appears at about $L \simeq 7500$ km. Note that while for $\sin^2 2\theta_{13} = 0.01$ the magic baseline is very clearly defined with the CP dependence going completely to zero, for the higher value of $\sin^2 2\theta_{13}$ of 0.05, the "magic" is not complete. The reason for this anomaly can be traced to the fact that Eq. (3.4) was derived for only very small values of θ_{13}. For larger values of this angle, higher order terms become important. These terms might depend on δ_{CP} and remain non-zero even at the magic baseline.

4. **Event Rates vs. γ**

   Figs. 3.11 and 3.12 demonstrate the impact of the magic baseline on the mass hierarchy and θ_{13} sensitivity respectively. In each of the four panels of both the figures the expected events in five years as a function of γ have been shown. Each panel is for a certain fixed

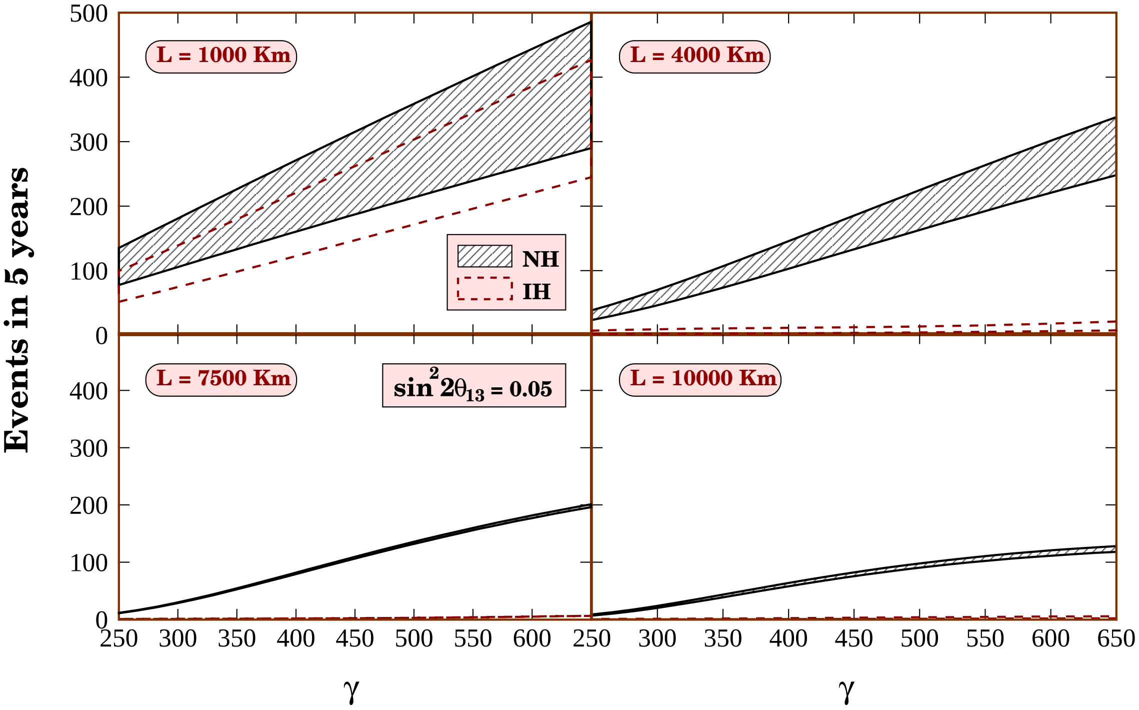

Figure 3.11: Total number of events as a function of γ for the ^{8}B source, for different values of L are shown in the four panels. The black hatched area shows the uncertainty range due to the CP phase when NH is true, while the area between the maroon dashed lines shows the corresponding uncertainty when IH is true. For all cases we assume $\sin^2 2\theta_{13} = 0.05$.

value of L, shown in the corresponding panel. In Fig. 3.11 the black hatched area shows the band for NH while the open band delimited by the dashed red lines are for the IH. As in Fig. 3.10, the band corresponds to the uncertainty in the event rate due to the unknown δ_{CP}. The effect of the uncertainty of δ_{CP} almost vanishes for $L = 7500$ km which is very close to the magic baseline. It can be seen that for the smaller baseline $L = 1000$ km, NH and IH predictions are largely overlapping, making it almost impossible for these experiments to give sensitivity to the mass hierarchy unless $\sin^2 2\theta_{13}$ turns out to be extremely large and δ_{CP} favorable. The hierarchy sensitivity is expected to improve as we go to larger baselines and this is reflected from the two bands for NH and IH separating out. It turns out that because the matter effects are very large for the magic baseline and effect of CP uncertainty is zero, this baseline gives the best sensitivity to the mass hierarchy. For L larger than magic, matter effects are higher but the flux is lower, while for L lower than magic, flux is higher but the matter effects are lower. For both above and below the magic baseline, the effect of δ_{CP} is expected to further reduce the sensitivity. This is particularly true for the lower L baselines. Fig. 3.12 shows the bands for NH but with two different choices for $\sin^2 2\theta_{13}$. Here the effect of the magic baseline is seen even more clearly.

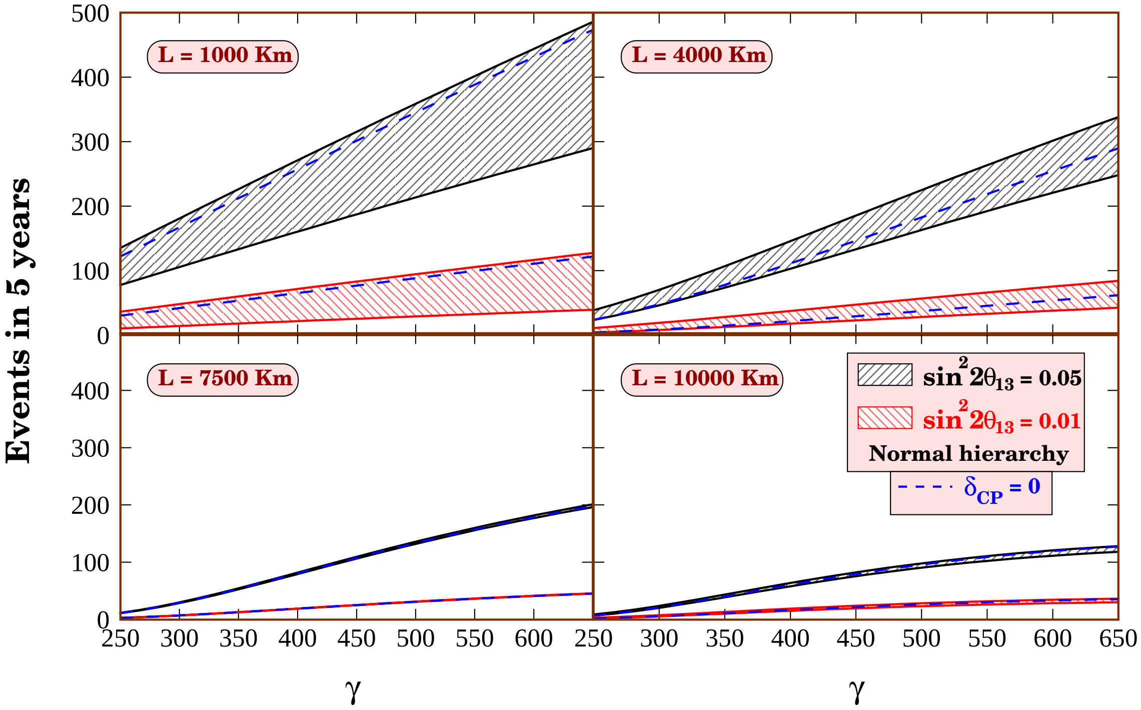

Figure 3.12: Total number of events as a function of γ for the ^{8}B source, for different values of L are shown in the four panels. The black hatched area shows the uncertainty range in the events due to CP phase when $\sin^2 2\theta_{13} = 0.05$, while the red hatched area shows the corresponding uncertainty when $\sin^2 2\theta_{13} = 0.01$. For all cases we assume NH to be true.

Fig. 3.13 shows as a function of γ, the number of events expected in five years in the CERN-INO beta-beam set-up. The solid (dashed) lines are for neutrino (antineutrino) events, with the thick line showing the event rate for NH (IH) while the thin line is for the IH (NH). We have assumed $\sin^2 2\theta_{13} = 0.01$ and $\delta_{CP} = 0$. One point which is transparent from this figure and which will be very relevant in understanding the behavior of the CERN-INO beta-beam set-up is the following: For a given value of θ_{13} and for NH (IH), we expect a large number of events in the neutrino (antineutrino) channel and almost negligible events in the antineutrino (neutrino) channel. This means that for NH (IH) it will be the neutrino (antineutrino) channel which will be statistically more important.

3.4.3 Background Rejection

Some technical issues pertaining to rejection of the beam related and atmospheric neutrino backgrounds will be discussed here.

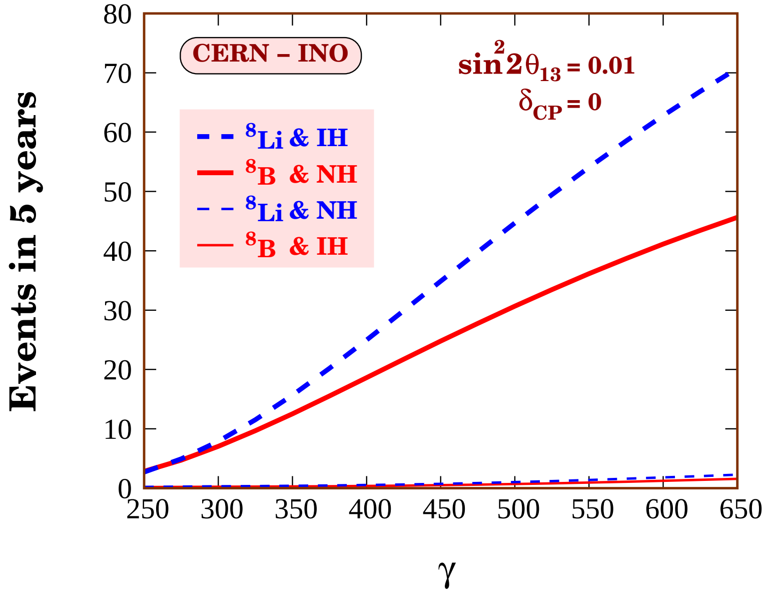

Figure 3.13: Total number of events as a function of γ for the ^{8}B (solid lines) and the ^{8}Li (dashed lines) sources. Results for both normal and inverted hierarchies are shown.

Beam Related Backgrounds

The possible backgrounds in a ν_e beta-beam experiment[10] using μ^- as an oscillation signal come from NC events such as

$$\nu_x + d(u) \rightarrow \nu_x + d(u) \tag{3.20}$$

$$\nu_x + d(u) \rightarrow \nu_x + d(u) + q\bar{q} \tag{3.21}$$

and ν_e charged current events

$$\nu_e + d \rightarrow e^- + u \text{ or } c \text{ (Cabibbo suppressed)} \tag{3.22}$$

$$\nu_e + d \rightarrow e^- + u + q\bar{q} \tag{3.23}$$

The quarks in the final state could produce mesons as a part of the hadronic junk. These mesons might constitute backgrounds in the following way :

1. Some energetic mesons can give long tracks inside the detector which can mimic the muon tracks.
2. These mesons can decay in flight producing secondary muons, a possible source of background.

---

[10] The discussion concerning the $\bar{\nu}_e$ beta-beam is similar and hence is not repeated here.

As discussed earlier, ICAL@INO will have 6 cm thick iron plates. Such a dense tracking detector will have excellent muon/pion and muon/electron separation capability in the energy range we are working with. The simulations carried out by the INO collaboration have shown that after the standard kinematical cuts are imposed, the electrons do not give any signal at all, while in 99% of the cases, the pions and kaons for the energy range of interest to us get absorbed very quickly in the iron via strong interactions and therefore do not hit enough RPCs to give a signal. At the energies of a beta-beam considered here, production cross section of D mesons (also Cabibbo suppressed) is small and they do not constitute a problem for the experiment. The associated strange or charm production is also highly suppressed at these energies. In addition, the fact that the detector will have a charge identification capability means that secondary μ^+ produced can be safely discarded, reducing the background even further. Therefore, in the analysis we estimate the NC backgrounds[11] by assuming an energy independent background suppression factor of $\sim 10^{-4}$ which agrees with [120]. We have noted that after five years of running of the CERN-INO beta-beam experiment with $\gamma = 650$, we expect only about 0.1 NC background events. Nevertheless we take this background into account in our numerical analysis. The background is assumed to have the same shape as the signal. But one should keep in mind the fact that this shape is not much of an issue since anyway the background is very small. we do not consider any backgrounds coming from the CC events of ν_e.

Since the oscillation probability $\nu_e \to \nu_\tau$ (silver channel) is about the same as that for $\nu_e \to \nu_\mu$ (golden channel), we expect almost as many ν_τ arriving at the detector as ν_μ. The τ^- produced through CC interaction may decay further inside the detector producing secondary μ^- with a branching ratio of 17.36%. But, the τ threshold (3.5 GeV) is high and the production cross section suppressed compared to μ. So we do not expect any significant background from this source either. We have estimated the number of secondary muons produced from the ν_τ component of the beam. For $\sin^2 2\theta_{13} = 0.01$, we expect 0.3 muon events per year with $\gamma = 500$. In addition, these secondary muons will be severely degraded in energy and therefore can be eliminated through energy cuts. We therefore neglect the backgrounds from this source.

Atmospheric Backgrounds

The atmospheric neutrino flux falls steeply with energy and is expected to produce much fewer events for the energy range that we are interested in[12]. The fact that INO has charge identification capability further reduces the atmospheric background. The most important handle on the reduction of this background comes from the timing information of the ion bunches inside the storage ring. For 5T magnetic field and $\gamma = 650$ for ^8B ions, the total length of the storage ring turns out to be 19564 m. We have checked that with eight bunches inside this ring at any given time, a bunch size of about 40 ns would give an atmospheric background to *signal* ratio of about 10^{-2}, even for a very low $\sin^2 2\theta_{13}$ of 10^{-3}. For a smaller bunch span, this will go down even further. In addition, atmospheric neutrinos will be measured in INO during deadtime and this can also be used to subtract them out. Hence we do not include this negligible background here.

---

[11] Mesons produced in NC processes are degraded in energy. Note that backgrounds from these mesons are very important in the case of the neutrino factory. However, since our relevant energy range is lower, the mesons produced in each event are much lower in energy and hence can be easily rejected by putting suitable cuts.

[12] We will show in the next section that even a threshold energy of 4 GeV is easily admissible in our set-up, and above 4 GeV there are much fewer atmospheric events.

3.5 Details of the Statistical Method

In order to quantify the sensitivity of this CERN-INO beta-beam experimental set-up to the mixing angle θ_{13} and $sgn(\Delta m^2_{31})$, we perform a statistical analysis of the "data" generated in ICAL@INO, assuming certain true values of the parameters. For our statistical analysis we employ a χ^2 function defined as

$$\chi^2_{total} = \chi^2_{\nu_e \to \nu_\mu} + \chi^2_{\bar{\nu}_e \to \bar{\nu}_\mu} + \chi^2_{prior} \ , \tag{3.24}$$

where the first term is the contribution from the neutrino channel, the second term comes from the antineutrino channel, while the last term comes from imposing priors on the oscillation parameters which we allow to vary freely in our fit and which we expect will be determined better from other experiments at the time when the data from the CERN-INO beta-beam set-up would be finally available. The χ^2 for the neutrino channel is given by

$$\chi^2_{\nu_e \to \nu_\mu} = min_{\xi_s, \xi_b} \left[2 \sum_{i=1}^{n} (\tilde{y}_i - x_i - x_i \ln \frac{\tilde{y}_i}{x_i}) + \xi_s^2 + \xi_b^2 \right] \ . \tag{3.25}$$

where n is the total number of bins,

$$\tilde{y}_i(\{\omega\}, \{\xi_s, \xi_b\}) = N_i^{th}(\{\omega\}) \left[1 + \pi^s \xi_s\right] + N_i^b \left[1 + \pi^b \xi_b\right] \ , \tag{3.26}$$

$N_i^{th}(\{\omega\})$ given by Eq. (3.19) being the predicted number of events in the energy bin i for a set of oscillation parameters ω and N_i^b are the number of background events in bin i. The quantities π^s and π^b in Eq. (3.26) are the systematical errors on signals and backgrounds respectively. We have taken $\pi^s = 2.5\%$ and $\pi^b = 5\%$ (see Table 3.4). The quantities ξ_s and ξ_b are the "pulls" due to the systematical error on signal and background respectively. The data in Eq. 3.25 enters through the variables $x_i = N_i^{ex} + N_i^b$, where N_i^{ex} are the number of observed signal events in the detector and N_i^b is the background, as mentioned earlier. We simulate the signal event spectrum using Eq. 3.19 for our assumed true values for the set of oscillation parameters which are given in the first column of Table 3.2. Different options are used for $\sin^2 2\theta_{13}$(true), δ_{CP}(true) and the true hierarchy and these are mentioned wherever applicable. In our χ^2 fit we marginalize over *all* oscillation parameters, the Earth matter density, as well as the neutrino mass hierarchy, as applicable. We do this by allowing all of these to vary freely in the fit and picking the smallest value for the χ^2 function. Of course, we expect better determination of some of these parameters, which are poorly constrained by this experimental set-up. Therefore, we impose a "prior" on these parameters through the χ^2_{prior} given by

$$\chi^2_{prior} \ = \ \left(\frac{|\Delta m^2_{31}| - |\Delta m^2_{31}(\text{true})|}{\sigma(|\Delta m^2_{31}|)} \right)^2 + \left(\frac{\sin^2 2\theta_{23} - \sin^2 2\theta_{23}(\text{true})}{\sigma(\sin^2 2\theta_{23})} \right)^2$$

$$
\begin{aligned}
&+ \left(\frac{\Delta m^2_{21} - \Delta m^2_{21}(\text{true})}{\sigma(\Delta m^2_{21})}\right)^2 + \left(\frac{\sin^2\theta_{12} - \sin^2\theta_{12}(\text{true})}{\sigma(\sin^2\theta_{12})}\right)^2 \\
&+ \left(\frac{\rho - 1}{\sigma(\rho)}\right)^2 . \qquad (3.27)
\end{aligned}
$$

where the 1σ error on these that we use are taken from [90, 112] and are given in the right column of Table 3.2. In our computation, we have used a matter profile inside the Earth with 24 layers. In Eq. 3.27, ρ is a constant number by which the matter density of each layer has been scaled. The external information on ρ is assumed to come from the study of the tomography of the earth [113]. In Eq. 3.27, ρ varies from 0.95 to 1.05 i.e., 5% fluctuation around 1.

Note that in our definition of the χ^2 function given by Eqs. 3.24 and 3.25, we have assumed that the neutrino and antineutrino channels are completely uncorrelated, all the energy bins for a given channel are fully correlated, and ξ_s and ξ_b are fully uncorrelated. We minimize the χ^2_{total} in two stages. First it is minimized with respect to ξ_s and ξ_b to get Eq. 3.25, and then with respect to the oscillation parameters ω to get the global best-fit. For minima with respect to ξ_s and ξ_b, we require that

$$
\frac{\partial \chi^2}{\partial \xi_s} = 0 \text{ and } \frac{\partial \chi^2}{\partial \xi_b} = 0 . \qquad (3.28)
$$

From Eqs. 3.25, 3.26, 3.28 we get,

$$
\begin{pmatrix} a_{11} & a_{12} \\ a_{21} & a_{22} \end{pmatrix} \begin{pmatrix} \xi_s \\ \xi_b \end{pmatrix} = \begin{pmatrix} c_1 \\ c_2 \end{pmatrix} \qquad (3.29)
$$

where,

$$
\begin{aligned}
c_1 &= \sum_{i=1}^{n} \left(\frac{x_i \pi^s N_i^{th}}{N_i^{th} + N_i^b} - \pi^s N_i^{th}\right) , \\
c_2 &= \sum_{i=1}^{n} \left(\frac{x_i \pi^b N_i^b}{N_i^{th} + N_i^b} - \pi^b N_i^b\right) , \\
a_{11} &= \sum_{i=1}^{n} \left[\frac{x_i (\pi^s N_i^{th})^2}{(N_i^{th} + N_i^b)^2}\right] + 1 , \\
a_{22} &= \sum_{i=1}^{n} \left[\frac{x_i (\pi^b N_i^b)^2}{(N_i^{th} + N_i^b)^2}\right] + 1 , \\
a_{12} = a_{21} &= \sum_{i=1}^{n} \left[\frac{x_i N_i^{th} N_i^b \pi^s \pi^b}{(N_i^{th} + N_i^b)^2}\right] \qquad (3.30)
\end{aligned}
$$

Using Eqs. 3.29 and 3.30, we calculate the values of ξ_s and ξ_b and then we use these values to calculate $\chi^2_{\nu_e \to \nu_\mu}$. In a similar fashion, we estimate $\chi^2_{\bar{\nu}_e \to \bar{\nu}_\mu}$ to obtain the χ^2_{total}.

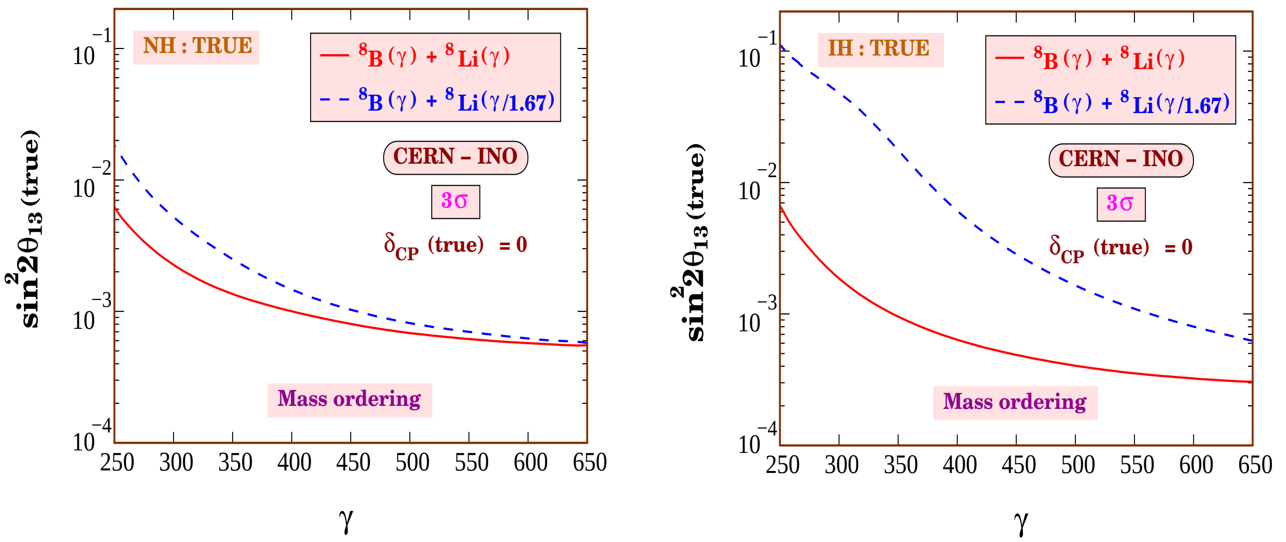

Figure 3.14: The range of $\sin^2 2\theta_{13}$(true) for which the wrong hierarchy can be ruled out at the 3σ C.L., as a function of γ. The left panel is for NH as true, while the right panel is when IH is true. The red solid curves show the sensitivity when the γ is chosen to be the same for both the neutrino and the antineutrino beams. The blue dashed lines show the corresponding sensitivity when the γ for the antineutrinos is scaled down by a factor of 1.67 with respect to the γ of the neutrino beam.

3.6 Measurement of the Neutrino Mass Ordering

Let us first focus on the issue of neutrino mass ordering. If the true value of θ_{13} has indeed been chosen to be large by Nature, sizable matter effects can be expected in this magical CERN-INO beta-beam experimental set-up, giving us a handle on the mass hierarchy. The mass hierarchy sensitivity is defined as the range of $\sin^2 2\theta_{13}$(true) for which the wrong hierarchy can be excluded at the 3σ C.L. The left (right) panel of Fig. 3.14 shows the hierarchy sensitivity when the NH (IH) is true. We show this as a function of γ. In both panels we show by the red solid lines the sensitivity when we add neutrino and antineutrino data with the same value of the Lorentz boost shown in the x-axis. The blue dashed lines on the other hand correspond to the sensitivity expected when the neutrino beam runs with the γ shown in the x-axis while the γ for the antineutrino beam is scaled down by a factor of 1.67. We assume five[13] years of running of the beta-beam in both polarities and a full spectral analysis has been performed. We note that using the combined neutrino and antineutrino beam running at the same value of γ the wrong hierarchy could be ruled out at 3σ for $\sin^2 2\theta_{13} > 6.8 \times 10^{-4}$ ($\sin^2 2\theta_{13} > 4.0 \times 10^{-4}$) for $\gamma = 500$ if the NH (IH) is true. Presence of both neutrino and antineutrino data simultaneously in the analysis restricts the fitted value of θ_{13} to be in a range very close to the assumed true value. For instance, for NH true, data corresponds to a large number of events for neutrinos and a small number of events for antineutrinos. When this is fitted with IH, we have a small number of events predicted for the neutrinos. In order to minimize the disparity between the data and

---

[13] Here all sensitivity figures correspond to a five years run.

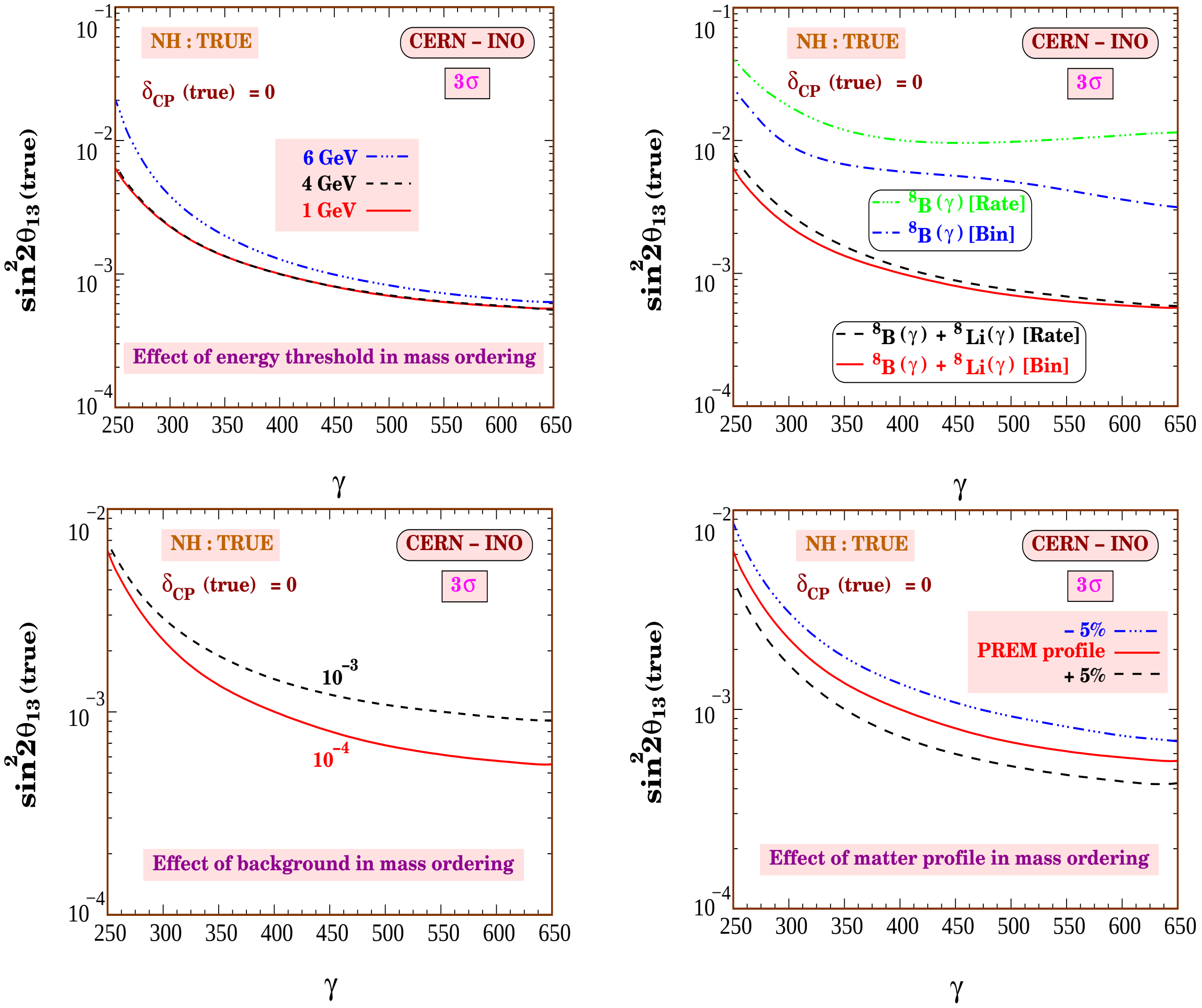

Figure 3.15: Plots showing the impact of various factors on the mass hierarchy sensitivity of the CERN-INO beta-beam experiment. The top left panel shows the impact of changing the detector threshold. The lower left panel shows the effect of changing the background rejection factor. The top right panel shows the difference in the sensitivity between the rate and spectral analysis. The lower right panel shows how the density profile would impact the hierarchy sensitivity.

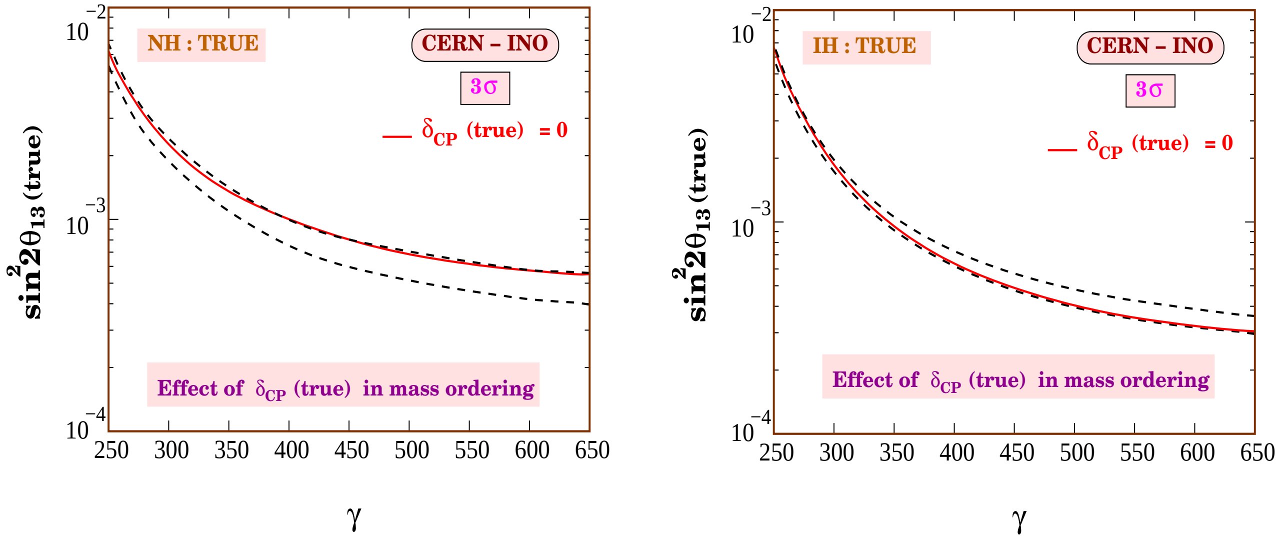

Figure 3.16: Effect of δ_{CP}(true) on the hierarchy sensitivity. The black dashed lines show the worst and best cases when we allow δ_{CP}(true) to take any value between 0 and 2π. The red solid curve corresponds to the reference case where $\delta_{CP}(\text{true}) = 0$. The left panel shows the case for true NH while the right panel is for true IH.

prediction for neutrinos, the fit tends to drive θ_{13} to its largest allowed value. However, larger values of θ_{13} would give very large number of antineutrino events for IH and this would be in clear conflict with the data. Therefore, the net advantage of adding data from both neutrino and antineutrino channels is that one cannot artificially reduce the χ^2 any longer by tinkering with θ_{13} in the fit. As a result, the sensitivity of the experiment to mass hierarchy witnesses a substantial improvement.

It can be noted from the plots that the hierarchy sensitivity falls when the scaled γ option for the antineutrino beam has been used. This is particularly relevant when the true hierarchy is inverted and/or when γ is low. Since scaling the γ reduces it by a factor of 1.67, the statistics for the antineutrinos fall by nearly a factor of 1.67 for this case and this reflects in the reduced hierarchy sensitivity of the experiment. Its impact when true hierarchy is inverted is more because in that case, the data corresponds to larger events for the antineutrinos and very small events for the neutrinos. The antineutrino events are therefore the driving force and an increase in their statistical uncertainty due to the scaled down γ accentuates the adverse effect on the hierarchy sensitivity. In the case of NH, the events in the neutrino channel are the dominant factor and the role of the antineutrinos is only to prevent the θ_{13} values in the fit to run to very large values, as discussed before. As long as the antineutrino events have enough statistical power to restrict θ_{13} to values close to the true value at which the data was generated, the hierarchy sensitivity remains reasonably good. Therefore, for the NH only for very low values of γ the hierarchy sensitivity gets seriously affected by the Lorentz boost scaling.

Fig. 3.15 shows how the hierarchy sensitivity depends on diverse input factors. As in Fig. 3.14 we show the 3σ limit for $\sin^2 2\theta_{13}$ as a function of γ in all the four panels and we assume that NH is true. The reference curve (red solid line) in all panels corresponds to the result obtained

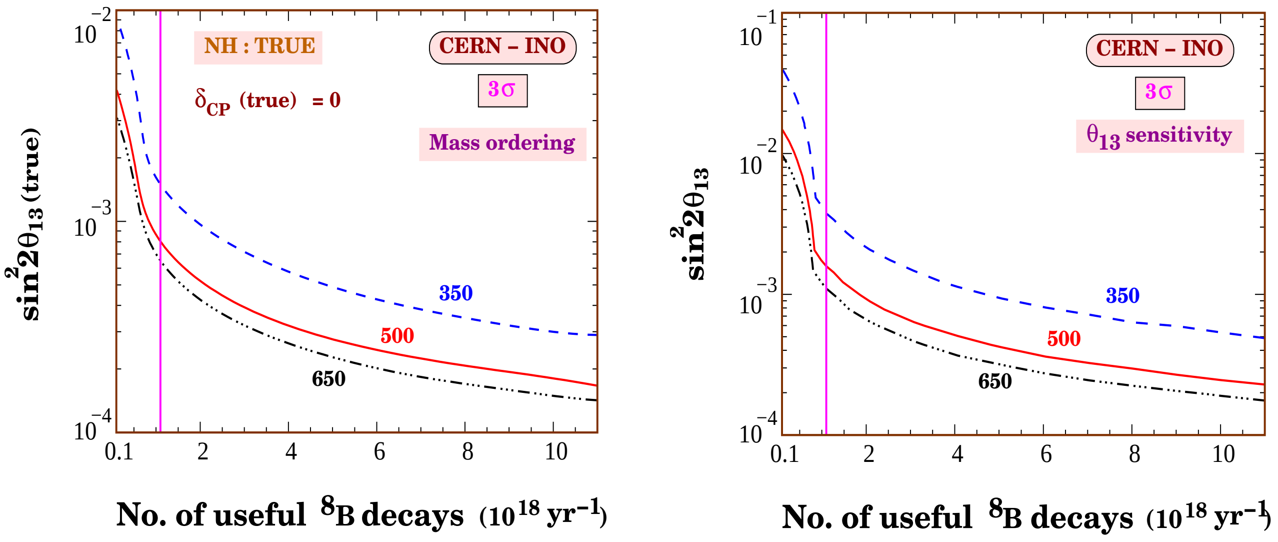

Figure 3.17: The variation of the experimental sensitivity on the number of useful ion decays in the straight sections of the storage ring. Left panel shows sensitivity to the mass hierarchy assuming NH to be true. Right panel shows the $\sin^2 2\theta_{13}$ sensitivity reach. In both panels, the majenta solid vertical line corresponds to the reference value used in the rest of the analysis.

with a ν_e and $\bar{\nu}_e$ beam with a spectral analysis. The upper left hand panel shows the effect of changing the threshold energy of the detector. The sensitivity of the experiment is seen to remain almost stable against the variation of the threshold energy upto 4 GeV. Only for a threshold of 6 GeV and above the sensitivity falls, the lower γ values getting more affected since they correspond to lower neutrino energies. In the lower left hand panel of the figure the effect of the chosen background fraction on the hierarchy sensitivity has been shown. The red solid line shows the sensitivity for our assumed background factor of 10^{-4} while the black dashed line shows the corresponding sensitivity when the background rejection is poorer and we have a higher residual background fraction of 10^{-3}. The upper right hand panel shows how our sensitivity increases by taking into account the spectral information of the events. It also shows how much improvement we get by combining the antineutrino data with the neutrino data. The black dashed line shows how the sensitivity falls when we use the total event rates instead of the events spectrum. The blue dashed-dotted and green dashed-triple-dotted lines show the sensitivity expected from the neutrino data alone. The blue dashed-dotted line is for binned neutrino data while the green dashed-triple-dotted lines shows the sensitivity for the total event rate for neutrinos alone. It can be seen that the effect of using the spectral information is only marginal when both neutrino and antineutrino are used, while the effect of combining the antineutrino data with the neutrino data on the sensitivity is huge. For the neutrino data alone, the sensitivity improves significantly when one uses the spectral information. In the lower right hand panel we show how the sensitivity of the experiment to hierarchy would get affected if we use a different profile for the Earth matter density instead of PREM. The red solid line is for earth density according to the PREM profile while the blue dotted and black dashed lines are when the matter density is 5% lower and 5% higher respectively than the density predicted by

$\gamma\backslash$N	Mass Hierarchy (3σ)		$\sin^2 2\theta_{13}$ sensitivity (3σ)	
	1.1×10^{18}	2.043×10^{18}	1.1×10^{18}	2.043×10^{18}
350	1.3×10^{-3}	9.3×10^{-4}	3.8×10^{-3}	2.3×10^{-3}
650	5.6×10^{-4}	4.1×10^{-4}	1.1×10^{-3}	7.3×10^{-4}

Table 3.5: Comparison of the variation of the detector sensitivity to mass hierarchy (columns 2 and 3) and $\sin^2 2\theta_{13}$ sensitivity (columns 4 and 5) with γ and N, the number of useful ion decays per year.

the PREM profile. When the density is higher (lower) the matter effects are higher (lower) and therefore the sensitivity improves (deteriorates).

One crucial point that we have not stressed so far concerns the dependence of the detector performance on the *true value* of δ_{CP}. All the earlier plots were presented assuming that $\delta_{CP}(\text{true}) = 0$. At exactly the magic baseline, it is expected that the sensitivity of the experiment to be completely independent of δ_{CP}. The CERN-INO distance of 7152 km is almost magical, but it is not the exact magic baseline. Therefore, we do expect some remnant impact of $\delta_{CP}(\text{true})$ on our results[14]. To show how our results get affected by $\delta_{CP}(\text{true})$, we show in Fig. 3.16 the hierarchy sensitivity just as in Fig. 3.14, but here we show the full band corresponding to all values of $\delta_{CP}(\text{true})$ from 0 to 2π. As before, the left panel is for NH true while the the right panel is for IH true, and we have taken in the analysis the full spectral data for the neutrinos as well as the antineutrinos, with the same γ. The lower edge of this band shows the best possible scenario where the experiment is most sensitive, while the upper edge shows the worst possible sensitivity. The red solid lines in both panels show for comparison the hierarchy sensitivity corresponding to $\delta_{CP}(\text{true}) = 0$, which we had presented in Fig. 3.14. We note from the figure that the hierarchy sensitivity is nearly the best for $\delta_{CP}(\text{true}) = 0$ when IH is true while if NH is true then it would give us almost the worst sensitivity. For NH (IH) as true the best possible sensitivity would be $\sin^2 2\theta_{13} > 3.96 \times 10^{-4}$ ($\sin^2 2\theta_{13} > 2.96 \times 10^{-4}$) for $\gamma = 650$ to be compared with $\sin^2 2\theta_{13} > 5.51 \times 10^{-4}$ ($\sin^2 2\theta_{13} > 3.05 \times 10^{-4}$) when $\delta_{CP}(\text{true}) = 0$. Therefore, we conclude that if NH is true then it would not be unfair to expect an even better hierarchy sensitivity than what was reported in Fig. 3.14, while if IH is true then the best sensitivity will be returned for $\delta_{CP}(\text{true}) \simeq 0$.

It has been noted from Figs. 3.11 and 3.12 that the total number of events in the detector increases roughly linearly with γ, except for extremely long baselines. Increasing the number of ion decays per year will also bring about a simple linear increase in the statistics. It is therefore pertinent to make a fair comparison between the dependence of the mass hierarchy sensitivity to the Lorentz boost γ and the number of useful ion decays in the ring[15]. In the left panel of Fig. 3.17 we show the effect of increasing the number of ion decays on the hierarchy sensitivity[16]. The plots exhibit the dependence of the sensitivity on the number of useful ion decays per year for an exposure of five years, for three different values of γ. The same Lorentz boost for the neutrino and antineutrino beams have been assumed. We present in Table 3.5 the relative increase in the hierarchy sensitivity when we increase the γ by a factor of 1.86 and compare it against the increase in the sensitivity when the number of ion decays are increased by the same factor. It can be noted that while the hierarchy sensitivity improves by a factor of 2.54 in going from $\gamma = 350$ to 650 keeping the number of ion decays per year as 1.1×10^{18}, it increases 1.5-fold when we raise the number of ion decays per year from 1.1×10^{18} to 2.04×10^{18} keeping $\gamma = 350$. However, we would like to stress that the improvement of the hierarchy sensitivity is not linear with either γ or number of ion decays per year. The crucial thing is that the behavior of the sensitivity dependence on both γ and number of ion decays per year is very similar. It increases very fast initially and then comparatively flattens out.

---

[14] Note that in all our results presented in this work, we have fully marginalized over all the oscillation parameters in the fit, including δ_{CP}.

[15] Note that this is also equivalent to increasing the total exposure time of the experiment. Both number of ion decays per year and exposure appear as a normalization factor for the event rate and hence increasing the

3.7 Measurement of $\sin^2 2\theta_{13}$

The CERN-INO beta-beam set-up is also expected to give very good sensitivity to the θ_{13} measurement. In what follows, we will quantify our results in terms of three "performance indicators",

1. $\sin^2 2\theta_{13}$ **sensitivity reach,**
2. $\sin^2 2\theta_{13}$ **discovery reach,**
3. $\sin^2 2\theta_{13}$ **precision.**

Below a detailed description of our definitions of these performance indicators has been given. All results in this section have been obtained by taking into account the full event spectrum and combining five years data from both the neutrino and antineutrino channels.

3.7.1 $\sin^2 2\theta_{13}$ Sensitivity Reach

The θ_{13} sensitivity reach is defined as the range of $\sin^2 2\theta_{13}$ which is incompatible with the data generated for $\sin^2 2\theta_{13}(\text{true}) = 0$ at the 3σ C.L. This performance indicator corresponds to the new $\sin^2 2\theta_{13}$ limit if the experiment does not see a signal for θ_{13}-driven oscillations[17].

---

number of ion decays by a factor n keeping the exposure same is equivalent to increasing the exposure by a factor n keeping the number of ion decays per year fixed.

[16] We assume that the number of useful ion decays for both ^{8}B and ^{8}Li have been scaled by the same factor. In the figure along the x-axis only the ^{8}B numbers are shown.

[17] Note from Eq. 3.4, while the first three terms go to zero when $\theta_{13} \rightarrow 0$, the last term, which depends only on the solar parameters and θ_{23}, remains non-vanishing. Therefore, when the flux is high, *i.e.*, for large γ and/or enhanced luminosity, we expect a sizable number of events even when $\sin^2 2\theta_{13}(\text{true}) = 0$.

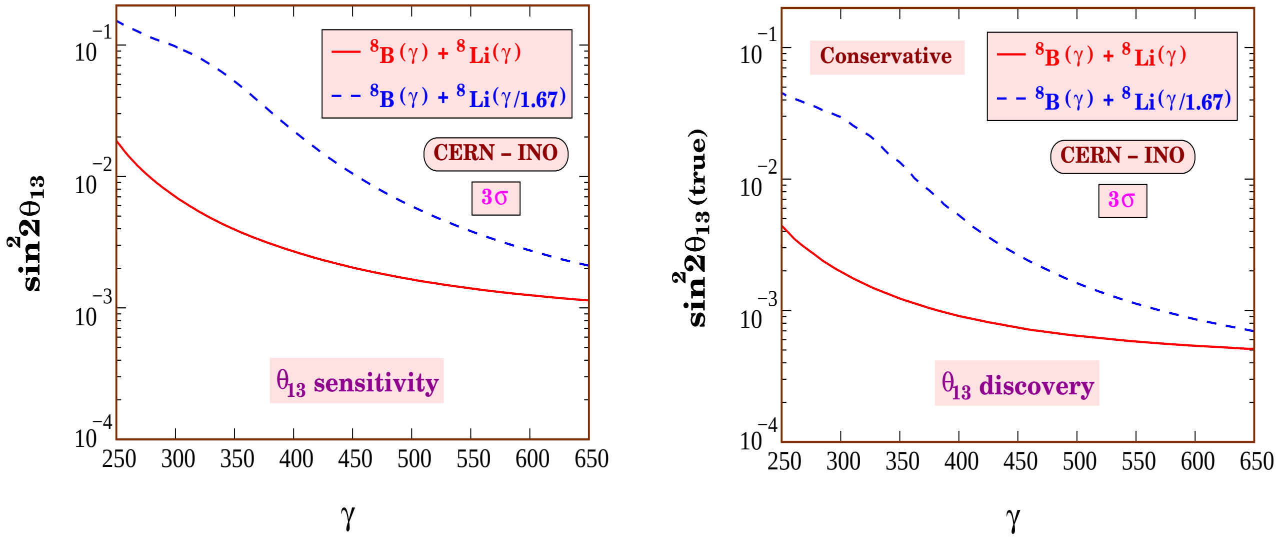

Figure 3.18: Left panel shows the 3σ sensitivity limit for $\sin^2 2\theta_{13}$. Right panel shows the 3σ discovery reach for $\sin^2 2\theta_{13}$(true). The red solid lines in the left and right panels show the sensitivity reach and discovery potential respectively, when the γ is assumed to be the same for both the neutrino and the antineutrino beams. The blue dashed lines show the corresponding limits when the γ for the ^{8}Li is scaled down by a factor of 1.67 with respect to the γ of the neutrino beam, which is plotted in the x-axis.

In that case, we can exclude some allowed values of $\sin^2 2\theta_{13}$, which we call our "θ_{13} sensitivity reach". We simulate this situation in our analysis by generating the data at $\sin^2 2\theta_{13}(\text{true}) = 0$ and fitting it with some non-zero value of $\sin^2 2\theta_{13}$ by means of the χ^2 technique. In our fit we marginalize over all the oscillation parameters including δ_{CP} and the mass hierarchy[18] and choose the value of $\sin^2 2\theta_{13}$ for which the fit yields $\chi^2 = 9$. The result is shown in the left panel of Fig. 3.18, as a function of γ. The red solid line shows the $\sin^2 2\theta_{13}$ sensitivity when γ is assumed to be the same for both the neutrino and the antineutrino beams. The blue dashed lines shows the corresponding 3σ upper limit when γ for the ^{8}Li is scaled down by a factor of 1.67 with respect to that for the neutrino beam. In generating the data we have assumed that $\sin^2 2\theta_{13}(\text{true}) = 0$, which means that we have negligible events in both the neutrino as well as the antineutrino channels, irrespective of the mass hierarchy. When this data is fitted allowing for non-zero $\sin^2 2\theta_{13}$, the neutrino (antineutrino) channel plays a dominating role when NH (IH) is assumed in the fit. We reiterate that Fig. 3.18 shows the $\sin^2 2\theta_{13}$ sensitivity after marginalizing over hierarchy as well. In other words, the sensitivity shown in this figure corresponds to the statistically weaker channel. For the case where the same γ for ^{8}B and ^{8}Li has been used, the neutrino channel is weaker since the event rate is about 1.5 times less than antineutrino events with the same γ. On the other hand when we scale down the Lorentz boost for ^{8}Li, the flux in the antineutrino channel goes down significantly and hence it becomes the statistically weaker channel as can be seen from Fig. 3.13 and therefore the marginalized

---

[18] Note that since $\sin^2 2\theta_{13}(\text{true}) = 0$, the data is independent of the δ_{CP}(true) and the true mass hierarchy. However, since we allow for non-zero $\sin^2 2\theta_{13}$ in the fit, the predicted event rates in our "theory" depend on δ_{CP} and the mass hierarchy.

χ^2 corresponds mainly to that from antineutrinos. Indeed one can check that the $\sin^2 2\theta_{13}$ sensitivity that we exhibit by the blue dashed line for the scaled γ case is comparable to what one can obtain for the antineutrino channel with IH and the corresponding lower γ. Similar feature is observed in addressing the issue of neutrino mass ordering taking IH as true hierarchy (see right panel of Fig. 3.14) and the γ for the antineutrinos is scaled down by a factor of 1.67 with respect to the γ of the neutrino beam.

The dependence of the $\sin^2 2\theta_{13}$ sensitivity on the number of useful radioactive ion decays per year in the straight section of the storage ring is shown in the right panel of Fig. 3.17. Here we have taken the same Lorentz boost for ^{8}B and ^{8}Li and we have shown the results for three fixed values of γ. The relative increase in the sensitivity by increasing γ and/or the number of useful ion decays per year by the same factor is quantified in the last two columns of Table 3.5.

3.7.2 $\sin^2 2\theta_{13}$ Discovery Reach

How good are our chances of observing a positive signal for oscillations and hence θ_{13} in the CERN-INO beta-beam set-up? We answer this question in terms of the parameter indicator which we call the "discovery reach" of the experiment for $\sin^2 2\theta_{13}$. This performance indicator is defined as the range of $\sin^2 2\theta_{13}$(true) values which allow us to rule out $\sin^2 2\theta_{13} = 0$ at the 3σ C.L. To find this we simulate the data at some non-zero value of $\sin^2 2\theta_{13}$(true) and fit it by assuming that $\sin^2 2\theta_{13} = 0$, allowing all other oscillations parameters to take any possible value in order to return back the smallest value for the χ^2. Note that since the fitted value of θ_{13} in this case always corresponds to 0, there is no need of any marginalizing over the hierarchy when fitting the data. However, since the data here is generated at a non-zero value of $\sin^2 2\theta_{13}$(true), it depends on the true mass hierarchy. The discovery reach of the experiment is therefore expected to be dependent on the true mass hierarchy. Likewise, while the value of δ_{CP} in the fit is inconsequential as $\sin^2 2\theta_{13} = 0$ in the fit, the data itself and hence the discovery reach, would depend on δ_{CP}(true). For each $\sin^2 2\theta_{13}$(true), we generate the data for all possible values of δ_{CP}(true) and for both the true mass hierarchies. For each case, the data is then fitted assuming $\sin^2 2\theta_{13} = 0$ and marginalizing over the other oscillation parameters, returning a value of $\chi^2_{\rm min}$ for each data set. We choose the minimum amongst these $\chi^2_{\rm min}$ and find the value of $\sin^2 2\theta_{13}$(true) for which we could claim a signal in the detector at the 3σ C.L. In the right panel of Fig. 3.18 we show this "most conservative"[19] $\sin^2 2\theta_{13}$ discovery reach of our experiment as a function of γ. We assume equal γ for both the ions for the red solid curve. One can see that for $\gamma = 650$, the most conservative discovery reach is $\sin^2 2\theta_{13}(\text{true}) = 5.11 \times 10^{-4}$ while if $\delta_{CP}(\text{true}) = 0$ then we have checked that the reach is slightly better and this will be $\sin^2 2\theta_{13}(\text{true}) = 5.05 \times 10^{-4}$. For the blue dashed line we assume that the γ for ^{8}Li is scaled down by a factor of 1.67 compared to that for ^{8}B, plotted on the x-axis. Since for same γ, neutrino is the statistically weaker channel, the red line mainly corresponds to what we expect for the true NH. For the scaled γ case since the antineutrino channel becomes statistically

---

[19] This is "most conservative" in the sense that no matter what the choices of δ_{CP}(true) and the true neutrino mass ordering, the θ_{13} discovery limit cannot be worse than the value presented.

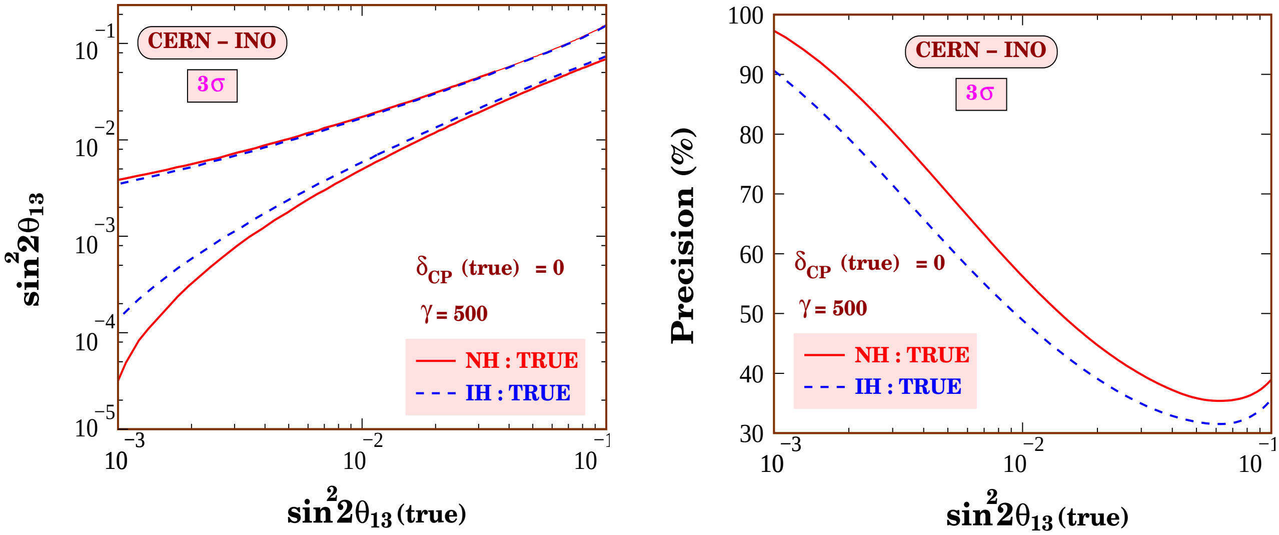

Figure 3.19: The precision with which $\sin^2 2\theta_{13}$ will be measured by the CERN-INO beta-beam experiment as a function of $\sin^2 2\theta_{13}$(true). Left panel shows the 3σ allowed range of $\sin^2 2\theta_{13}$ while the right panel shows the precision defined in the text.

weaker, the lower χ^2 comes from this channel and the blue dashed line corresponds to what we expect for the true IH.

3.7.3 $\sin^2 2\theta_{13}$ Precision

In Fig. 3.19 we show how *precisely* the mixing angle $\sin^2 2\theta_{13}$ will be measured, if we observe a θ_{13} driven signal at the detector. The left panel depicts as a function of $\sin^2 2\theta_{13}$(true) the corresponding range of allowed values of $\sin^2 2\theta_{13}$ at the 3σ C.L. We have assumed $\gamma = 500$ and $\delta_{CP}(\text{true}) = 0$. The solid line is assuming NH to be true, while the dashed line is for IH true. Note that in the fit we always marginalize over the hierarchy and δ_{CP}. The right panel shows the variable "precision" which we define as

$$\text{precision} = \frac{(\sin^2 2\theta_{13})_{max} - (\sin^2 2\theta_{13})_{min}}{(\sin^2 2\theta_{13})_{max} + (\sin^2 2\theta_{13})_{min}} \times 100\,\%\ , \tag{3.31}$$

where $(\sin^2 2\theta_{13})_{max}$ and $(\sin^2 2\theta_{13})_{min}$ are the maximum and minimum allowed values of $\sin^2 2\theta_{13}$ respectively at 3σ.

3.8 Summary and Conclusions

Long baseline experiments which will use the golden $P_{e\mu}$ channel for determining the neutrino oscillation parameters face a serious threat from the menace of clone solutions due to the so-called parameter degeneracies. These degeneracies come in three forms: the $\delta_{CP} - \theta_{13}$ intrinsic degeneracy, the $\delta_{CP} - sgn(\Delta m^2_{31})$ degeneracy and the θ_{23} octant degeneracy, and necessarily result in degrading the sensitivity of the experiment. The CERN-INO near-magic distance of 7152 km offers the possibility of setting up an experiment at a baseline where the δ_{CP} dependent terms almost drop out from the expression of the golden channel probability. Thus two out of the three degeneracies are evaded, providing a platform for clean measurement of θ_{13} and $sgn(\Delta m^2_{31})$, two major players in our understanding of the origin of neutrino masses and mixing. A large magnetized iron calorimeter with a total mass of at least 50 kton is expected to be built soon at INO. It will be ideal for detecting multi-GeV ν_μ and hence can be used as the far detector for a high energy beta-beam.

In this chapter we studied in detail the physics reach of the CERN-INO magical beta-beam set-up. For $\gamma = 650$, $\delta_{CP}(\text{true}) = 0$ and true NH, the sensitivity to hierarchy determination at 3σ is $\sin^2 2\theta_{13}(\text{true}) = 5.51 \times 10^{-4}$ when full spectral data from neutrino and antineutrino channels are combined. Even though the effect of $\delta_{CP}(\text{true})$ on the event rate of such an experiment is expected to be small, there is some residual dependence on it because the CERN-INO distance does not conform to the exact magic baseline. We studied the change in the hierarchy sensitivity due to the uncertainty in δ_{CP}. It turns out that for $\gamma = 650$ and with NH (IH) true, the best sensitivity to hierarchy determination corresponds to $\sin^2 2\theta_{13}(\text{true}) = 3.96 \times 10^{-4}$ ($\sin^2 2\theta_{13}(\text{true}) = 2.96 \times 10^{-4}$), while the worst case is $\sin^2 2\theta_{13}(\text{true}) = 5.58 \times 10^{-4}$ ($\sin^2 2\theta_{13}(\text{true}) = 3.59 \times 10^{-4}$).

A detailed analysis of the potential of probing θ_{13} at this experiment has been presented here. We defined and studied the θ_{13} reach in terms of three performance indicators: the sensitivity reach, the discovery reach and the precision of $\sin^2 2\theta_{13}$ measurement. The θ_{13} sensitivity reach is defined as the range of $\sin^2 2\theta_{13}$ which is incompatible with the data generated for $\sin^2 2\theta_{13}(\text{true}) = 0$ at the 3σ C.L. The sensitivity reach corresponds to $\sin^2 2\theta_{13} = 1.14 \times 10^{-3}$ at 3σ C.L. for $\gamma = 650$ and this is independent of the true hierarchy and $\delta_{CP}(\text{true})$. The discovery reach is defined as the range of true values of the mixing angle for which we have an unambiguous oscillation signal in the detector. At 3σ C.L. the discovery reach corresponds to $\sin^2 2\theta_{13}(\text{true}) = 5.05 \times 10^{-4}$ ($\sin^2 2\theta_{13}(\text{true}) = 2.96 \times 10^{-4}$) for $\gamma = 650$, $\delta_{CP}(\text{true}) = 0$ and NH (IH) true while the most conservative limit irrespective of $\delta_{CP}(\text{true})$ and the true neutrino mass ordering is $\sin^2 2\theta_{13}(\text{true}) = 5.11 \times 10^{-4}$. We also presented the expected precision with which $\sin^2 2\theta_{13}$ would be determined in this experiment for $\sin^2 2\theta_{13}(\text{true}) > 10^{-3}$.

Neutrino physics is in wait for the next great leap forward in the decade ahead. The study of the golden channel probability $P_{e\mu}$ using a beta-beam neutrino source and an iron calorimeter detector at a very long magical baseline may well turn out, as we have demonstrated in this chapter, to be very crucial in this endeavour. In the next chapter, we will discuss the impact of matter effects in the ν_e survival probability at long baselines in extracting the information about the neutrino mass ordering and the 1-3 mixing angle.

Chapter 4

Neutrino parameters from matter effects in P_{ee} at long baselines

4.1 $\boxed{\text{Introduction}}$

Determination of the 1-3 neutrino mixing angle θ_{13}, sgn(Δm^2_{31}), the three CP phases and the absolute neutrino mass scale are necessary for reconstruction of the neutrino mass matrix, which will have important consequences for nuclear and particle physics, astrophysics and cosmology. The golden channel $P_{e\mu}$ has the capability of measuring the Dirac phase δ_{CP}, $sgn(\Delta m^2_{31})$ and θ_{13} in long baseline accelerator based experiments. However, this strength of the golden channel also brings in the well-known problem of parameter "degeneracies", where one gets multiple fake solutions in addition to the true one [93, 94, 95, 96]. Various ways to combat this vexing issue have been suggested in the literature, including combining the golden channel with the "silver" ($P_{e\tau}$) [106] and "platinum" ($P_{\mu e}$) channels. While each of them would have fake solutions, their combination helps in beating the degeneracies since each channel depends differently on δ_{CP}, $sgn(\Delta m^2_{31})$ and θ_{13}. In this chapter, we focus on the $\nu_e \to \nu_e$ survival channel, P_{ee}, which is *independent* of δ_{CP} and the mixing angle θ_{23}. It is therefore *completely* absolved of degeneracies and hence provides a clean laboratory for the measurement of $sgn(\Delta m^2_{31})$ and θ_{13}. This gives it an edge over the conversion channels, which are infested with degenerate solutions.

The P_{ee} survival channel has been extensively considered for measuring θ_{13} with $\bar{\nu}_e$ produced in nuclear reactors [121] and with detectors placed at a distance $\simeq 1$ km. Reducing systematic uncertainties to the sub-percent level is a prerequisite for this program and enormous R&D is underway for this extremely challenging job. For accelerator based experiments, the survival channel, P_{ee}, has been discussed with sub-GeV neutrinos from a beta-beam source at CERN and a megaton water detector in Fréjus at a baseline of 130 km [62, 63, 65, 107]. However, no significant improvement on the θ_{13} limit was found in [107] for a systematic error of $\gtrsim$ 5%. This stems mainly from the fact that in these experiments one is trying to differentiate between two scenarios, both of which predict a large number of events, differing from each other by a small number due to the small value of θ_{13}. Also, since $sgn(\Delta m^2_{31})$, is ascertained using earth matter effects, there is no hierarchy sensitivity in these survival channel experiments due to the short baselines involved.

In this chapter, we emphasize on the existence of large matter effects in the survival channel, P_{ee}, for an experiment with a very long baseline. Recalling that $P_{ee} = 1 - P_{e\mu} - P_{e\tau}$ and since for a given $sgn(\Delta m^2_{31})$ *both* $P_{e\mu}$ and $P_{e\tau}$ will either increase or decrease in matter, the change in P_{ee} is almost twice that in either of these channels. Using the multi-GeV ν_e flux from a beta-beam source, we show that this large matter effect allows for significant, even maximal, deviation of P_{ee} from unity. This, can thus be a convenient tool to explore θ_{13}. This is in contrast to the reactor option or the beta-beam experimental set-up in [107], where increasing the neutrino flux and reducing the systematic uncertainties are the only ways of getting any improvement on the current θ_{13} limit. We further show, for the first time, that very good sensitivity to the neutrino mass ordering can also be achieved in the P_{ee} survival channel owing to the large matter effects. We discuss plausible experimental set-ups with the survival channel and show how the large matter effect propels this channel, transforming it into a very useful tool to probe $sgn(\Delta m^2_{31})$ and θ_{13} even with relatively large room for systematic uncertainties.

4.2 The $\nu_e \to \nu_e$ Survival Probability

Under one mass scale dominance and the constant density approximation, the matter conversion probabilites are,

$$P_{ex} = Y_{23} \sin^2 2\theta^m_{13} \sin^2 \left[1.27(\Delta m^2_{31})^m L/E\right], \tag{4.1}$$

where $Y_{23} = \sin^2\theta_{23}$ for $x = \mu$ and $Y_{23} = \cos^2\theta_{23}$ for $x = \tau$. Then we have

$$P_{ee} = 1 - P_{e\mu} - P_{e\tau} = 1 - \sin^2 2\theta^m_{13} \sin^2 \left[1.27(\Delta m^2_{31})^m L/E\right]. \tag{4.2}$$

The largest deviation of P_{ee} from unity is obtained when the conditions 3.14 and 3.15 are satisfied simultaneously. This ensures maximum matter effect in the conversion channels (see Eqs. 3.17 and 3.18). However, there are suppression factors, $\sin^2\theta_{23}$ for $P_{e\mu}$ and $\cos^2\theta_{23}$ for $P_{e\tau}$, not present in P_{ee}. Moreover, since P_{ee} does not contain θ_{23}, the octant ambiguity as well as parameter correlations due to uncertainty in θ_{23} [95] are absent. In addition, as mentioned earlier, the P_{ee} channel does not contain the CP phase, δ_{CP} and therefore this channel does not suffer from the effect of the so-called $(\theta_{13}, \delta_{CP})$ intrinsic degeneracy [93] and the (sgn(Δm^2_{31}), δ_{CP}) degeneracy [94]. Both of these remain true in the presence of non-zero Δm^2_{21} [122].

Using Eq. 3.18, one can estimate the distance where $P_{ee} \simeq 0$ for a given value of θ_{13}. For instance for $p = 0$ and $\sin^2 2\theta_{13} = 0.2$ and 0.1, these distances are 7600 km and 10200 km respectively which can be readily seen from Fig. 3.6. For higher values of p the distance exceeds the earth's diameter for θ_{13} in the current allowed range. Using $(\rho L)^{max}$ corresponding to the PREM profile, from Eq. 3.18 one can estimate that the condition of maximal matter effects inside the earth's mantle is satisfied only for $\sin^2 2\theta_{13} \gtrsim 0.09$. In our numerical work, we solve the full three flavour neutrino propagation equation assuming the PREM [110] profile and keep Δm^2_{21} and $\sin^2\theta_{12}$ fixed at their present best-fit values of 8.0×10^{-5} eV^2 and 0.31 respectively

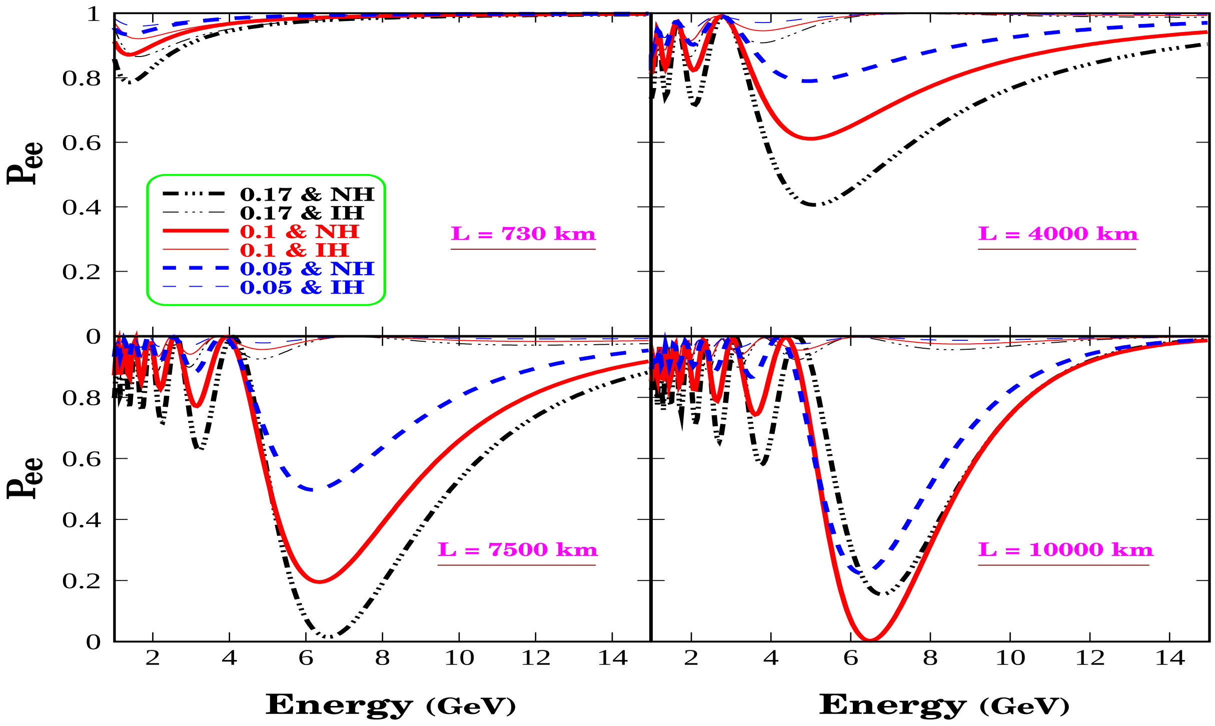

Figure 4.1: The survival probability P_{ee} in matter as a function of E for four different values of the baseline L. For each L, the plots are given for three different values of $\sin^2 2\theta_{13}$ (0.17, 0.1 and 0.05). Thick (thin) lines are for NH (IH).

[78] as mentioned in the first column of Table 3.2. For the other oscillation parameters, the benchmark values are also taken from the same table.

In Fig. 4.1 we plot P_{ee} as a function of energy, at four different L and for three values of $\sin^2 2\theta_{13}$. The plots confirm that maximal matter effects come at $L \simeq 10000$ km and $L \simeq 7500$ km for $\sin^2 2\theta_{13} = 0.1$ and 0.17 respectively for the normal hierarchy (NH). For the inverted hierarchy (IH) there is no significant matter effect for ν_e. This large difference in the probabilities for NH and IH can be exploited for the determination of $sgn(\Delta m^2_{31})$. Further, since the matter effect is a sensitive function of θ_{13} it may also be possible to obtain information on this angle. We can also see that for a given value of $\sin^2 2\theta_{13}$ ($\gtrsim 0.09$) and E, the matter effect increases (almost linearly) with L, until the L for maximal matter effect is reached, beyond which matter effect falls. For values of $\sin^2 2\theta_{13} < 0.09$ the condition for maximum matter effect is not met inside the earth's mantle and hence the matter effect and sensitivity to both hierarchy as well as θ_{13} increase with L.

In what follows, we will show how, in a plausible experiment, one can use this near-resonant matter effect in the survival channel, P_{ee}, to constrain θ_{13} and $sgn(\Delta m^2_{31})$. Fig. 4.1 shows that the requirements for such a program include

1. $\boxed{\textbf{a } \nu_e \textbf{ beam,}}$

2. **a baseline of at least a few thousand km,**
3. **average energies around 6 GeV,**
4. **a detector capable of observing e^- unambiguously at these energies.**

4.3 The Experimental Set-up

4.3.1 Pure ν_e ($\bar{\nu}_e$) Source

The various issues related to beta-beams have already been discussed in great detail in section 3.2 of the previous chapter. The ions considered as possible sources for beta-beams are ^{18}Ne and ^{8}B for ν_e and ^{6}He and ^{8}Li for $\bar{\nu}_e$. The end point energies of ^{6}He and ^{18}Ne are $\sim$ 3.5 MeV while for ^{8}B and ^{8}Li this can be larger $\sim$ 13-14 MeV (see Table 1.1). For the Lorentz boost factor $\gamma = 250$ (500) the ^{8}B and ^{8}Li sources have peak energy around $\sim$ 4 (7) GeV. Since this is in the ball-park of the energy necessary for near-resonant matter effects as discussed above, we will work with ^{8}B (^{8}Li) as the source ion for the ν_e ($\bar{\nu}_e$) beta-beam and $\gamma = 250$ and 500.

4.3.2 Water Čerenkov Detector

Water Čerenkov detectors have excellent capability of separating electron from muon events. Since this technology is very well known, megaton water detectors are considered to be ideal for observing beta-beams. Proposals for megaton water detectors include UNO [123] in USA, HyperKamiokande [124] in Japan and MEMPHYS [125] in Europe. If the beta-beam is produced at CERN, then baselines in the range 7000-8600 km would be possible at any of the proposed locations for the UNO detector. Likewise, if the beta-beam source be at FNAL, then the far detector MEMPHYS would allow for $L = 7313$ km. HyperKamiokande could also be considered as the far detector and in that case $L = 10184$ (9647) km if the source be at FNAL (CERN). Such detectors do not have any charge identification capacity. But in a beta-beam, the β^- and β^+ emitters can be stacked in different bunches and the timing information at the detector can help to identify the e^- and e^+ events [60].

4.3.3 Backgrounds

It is well known that there are no beam induced backgrounds for beta-beams. In the previous chapter (subsection 3.4.3), these issues have been addressed in detail. In this experimental set-up, the process $\nu_e \rightarrow \nu_\tau \rightarrow \tau^- \rightarrow e^-$ could mimic the signal. We have checked that the background to signal ratio for these events in the relevant energy range is $\sim 10^{-2}$ and can be neglected for the disappearance mode. The electron events from K and π^- decays are also

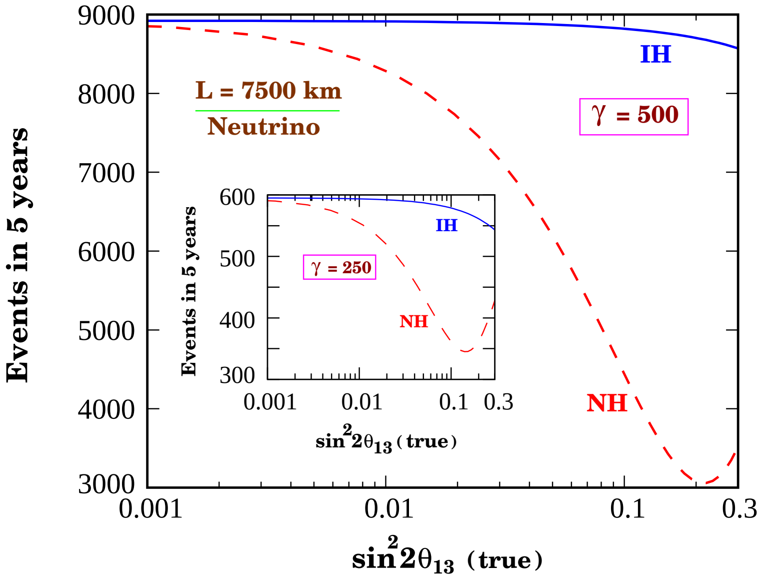

Figure 4.2: Events in 5 years vs. $\sin^2 2\theta_{13}$ for NH (dashed line) and IH (solid line) for $L = 7500$ km and $\gamma = 500$. The inset shows the same but for $\gamma = 250$.

negligible. The atmospheric background can be estimated in the beam off mode and reduced through directional, timing, and energy cuts.

4.4 Simulation Details and Event Rates

For our numerical analysis we use the standard χ^2 technique with

$$\chi^2_{total} = \chi^2_{\nu_e \to \nu_e} + \chi^2_{prior}, \tag{4.3}$$

where[1]

$$\chi^2_{prior} = \left(\frac{|\Delta m^2_{31}| - |\Delta m^2_{31}(\text{true})|}{\sigma(|\Delta m^2_{31}|)} \right)^2 . \tag{4.4}$$

$\chi^2_{\nu_e \to \nu_e}$ is calculated using the same expression that we have used for $\chi^2_{\nu_e \to \nu_\mu}$ (see Eqs. 3.25 & 3.26) in the previous chapter. Here all the results have been presented using the data from only neutrino (^{8}B) run without any spectral information. We have not considered any background[2] in our analysis. We have taken 3% systematical error on signals. The prospective "data" is generated at the "true" values of oscillation parameters as given in the Table 3.2, assuming 440 kton of fiducial volume for the detector with 90% detector efficiency, threshold of 4 GeV and

---

[1] No prior is taken on θ_{23} because P_{ee} is independent of θ_{23}. Here we have kept Δm^2_{21} and $\sin^2\theta_{12}$ fixed at their present best-fit values in the fit. No uncertainty has been taken in the PREM profile when we fit the simulated data.

[2] Backgrounds are not important here because we are dealing with the survival channel (P_{ee}) and the number of events is also quite large.

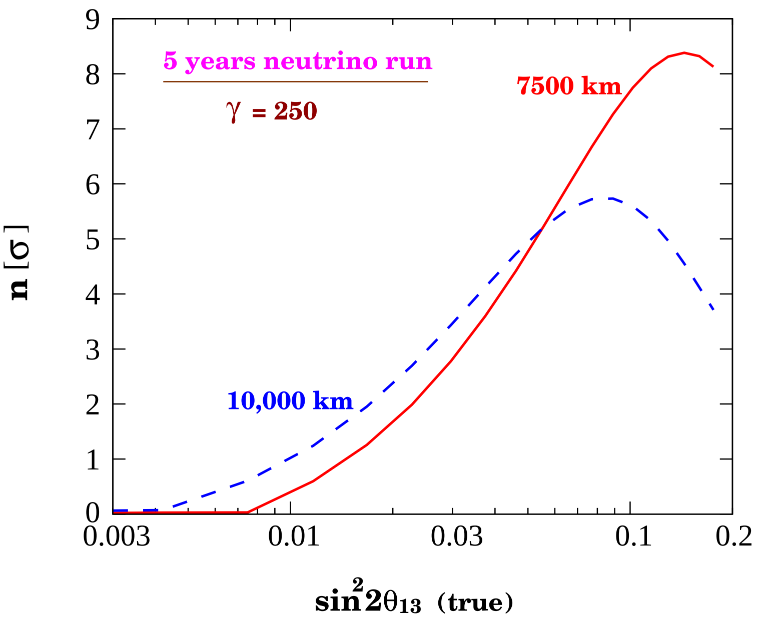

Figure 4.3: Sensitivity to hierarchy for $L = 7500$ (solid line) and 10000 km (dashed line) and $\gamma = 250$, as a function of $\sin^2 2\theta_{13}$(true).

energy smearing of width 15%. For the ν_e beta-beam we have assumed 1.1×10^{18} useful ^{8}B decays per year and show results for 5 years of running of this beam. The number of events as a function of $\sin^2 2\theta_{13}$ at $L = 7500$ km with a $\gamma = 500$ ν_e beta-beam is shown in Fig. 4.2 for NH and IH. The inset in Fig. 4.2 shows the number of events in 5 years expected from a lower $\gamma = 250$. We have used the neutrino-nucleon interaction cross-sections from the Globes package [117] which are taken from [118, 119].

4.5 Sensitivity to $\mathrm{sgn}(\Delta m^2_{31})$ and θ_{13}

In Fig. 4.3, we show the sensitivity ($n\sigma$, $n = \sqrt{\chi^2}$) of the survival channel to the neutrino mass ordering for $L = 7500$ and 10000 km and $\gamma = 250$. If the true value of $\sin^2 2\theta_{13} = 0.05$, then one can rule out the IH at the 4.8σ (5.0σ) C.L. with $L = 7500$ (10000) km. For $L = 7500$ (10000) km, the wrong IH can be disfavored at the 90% C.L. if the true value of $\sin^2 2\theta_{13} > 0.03$ (0.025). The sensitivity improves significantly if we use $\gamma = 500$ instead of 250, since (i) the flux at the detector increases, and (ii) the flux peaks at E closer to 6 GeV, where we expect largest matter effects. For $\gamma = 500$ and $L = 7500$ (10000) km, the IH can be disfavored at 2.6σ (3.8σ) C.L. for a lower value of $\sin^2 2\theta_{13}(\text{true}) = 0.015$. The range of $\sin^2 2\theta_{13}$(true) for which the IH can be ruled out at 90% and 3σ C.L. for different values of L are shown in the upper panel of Fig. 4.4 for $\gamma = 250$ and 500. From the figure one can see that for $\gamma = 500$ and $L =$ 7500 (10000) km the wrong IH can be disfavored at the 90% C.L. if $\sin^2 2\theta_{13}(\text{true}) > 1.0 \times 10^{-2}$

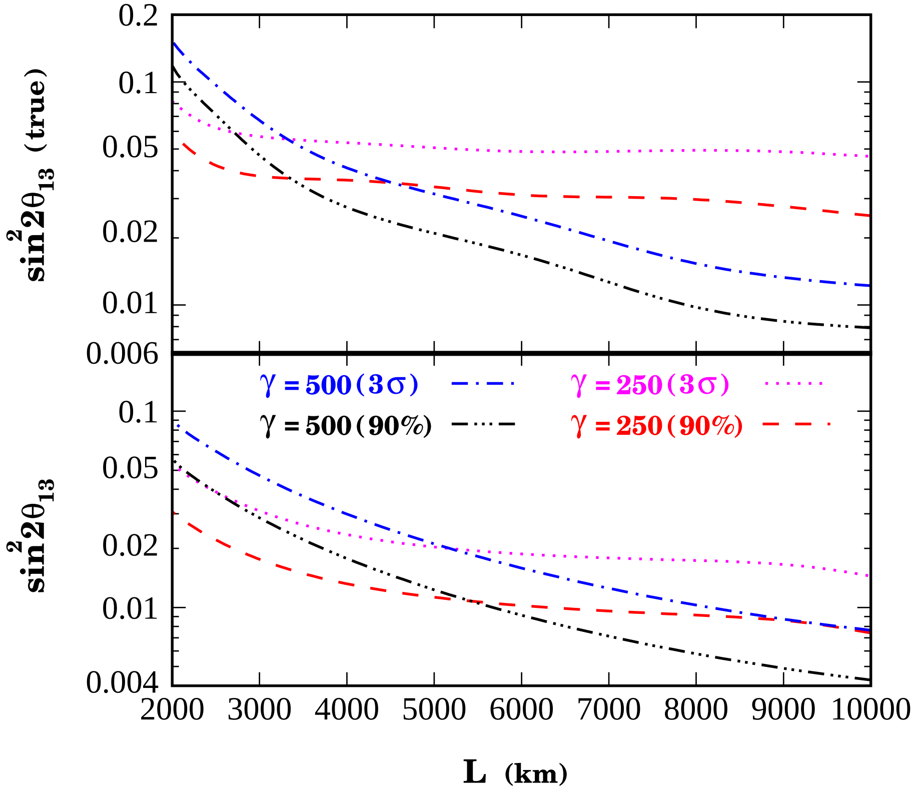

Figure 4.4: The upper panel shows the range of $\sin^2 2\theta_{13}$(true) for which the wrong IH can be excluded at 90% and 3σ C.L. while the lower panel gives the sensitivity to $\sin^2 2\theta_{13}$ at various baselines at 90% and 3σ C.L., for two values of γ.

(8.0×10^{-3}). If instead we use a total systematic error of 5% then we get the above sensitivity limits as $\sin^2 2\theta_{13}(\text{true}) > 1.6 \times 10^{-2}$ (1.2×10^{-2}) at 90% C.L.

If the $\sin^2 2\theta_{13}$(true) turns out to be smaller than the sensitivity reach shown in the upper panel of Fig. 4.4 for a given L, then it would not be possible to determine the hierarchy at the given C.L. However, we would still be able to put better constraints on $\sin^2 2\theta_{13}$ itself. The lower panel of Fig. 4.4 demonstrates as a function of L, the sensitivity to θ_{13}, i.e., the range of $\sin^2 2\theta_{13}$ which is incompatible with the data generated for $\sin^2 2\theta_{13}(\text{true}) = 0$ at 90% and 3σ C.L. Both Figs. 4.3 and 4.4 show that the sensitivity improves with L, even though the flux falls as $1/L^2$. This results from matter effects increasing with L, as noted before. For $L = 7500$ (10000) km, we can constrain $\sin^2 2\theta_{13} < 6.3 \times 10^{-3}$ (4.3×10^{-3}) at the 90% C.L. for γ =500. For a 5% systematic error the above numbers are changed to $\sin^2 2\theta_{13} < 1.0 \times 10^{-2}$ (7.3×10^{-3}).

How does this compare with alternate possibilities? If the energy can be reconstructed accurately, then the result can be improved further. For instance, for L=7500 km, if one could preferentially select the energy in the range 5 to 7.5 GeV, then the wrong IH can be excluded from true NH for $\sin^2 2\theta_{13}(\text{true}) = 7.47 \times 10^{-3}$ at 90% C.L. for $\gamma = 500$.

We have presented our results using a ν_e beam and assuming NH to be the true hierarchy. Similar results can also be obtained with a $\bar{\nu}_e$ beam for IH. It is also possible to run both beams simultaneously.

4.6 $\boxed{\text{Discussions and Conclusions}}$

In conclusion, we propound the possibility of using large matter effects in the survival channel, P_{ee}, at long baselines for determination of the neutrino mass ordering ($sgn(\Delta m^2_{31})$) and the yet unknown leptonic mixing angle θ_{13}. Matter effects in the transition probabilites $P_{e\mu}$ and $P_{e\tau}$ act in consonance to give an almost two-fold effect in the survival channel. In addition, the problem of spurious solutions due to the leptonic CP phase and the atmospheric mixing angle θ_{23} does not crop up. The development of beta-beams as sources of pure $\nu_e/\bar{\nu}_e$ beams enables one to exclusively study the P_{ee} survival probability and adds a new direction to the prospects of a future beta-beam. In the next chapter, we will study the performance of the magical CERN-INO beta-beam set-up in exploring the signals of new physics which are present in the R-parity violating supersymmetric models.

Chapter 5

Can R-parity violating supersymmetry be seen in long baseline Beta-beam experiments?

5.1 Introduction

Long baseline neutrino oscillation experiments using beta-beam hold promise of refining our knowledge on the third mixing angle θ_{13}, $\text{sgn}(\Delta m^2_{31})$ and the CP phase δ_{CP}, vital missing parameters of the neutrino mass matrix. The phenomenon of neutrino oscillation firmly establishes the evidence for physics beyond the Standard Model and the sub dominant effects due to possible new physics can leave their imprints in the future long baseline beta-beam experiments which are supposed to give us precision below 1%. In this chapter, we will try to address the following questions :

1. **Can the proposed magical CERN-INO long baseline beta-beam neutrino experiment probe non-standard interactions (NSI) that are present in RPVSM?**
2. **Can these NSI become fatal in attempts to further sharpen our understanding of the neutrino properties?**
3. **Can new physics leave its imprints at the propagation stage of neutrinos?**

Interaction of neutrinos with matter affect long baseline experiments and this becomes more prominent at higher values of θ_{13}. Various authors [108, 116, 126] have considered this effect for atmospheric neutrinos. Apart from the electroweak effects, there may well be NSI leading to flavour diagonal and flavour changing neutral currents. Here we have in mind interactions with quarks and leptons involving an initial and a final neutrino. If there is no change in the neutrino flavour – as, for example, in Z^0 exchange – this is classified as an FDNC process, while it would be FCNC otherwise. RPVSM [80], which have such interactions already built-in[1], will be the main focus of our work. Recently a model in which couplings associated with FCNC and FDNC can be quite a bit higher than permitted in RPVSM has also been considered [127, 128]. Naturally, here the matter effect will be further enhanced. However, as RPVSM is a well-studied, renormalizable model which can satisfy all phenomenological constraints currently available, we shall restrict our main analysis only to it and shall make qualitative remarks about the other model, for which our results can be easily extended.

Consequences of FCNC and FDNC for solar and atmospheric neutrinos [10, 129, 130], and neutrino factory experiments [131] have been looked into. Our focus is on long baseline beta-beam experiments. Our analysis encompasses both NH and IH and we also incorporate all relevant trilinear R-parity violating couplings leading to FCNC and FDNC. Huber *et al* [132] have a somewhat similar analysis using neutrino beams obtained from muon decays.

The very long baseline from CERN to INO will capture a significant matter effect and offers a scope to signal NSI. We examine whether the presence of R-parity violating ($\not{R}$) interactions will come in the way of constraining the mixing angle θ_{13} or unraveling the neutrino mass ordering. The possibility to obtain bounds on some $\not{R}$ couplings is also probed.

5.2 $\boxed{\not{R}\ \textbf{Supersymmetry}}$

In supersymmetric theories [80], gauge invariance does not imply baryon number (B) and lepton number (L) conservation. In the minimal supersymmetric Standard Model, L and B conservation is ensured by invoking 'R-parity' (defined as $R = (-1)^{3B+L+2S}$ where S is the spin). It is a discrete Z_2 symmetry under which the Standard Model particles are even and their superpartners are odd. The imposition of such a symmetry, while it serves a purpose, is rather *ad hoc*. In general, from the naïve theoretical point of view it is expected that L and B conservation does not hold in supersymmetric theories. However, as this leads to a very fast proton decay, we follow a common practice and assume that B is conserved. This can be ensured by replacing the Z_2 symmetry of R-parity by a Z_3 symmetry, the so-called 'baryon triality' [133]. In such a scenario, in addition to the usual Yukawa interactions, the superpotential contains renormalizable L-violating trilinear λ- and λ'-type couplings and bilinear μ_i couplings :

$$W_{\not{L}} = \sum_{i,j,k} \frac{1}{2}\lambda_{ijk} L_i L_j E^c_k + \lambda'_{ijk} L_i Q_j D^c_k + \mu_i L_i H_u, \tag{5.1}$$

where $i, j, k = 1, 2, 3$ are generation indices and colour and $SU(2)$ indices are suppressed. Here L_i and Q_i are $SU(2)$-doublet lepton and quark superfields respectively; E_i, D_i denote the right-handed $SU(2)$-singlet charged lepton and down-type quark superfields respectively; H_u is the Higgs superfield which gives masses to up-type quarks. Particularly, λ_{ijk} is antisymmetric under the interchange of the first two generation indices. The bilinear couplings, μ_i, are severely constrained by the small neutrino masses. So we will discuss the phenomenology of λ- and λ'-type couplings only. Then, expanding the above superpotential in standard four-component Dirac notation, we have for λ'-type couplings

---

[1] *e.g.* through squark (λ'-type couplings) or slepton (λ-type couplings) exchange.

$$\begin{aligned}\mathcal{L}_{\lambda'} \;=\; \lambda'_{ijk}\, [\, & \tilde{d}^j_L\, \bar{d}^k_R \nu^i_L + (\tilde{d}^k_R)^* (\bar{\nu}^i_L)^c d^j_L + \tilde{\nu}^i_L \bar{d}^k_R d^j_L \\ & - \tilde{e}^i_L \bar{d}^k_R u^j_L - \tilde{u}^j_L\, \bar{d}^k_R e^i_L - (\tilde{d}^k_R)^* (\bar{e}^i_L)^c u^j_L] + \text{h.c.},\end{aligned} \tag{5.2}$$

where only the first two terms and their hermitian conjugates are relevant for the quark-neutrino interactions inside the matter *via* squark exchange. Above, the sfermion fields are characterized by the tilde sign. For λ-type couplings, one can write

$$\mathcal{L}_{\lambda} \;=\; \frac{1}{2}\lambda_{ijk}\, [\, \tilde{e}^j_L\, \bar{e}^k_R \nu^i_L + (\tilde{e}^k_R)^* (\bar{\nu}^i_L)^c e^j_L + \tilde{\nu}^i_L \bar{e}^k_R e^j_L - (i \leftrightarrow j)] + \text{h.c.}, \tag{5.3}$$

where only the first two terms with $i \leftrightarrow j$ and their hermitian conjugates are responsible for the interactions of neutrinos with the charged leptons inside the matter *via* slepton exchange. The interaction terms given by Eq. 5.2 and 5.3 violate L, as well as lepton flavour number. Suitable combinations of two such terms can lead to processes which are lepton flavour violating but L-conserving. In what follows, all these new physics couplings are assumed to be real but will entertain both positive and negative values. The interactions of neutrinos with electrons and d-quarks in matter induce transitions (i) $\nu_i + d \to \nu_j + d$ and (ii) $\nu_i + e \to \nu_j + e$. (i) is possible through λ' couplings *via* squark exchange for all i, j and through Z exchange for $i = j$ while (ii) can proceed *via* W and Z exchange for $i = j$, as well as through λ couplings *via* slepton exchange for all i, j.

5.3 Golden Channel Oscillations including NSI

The golden channel probability $P_{e\mu}$ in the presence of standard Earth matter effects has been discussed in great detail in section 3.3. Now let us see what are the changes that we would have in the presence of NSI inside the Earth matter. In the mass basis of neutrinos

$$M^2 = \text{diag}(m_1^2, m_2^2, m_3^2) = U^\dagger M_\nu^+ M_\nu U, \tag{5.4}$$

where M_ν is the neutrino mass matrix in the flavour basis and m_1, m_2, and m_3 correspond to masses of three neutrinos. U is the mixing matrix defined by Eq. 2.18. Eq. 2.28 depicts the time evolution of flavour eigenstates (in the presence of three neutrinos) in matter which can be rewritten in the form

$$i\frac{d}{dt}\begin{pmatrix}\nu_e \\ \nu_\mu \\ \nu_\tau\end{pmatrix} = H \begin{pmatrix}\nu_e \\ \nu_\mu \\ \nu_\tau\end{pmatrix}, \tag{5.5}$$

where

$$H = U\left(\frac{M^2}{2E}\right)U^\dagger + R = \frac{\tilde{M}^2}{2E}. \tag{5.6}$$

$\frac{\tilde{M}^2}{2E}$ is the effective mass squared matrix. R is a 3×3 matrix reflecting the matter effect in the form

$$R_{ij} = R_{ij}(\text{Standard Model}) + R_{ij}(\lambda') + R_{ij}(\lambda). \tag{5.7}$$

Specifically,

$$R_{ij}(\text{Standard Model}) = \sqrt{2} G_F N_e \delta_{ij} (i, j = 1), \tag{5.8}$$

$$R_{ij}(\lambda') = \sum_m \left(\frac{\lambda'_{im1} \lambda'_{jm1}}{4m^2(\tilde{d}_m)} N_d + \frac{\lambda'_{i1m} \lambda'_{j1m}}{4m^2(\tilde{d}_m)} N_d \right), \tag{5.9}$$

$$R_{ij}(\lambda) = \sum_{k \neq i,j} \frac{\lambda_{ik1} \lambda_{jk1}}{4m^2(\tilde{l}_k^{\pm})} N_e + \sum_n \frac{\lambda_{i1n} \lambda_{j1n}}{4m^2(\tilde{l}_n^{\pm})} N_e, \tag{5.10}$$

where N_d is the down-quark density in Earth matter. Note that R is a symmetric matrix and also that antineutrinos will have an overall opposite sign for R_{ij}. Assuming Earth matter to be neutral and isoscalar, $N_e = N_p = N_n$ and $N_d = 3N_e$.

The current bounds on the $\not{R}$ couplings [80] imply that the λ' induced contributions to R_{11}, R_{12} and R_{13} are several orders less than $\sqrt{2} G_F N_e$. We neglect those terms in our analysis. The upper bounds on all couplings in $R_{ij}(\lambda)$ are also very tight [80] in comparison to $\sqrt{2} G_F N_e$ and their effect will be discussed later. So, first we consider, in addition to the Standard Model contribution, only

$$\begin{aligned} R_{23} &= R_{32} = \frac{N_d}{4m^2(\tilde{d}_m)} \left(\lambda'_{2m1} \lambda'_{3m1} + \lambda'_{21m} \lambda'_{31m} \right), \\ R_{22} &= \frac{N_d}{4m^2(\tilde{d}_m)} \left(\lambda'^{\,2}_{2m1} + \lambda'^{\,2}_{21m} \right) \ , \ R_{33} = \frac{N_d}{4m^2(\tilde{d}_m)} \left(\lambda'^{\,2}_{3m1} + \lambda'^{\,2}_{31m} \right), \end{aligned} \tag{5.11}$$

which are comparable to $\sqrt{2} G_F N_e$. One can see from Eq. 5.11 that $R_{23} \neq 0$ implies both R_{22} and R_{33} are non-zero[2].

The current bounds on the relevant couplings are as follows [80] :

$$|\lambda'_{221}, \lambda'_{231}| < 0.18; \ |\lambda'_{21m}| < 0.06; \ |\lambda'_{331}| < 0.58; \ |\lambda'_{321}| < 0.52; \ |\lambda'_{31m}| < 0.12, \tag{5.12}$$

for down squark mass $m_{\tilde{d}} = 100$ GeV. The chosen limits on λ'_{21m} and λ'_{31m} do not conflict with the ratio $R_{\tau\pi} = \Gamma(\tau \longrightarrow \pi \nu_\tau) / \Gamma(\pi \longrightarrow \mu \bar{\nu}_\mu)$ [80]. However, the recently published BELLE bound on the mode $\tau \longrightarrow \mu \pi^0$ [134] tightly constrains precisely those products of the λ' couplings which enter in $R_{23} = R_{32}$ in Eq. (5.11). It has been shown that $|\lambda'_{21m} \lambda'^{*}_{31m}|$ and $|\lambda'_{2m1} \lambda'^{*}_{3m1}|$ both must be $< 1.8 \times 10^{-3} (\frac{\tilde{m}}{100 \text{ GeV}})^2$ [135]. This effectively makes R_{23} negligible for our purposes.

In general, it is cumbersome to write an analytical form of the oscillation probability in the three-flavour scenario with matter effects. However, under certain reasonable approximations it is somewhat tractable. For the energies and baselines under consideration, $\Delta m^2_{21} L/E << 1$ and we can use the one mass scale dominance approximation. Under OMSD, the V_{12} part of U (see Eq. 2.17) drops out from Eq. 5.6. In the special case where $R_{22} = R_{33}$, if one uses the best-fit value of the vacuum mixing angle $\theta_{23} = \pi/4$ then the neutrino mass squared eigenvalues are:

---

[2] However, in other models [127] this may not be the case.

$$\left(\frac{\tilde{M}_2^2}{2E}\right) = R_{22} - R_{23}, \quad \left(\frac{\tilde{M}_{1,3}^2}{2E}\right) = \frac{1}{2}\left(\frac{\Delta m_{31}^2}{2E} + R_{11} + R_{22} + R_{23} \mp B\right), \tag{5.13}$$

where

$$B = \left[\left(\frac{\Delta m_{31}^2}{2E}\right)^2 + \left(-R_{11} + R_{22} + R_{23}\right)^2 - 2\frac{\Delta m_{31}^2}{2E}\cos 2\theta_{13}\left(R_{11} - R_{22} - R_{23}\right)\right]^{1/2}. \tag{5.14}$$

The matter induced neutrino mixing matrix is given by

$$U^m = \begin{pmatrix} U_{11}^m & 0 & U_{13}^m \\ N_1 & -\frac{1}{\sqrt{2}} & N_3 \\ N_1 & \frac{1}{\sqrt{2}} & N_3 \end{pmatrix}. \tag{5.15}$$

Here

$$N_{1,3} = \left[\frac{2\left(-R_{11} + R_{22} + R_{23} + \frac{\Delta m_{31}^2}{2E}\cos 2\theta_{13} \pm B\right)^2}{\left(\frac{\Delta m_{31}^2}{2E}\right)^2 \sin^2 2\theta_{13}} + 2\right]^{-1/2}, \tag{5.16}$$

where N_1 (N_3) corresponds to +(−) sign in the above expression. Neglecting the CP phase δ_{CP} in the standard parameterization of U^m, one may write $U_{13}^m = \sin\theta_{13}^m$ and $U_{23}^m = \sin\theta_{23}^m \cos\theta_{13}^m$. From eq. (5.15) it follows that $\theta_{23}^m = \theta_{23}$, the vacuum mixing angle. θ_{13}^m, on the other hand, changes from its vacuum value and it is $\pi/4$ for

$$R_{11} - R_{22} - R_{23} = \frac{\Delta m_{31}^2}{2E}\cos 2\theta_{13}. \tag{5.17}$$

In the absence of non-standard interactions, $R_{22} = R_{23} = R_{33} = 0$ and $R_{11} = \sqrt{2}G_F N_e$, this is the well-known condition for matter induced maximal mixing (see Eq. 2.26). Since in Eq. 5.15, $U_{12}^m = 0$, in the ν_e to ν_μ oscillation probability the terms involving $(\tilde{M}_2^2 - \tilde{M}_1^2)$ and $(\tilde{M}_3^2 - \tilde{M}_2^2)$ will not survive and we get :

$$P_{\nu_e \to \nu_\mu} = 4\ \left(U_{13}^m\right)^2\ \left(U_{23}^m\right)^2\ \sin^2\left(2.54\ B\ L\right), \tag{5.18}$$

where E, Δm_{31}^2 and L are expressed in GeV, eV^2, and km, respectively. This expression is also valid for antineutrinos. Using Eqs. 5.13 and 5.15 one can easily obtain the oscillation probabilities for other channels.

The above analytical formulation has been used as a cross-check on our numerical results. For example, Fig. 5.1, which shows the variation of $P_{\nu_e \to \nu_\mu}$ as a function of the energy, is obtained by solving the full three flavour neutrino propagation equation assuming the PREM [110] profile and including NSI. The range of energy is chosen in line with the discussions in the rest of this work. The probability falls with decreasing θ_{13} and, for illustration, we have chosen $\sin^2 2\theta_{13} = 0.043$ and for all other oscillation parameters we assume the benchmark values

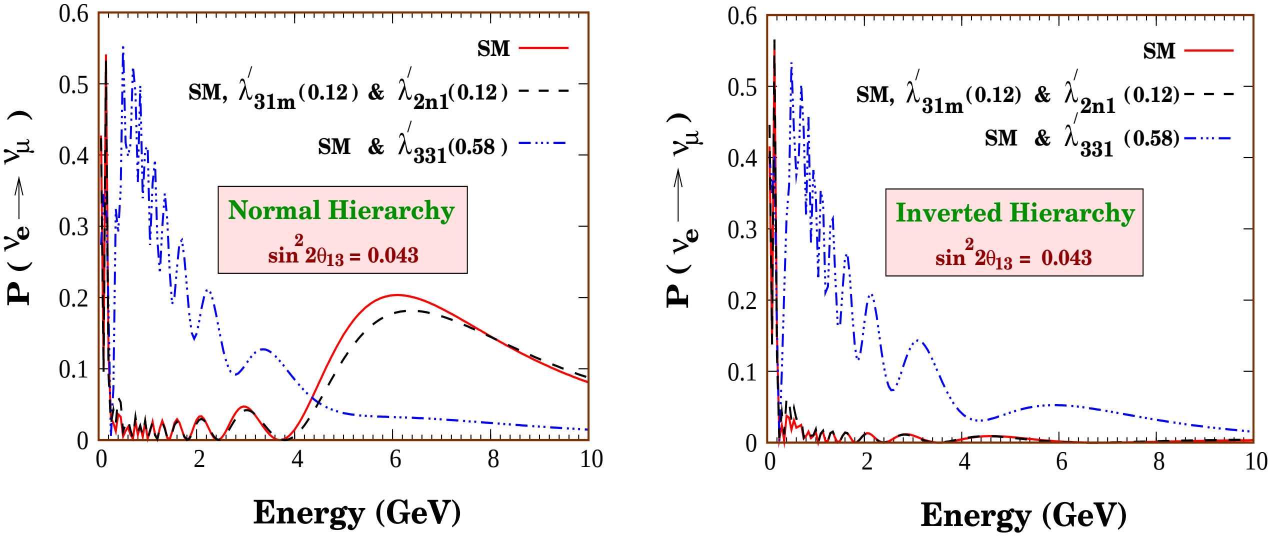

Figure 5.1: $P_{\nu_e \to \nu_\mu}$ for the NH and IH. SM corresponds to only standard electroweak interactions. The values of λ' are given in parentheses. m can take any value, $n = 2$ or 3.

given in Table 3.2. Apart from some qualitative remarks, all the results have been presented considering $\delta_{CP} = 0$ corresponding to the CP conserving case. The purpose of Fig. 5.1 is twofold: (a) to show how the distinguishability between the NH and IH may get blurred by the RPVSM interactions, and (b) how irrespective of the hierarchy chosen by Nature the results may be completely altered by the presence of these interactions. Each panel of Fig. 5.1 has three curves: the solid line (only electroweak interactions), dot-dashed line (in addition, R_{33} gets a non-zero RPVSM contribution), and dashed line ($R_{22} = R_{33}$ are nonzero, in addition to the electroweak contribution). Only in the last case is the analytical formula we have presented above applicable. We find excellent agreement. Two aspects of the results are worth pointing out.

First, in the absence of NSI, for the IH with neutrinos, the resonance condition Eq. 5.17 is not satisfied and the oscillation probability is negligible (right panel solid line). This could be altered prominently by the RPVSM interactions (dot-dashed curve) so that the distinguishability between the two hierarchy scenarios may well get marred by $\not{R}$ supersymmetric interactions.

Secondly, for the NH, it is seen that the peak in the probability may shift to a different energy in the presence of the RPVSM interactions. This is because the condition for maximal mixing in Eq. 5.17 is affected by the $\not{R}$ interactions. For the IH, the oscillation probability is considerably enhanced for some energies. Thus, physics expectations for both hierarchies will get affected by RPVSM.

In the following section we dwell on the full impact of this physics on a long baseline CERN-INO beta-beam experiment.

5.4 Results

In this work the same magical CERN-INO long baseline beta-beam experimental set-up has been considered with which we dealt earlier in chapter 3. Here all the results will be presented taking ^{8}B as the candidate ion for the ν_e beta-beam[3] source and with $\gamma = 350$. All the presented results are based on a five years of ICAL@INO[4] data sample. The event rates have been estimated using Eq. 3.19. Details about the backgrounds and neutrino-nucleon cross sections may be found in section 3.4.

At the production and detection levels, FCNC and FDNC effects can change the spectrum and detection cross sections by a small ($\lesssim 0.1\%$) amount but this would not alter the conclusions. At the source and detector, they may also mimic the oscillation signal itself, but these effects are tiny[5] ($\sim \mathcal{O}(10^{-14})$). Here we discuss how FCNC and FDNC may significantly modify the propagation of neutrinos through matter over large distances.

5.4.1 Extraction of θ_{13} and determination of hierarchy

If neutrinos have only Standard Model interactions then the expected number of muon events is fixed[6] for a particular value of θ_{13} with either NH or IH as may be seen from the solid lines in Fig. 5.2. The vast difference for the alternate hierarchies picks out such long baseline experiments as good laboratories for addressing this open question of the neutrino mass spectrum.

If non-standard interactions are present then, depending on their coupling strength, the picture can change dramatically. In Fig. 5.2, the shaded region corresponds to the allowed values when supersymmetric FCNC and FDNC interactions are at play. It is obtained by letting the λ' couplings[7] vary over their entire allowed range – both positive and negative – given in Eq. 5.12, subject to the further constraints on particular products.

It is seen that to a significant extent the distinguishability of the two hierarchies is obstructed by the $\not{R}$ interactions unless the number of events is more than about 60. Also, the one-to-one correspondence is lost between θ_{13} and the number of events and, at best, a lower bound can now be placed on θ_{13} from the observed number. Of course, if the neutrino mass ordering is known from other experiments, then this lower bound can be strengthened, especially for the inverted hierarchy.

---

[3] Broadly speaking, the results obtained with ^{8}B neutrino beta-beam taking NH (IH) are similar to that with ^{8}Li antineutrino beta-beam source considering IH (NH) but details do differ.

[4] A detailed description of the ICAL@INO detector has already been given in section 3.4 and we use the same detector characteristics as depicted in Table 3.4.

[5] This is due to the very tight constraints from $\mu \to e$ transition limits in atoms [136].

[6] Recall we assume that, but for θ_{13} and the mass hierarchy, the other neutrino mass and mixing parameters are known.

[7] In fact, we have chosen the subscript m in the λ' couplings in Eq. 5.11 to be any one of 1, 2 or 3.

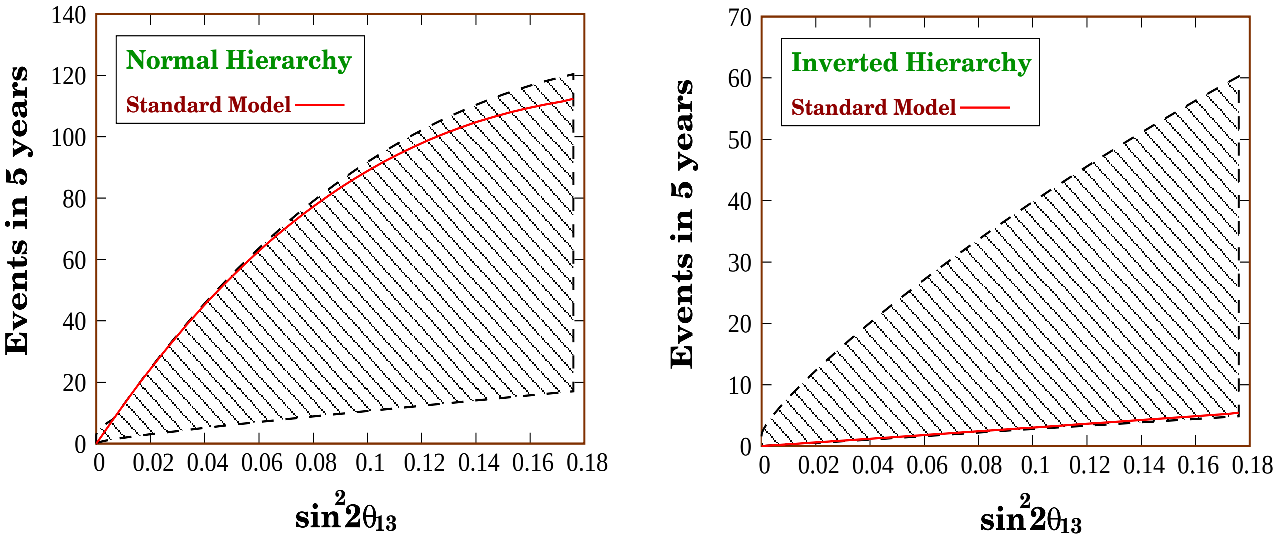

Figure 5.2: Number of muon events for the NH (left panel) and IH (right panel) as a function of $\sin^2 2\theta_{13}$ for a five years of ICAL@INO run. The solid lines correspond to the absence of any NSI. The hatched area is covered if the λ' couplings are varied over their entire allowed range.

It is also noteworthy that for some values of λ'-couplings there may be more events than can be expected from the Standard Model interactions, no matter what the value of θ_{13}. Thus, observation of more than 112 (5) events for the NH (IH) would be a clear signal of new physics.

5.4.2 Constraining λ'

If θ_{13} is determined from other experiments then it will be easier to look for non-standard signals from this beta-beam experiment. However, even if the precise value remains unknown at the time, considering the upper bound on θ_{13} one may tighten the constraints on the λ' couplings. Fig. 5.2 reflects the overall sensitivity of the event rate to the $\not{R}$ interactions obtained by letting all RPVSM couplings vary over their entire allowed ranges. In this subsection, we want to be more specific and ask how the event rate depends on any chosen λ' coupling.

At the outset, it may be worth recalling that the BELLE bound on $\tau \to \mu\pi^0$ [134] severely limits the products $\lambda'_{2m1}\lambda'_{3m1}$ and $\lambda'_{21m}\lambda'_{31m}$. Thus, R_{23} can be dropped in the effective neutrino mass matrix (see Eq. 5.6). If only λ'_{2m1} and/or λ'_{21m} (λ'_{3m1} and/or λ'_{31m}) is non-zero, then R_{22} (R_{33}) alone receives an RPVSM contribution. Both R_{22} and R_{33} can be simultaneously non-zero if λ'_{21m} and λ'_{3m1} (or λ'_{2m1} and λ'_{31m}) are non-zero at the same time.

In the light of this, we consider the situation where only one of the above $\not{R}$ coupling is non-zero. In such an event, only one of R_{22}, R_{33} is non-zero. The dependence of the number of events on a non-zero λ'_{331} or λ'_{2m1}, for a chosen $\sin^2 2\theta_{13}$, can be seen from Fig. 5.3. In this figure, we use the fact that if only one of these $\not{R}$ couplings is non-zero, it appears in the results through $|\lambda'|$. For the NH, the curves for λ'_{2m1}, for m = 2,3, are terminated at the maximum allowed value of 0.18. Fig. 5.3 can also be used for λ'_{321}, λ'_{31m} and λ'_{21m}, bearing in mind their different

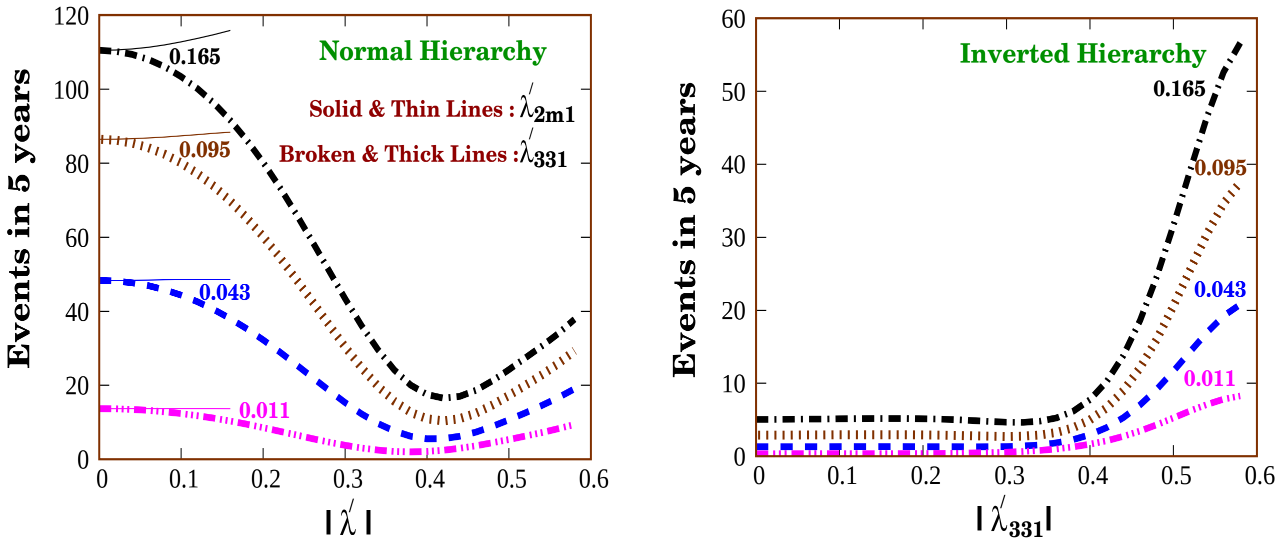

Figure 5.3: The number of events as a function of a coupling $|\lambda'|$, present singly, for the NH (left panel) and IH (right panel). The thick (thin) lines are for $|\lambda'_{331}|$ ($|\lambda'_{2m1}|$, m = 2, 3). The chosen $\sin^2 2\theta_{13}$ are indicated next to the curves.

upper bounds. For the IH, the number of events is small for λ'_{2m1} and λ'_{21m} and insensitive to the magnitude of the coupling. These are not shown. It is seen that for the NH there is a good chance to determine the $\not{R}$ couplings from the number of events. In fact, if the number of events is less than about 38 there is a disallowed region for $|\lambda'|$, while for larger numbers there is only an upper bound. For the IH, more than about five events will set a lower bound on the coupling.

5.4.3 Effect of λ

The λ couplings which can contribute in Eq. 5.10 have strong existing bounds [80] and their contribution to R is rather small in comparison to $\sqrt{2}G_F N_e$. Among them, the bounds $\lambda_{121} < 0.05$ and $\lambda_{321} < 0.07$ for $m_{\tilde{l}} = 100$ GeV are relatively less stringent [80]. We show their very modest impact in Fig. 5.4. It is clear from this figure that (a) the λ-type couplings cannot seriously deter the extraction of θ_{13} or the determination of the neutrino mass ordering, and (b) when θ_{13} is known in future it will still not be possible to constrain these couplings through long baseline experiments.

5.5 Conclusions

R-parity violating supersymmetry is among several extensions of the Standard Model crying out for experimental verification. The model has flavour diagonal and flavour changing neutral

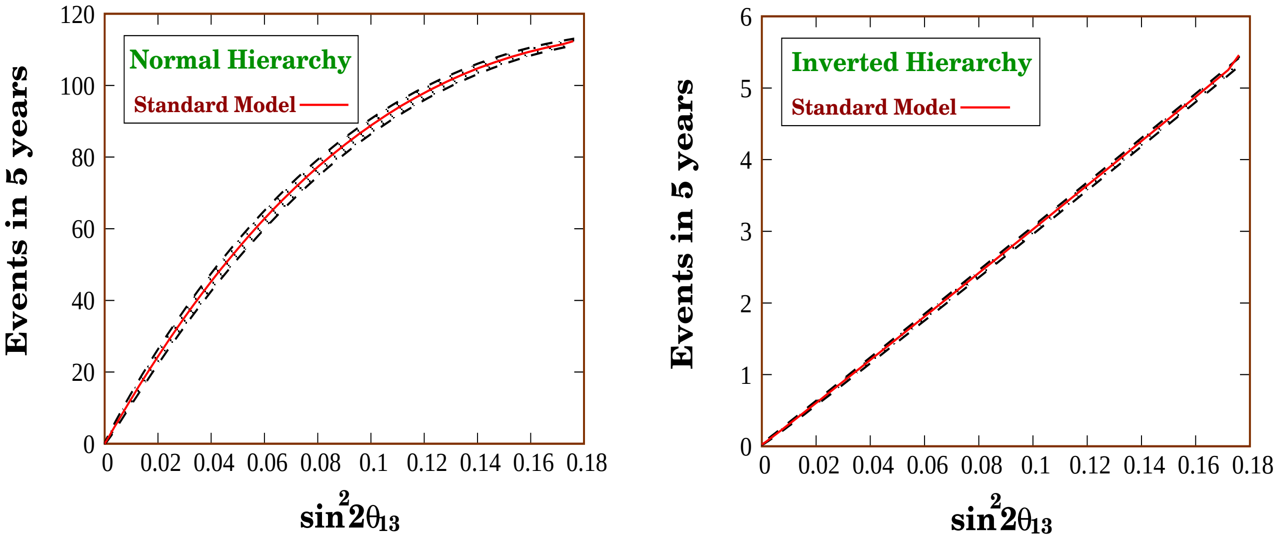

Figure 5.4: Number of muon events for the NH (left panel) and IH (right panel) as a function of $\sin^2 2\theta_{13}$ for a five years of ICAL@INO run. The solid lines correspond to the absence of any NSI. The hatched area is covered if the λ couplings are varied over their entire allowed range.

currents which can affect neutrino masses and mixing and can leave their imprints in long baseline experiments. This is the focus of this work.

We consider a beta-beam experiment with the source at CERN and the detector at INO. We find that the $\not{R}$ interactions may obstruct a clean extraction of the mixing angle θ_{13} or determination of the mass ordering unless the bounds on the λ' couplings are tightened. On the other hand, one might be able to see a clean signal of new physics. Here, the long baseline comes as a boon over experiments like MINOS which cover shorter distances. Two experiments of these contrasting types, taken together, can expose the presence of NSI like RPVSM.

There are other non-standard models [127] where four-fermion neutrino couplings with greater strength have been invoked. The signals we consider will be much enhanced in such cases.

Our results are presented for the CP conserving case. As θ_{13} is small, the CP violating effect is expected to be suppressed. We have checked this for the Standard Model, where the 'magic' nature of the baseline [97] also plays a role.

Finally, in this work we have restricted ourselves to a beta-beam neutrino source. Much the same could be done for antineutrinos as well; then the signs of all terms in R (see Eq. 5.6) will be reversed. It follows from Eq. 5.17 that θ_{13}^m can then be maximal only for the IH and as such more events are expected here than in the NH. Broadly, results similar to the ones presented here with neutrinos can be obtained with antineutrinos if NH is replaced by IH and *vice-versa*. In the next chapter, we will show that a small detector placed near a beta-beam storage ring can probe L violating interactions, as predicted by supersymmetric theories with R-parity non-conservation at the production and detection stages of neutrinos.

Chapter 6

Probing Lepton Number Violating Interactions with Beta-beam using a Near-Detector

6.1 Introduction

In the Standard Model, lepton number conservation is only accidental; the particle content and the requirement of renormalizability ensure that each lepton flavour number is conserved separately. However, non-zero neutrino masses, as indicated by recent neutrino oscillation experiments, have proved that the success of the Standard Model should be viewed as that of a low energy effective theory. It is not unreasonable to expect that in some extensions of the Standard Model, L conservation may not hold. Indeed, a Majorana mass term for the neutrinos violates total lepton number. The non-observation of direct L violation in the past experiments have put stringent constraints on some of these interactions. In this chapter we show that beta-beams and a nearby detector can be a good further probe of such interactions. For this work, the advantage of a 'near' detector is twofold.

1. **Firstly, due to the short base-length, neutrinos do not get much scope to oscillate before being detected, which could otherwise mimic signals of the L-violating ($\not{L}$) interactions.**
2. **The other obvious advantage is that a larger part of the beam can be picked up with a smaller detector.**

We consider placing a 5 kton cylindrical detector, aligned with the beam axis, within 1 km from the beta-beam storage ring. The $\not{L}$ interactions can lead to tau leptons in near-detector experiments in two ways. A ν_τ can be produced due to such interactions during beta-decay, yielding a τ through weak CC interactions in the detector. Alternatively, the electron neutrinos in the beam, produced through usual beta-decay, can undergo $\not{L}$ interactions with the detector,

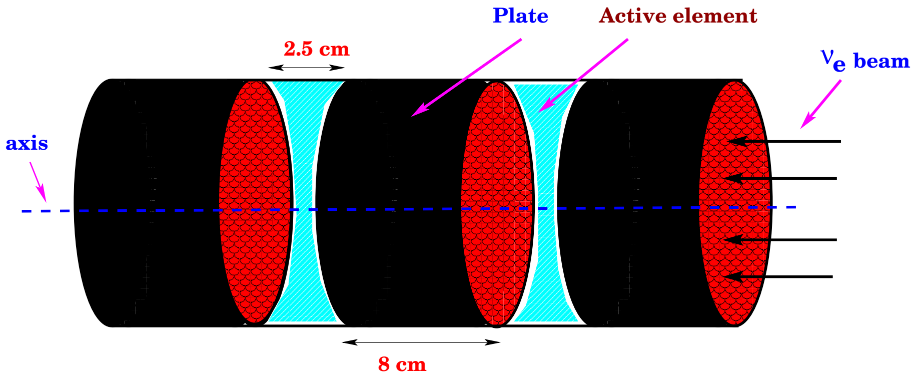

Figure 6.1: A schematic diagram of the proposed detector (a part only). The incoming ν_e beam may have a very small contamination of neutrinos of other flavours in the presence of lepton flavour violating interactions.

leading to tau leptons. The taus promptly decay, part of the time in a muonic channel. Iron calorimeters with active detector elements serve well for identifying these muons, which leave long tracks in the detector, and for filtering out backgrounds. We will also briefly comment on water Čerenkov and other detectors.

In the following section a brief account of the experimental set-up is presented. In section 6.3, $\not{L}$ interactions are discussed in the context of R-parity violating supersymmetric models [80, 137]. We stress how beta-decay can be affected in the presence of such interactions, yielding ν_τ in a few cases in place of the standard ν_e. The processes via which ν_e produce tau leptons in the detector are also described. The expected number of muon events from tau decay and the constraints ensuing in the event of their non-observation will be presented in section 6.4.

6.2 Beta-beam Flux at a Near-Detector

The choice of ions for a beta-beam is predicated by the intended physics. The low end-point energies (see Table 1.1) of the ^{6}He and ^{18}Ne ions restrict the energy reach of the beam; a threshold energy of 3.5 GeV is necessary to produce a τ-lepton from an incoming neutrino. Therefore, we will work with ^{8}B and ^{8}Li ions, offering higher end-point energies. We pick only the neutrino beam for our discussion.

The geometry of the beta-beam storage ring determines the neutrino flux at a near-detector. For a low-γ design, a 6880 m decay ring with straight sections of length ($\equiv S$) 2500 m each (36% useful length for ion decays) has been proposed. In such a configuration, $N_\beta = 1.1 \times 10^{18}$ useful decays (decays in one of the straight sections) per year can be obtained with ^{18}Ne ions. We have used this same luminosity for ^{8}B and higher γ. To settle these issues a dedicated study is on at CERN.

6.2.1 Detector Simulation Study

We consider a cylindrical 5 kton detector (as in Fig. 6.1) aligned with one of the straight sections of the storage ring. The detector is made of iron slabs (thickness 8 cm) with interleaved active detector elements (thickness 2.5 cm) such as resistive plate chambers (RPCs). The readouts from these RPCs will be concentric annular strips of small width with further segmentation to improve the position resolution. In this proposal, iron is the main content of the detector[1]. The thickness of the slabs ensures that electrons do not propagate in the detector. The signal muons are of sufficient energy to give rise to long tracks. To eliminate possible beam-induced backgrounds (see below) from pions produced in CC and NC processes, typically 6 to 13 hits (depending on the boost γ ranging from 250 to 450) are required of a putative muon track.

As noted earlier, the signature of new physics we consider is the appearance of prompt tau leptons which decay into muons with a branching fraction of 17.36% [138]. The tau production threshold is around 3.5 GeV. This is what necessitates the higher boost γ.

Backgrounds, other than those of the beam-induced variety discussed below, are controllable, as we now point out. A beam-off run will help make a first estimate of these backgrounds. Further, an important aspect of the beta-beam source is its capability of eliminating backgrounds through timing information. The beam itself will consist of bunches of typically 10ns size and the number of bunches will be chosen so as to ensure that the ratio of the active- to the dead-time is $\mathcal{O}(10^{-3})$. Backgrounds from other sources, namely, atmospheric neutrinos, spallation neutrons, cosmic rays, etc. can thus be largely rejected from the time-stamp of a recorded event. Even further reductions of the backgrounds of external origin can be envisioned through fiducial and directionality cuts.

Now let us turn our attention to the issue of beam-induced backgrounds caused by NC and CC interactions of unoscillated ν_e. Electrons produced through weak interactions by the incoming ν_e are quickly absorbed and do not leave any track. Formation of prompt muons through $\not{R}$ supersymmetric interactions is suppressed by strong bounds on the relevant couplings arising from limits on $\mu - e$ transitions in atoms [136]. However, the beta-beam neutrinos can produce pions along with other hadrons at the detector via CC and NC processes. They undergo strong interactions with the detector material and are quickly absorbed before they can decay. But as numerous pions are produced, it needs to be checked whether some of them can fake the signal.

We have checked our naïve expectations with a detector simulation study using GEANT [139] aided by NUANCE [140]. It is observed that for neutrino-nucleon interactions at energies interesting for our study, the produced lepton preferentially carries most of the energy of the incident neutrino. Moreover, pions are usually produced with multiplicity more than unity. Hence it is not unreasonable to expect that the pions will be less energetic compared to the taus produced via $\not{L}$ interactions and hence in detectors of this genre, it is possible to distinguish hadronic showers from a muon track.

---

[1] Lead may be an interesting alternative material to enhance the event rate.

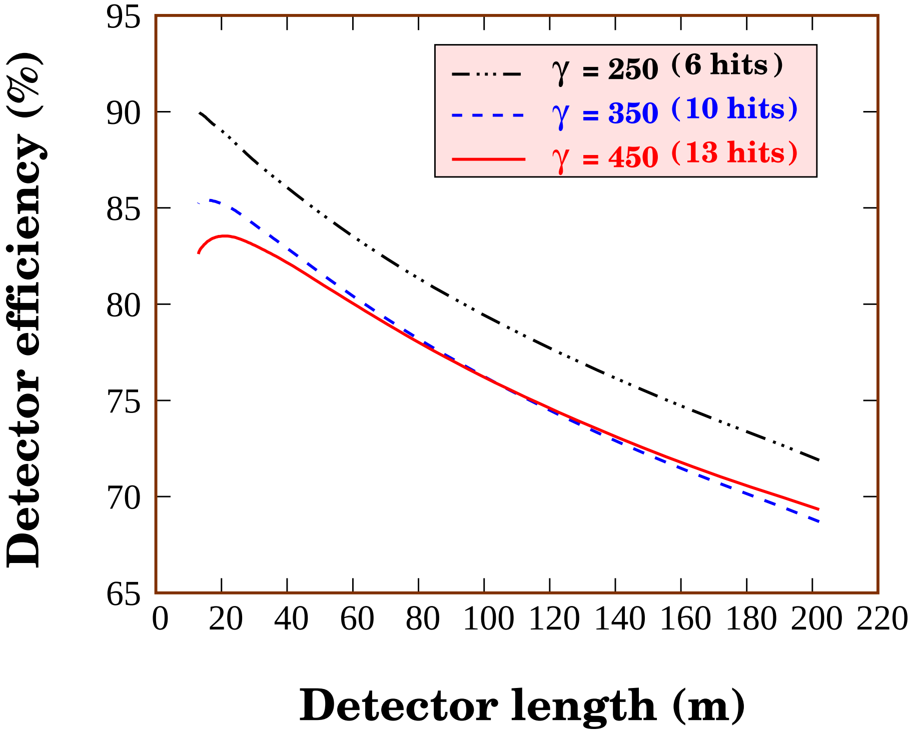

Figure 6.2: Detector efficiency for $\gamma = 250, 350, 450$. The corresponding cuts on muon hits used are 6, 10 and 13 respectively.

However, a conservative approach is followed in pion background estimation. Although pions do not leave behind a straight track like a muon, we still count the number of hits as a measure of the distance traversed by a pion. We impose a criterion of minimum number of hits to identify a track to be a muon one. We find from a simulation that, for $\gamma = 250/350/450$, imposing a cut of 6/10/13 hits will reduce the pion background at least to the 10^{-3} level.

The detector geometry plays a role in determining the signal efficiency after imposition of these cuts. Since the muons produced from boosted tau lepton decay carry transverse momentum, some of them may exit the detector through its sides, failing to satisfy the cuts. For a fixed detector mass (5 kton), a longer detector has a smaller cross-sectional area, resulting in a drop in the detector efficiency for the above reason. As the detector length increases from 20 m to 200 m, with our set of cuts, the efficiency factor reduces from 85% to 70% approximately, showing little dependence on γ (see Fig. 6.2).

6.2.2 Neutrino Fluxes

Neglecting small Coulomb interactions, the lab frame neutrino beta-beam flux (per unit solid angle per unit energy bin per unit time per unit length of the straight section) emitted at an angle θ with the beam axis is described by (see also Eq. 3.2)

$$\phi^{Near}(E,\theta) = \frac{1}{4\pi}\frac{g}{m_e^5 f}\frac{1}{\gamma(1-\beta\cos\theta)}(E_0 - E^*)E^{*2}\sqrt{(E_0-E^*)^2 - m_e^2}, \tag{6.1}$$

where $g \equiv N_\beta / S$ is the number of useful decays per unit time per unit length of the straight section.

To calculate the resulting number of events at a cylindrical near-detector of radius R and length D aligned with the beam axis it is necessary to integrate over the length S of the straight section of the storage ring and the volume of the detector. The event rate at a detector placed at a distance L from the storage ring is given by [141]

$$\frac{dN_{\not L}}{dt} = n\varepsilon \int_0^S dx \int_0^D d\ell \int_0^{\theta'} d\theta\, 2\pi \sin\theta \int_{E_{min}}^{E'} dE\, \phi^{Near}(E,\theta)\,\sigma(E), \tag{6.2}$$

where

$$\tan\theta^{'}(x,\ell) = \frac{R}{L+x+\ell} \quad \text{and} \quad E' = \frac{E_0 - m_e}{\gamma(1-\beta\cos\theta)}. \tag{6.3}$$

Here n represents the number of target nucleons per unit detector volume, ε is the detector efficiency as presented in Fig. 6.2, E_{min} denotes the tau production threshold, and $\sigma(E)$ stands for the neutrino-nucleon cross section. Note that the source of L-violation may lie either in $\phi^{Near}(E,\theta)$ (in case of $\not R$ beta-decay) or in $\sigma(E)$ (in case of $\not R$ tau production).

To help subsequent discussion, following [141], we rewrite the above formula isolating the geometry integrated total flux $\Phi(E;S,D,R,L)$ (per unit time per unit energy bin) falling on the detector and emitted from the whole length of the straight section as follows :

$$\frac{dN_{\not L}}{dt} = n\varepsilon \int_{E_{min}}^{E_{max}} dE\, \Phi(E;S,D,R,L)\,\sigma(E), \tag{6.4}$$

where

$$\Phi(E;S,D,R,L) = \int_0^S dx \int_0^D d\ell \int_0^{\theta'} d\theta\, 2\pi\sin\theta\, \phi^{Near}(E,\theta) \tag{6.5}$$

and

$$E_{max} = \frac{E_0 - m_e}{\gamma(1-\beta)}. \tag{6.6}$$

The beta-beam also involves a few small uncertainties which we neglect in our analysis. However for completeness, these are listed here :

- There exist different excited states of the daughter nuclei of the decaying ion, which additionally lead to small contributions to the spectra with different end-point energies.
- The ion beam has a finite transverse size. However, as this size varies [142] between only 3.0 cm to 5.1 cm, with an average of 4 cm (3σ), in both transverse directions inside the ring, the variation in flux at the detector due to this is negligible.

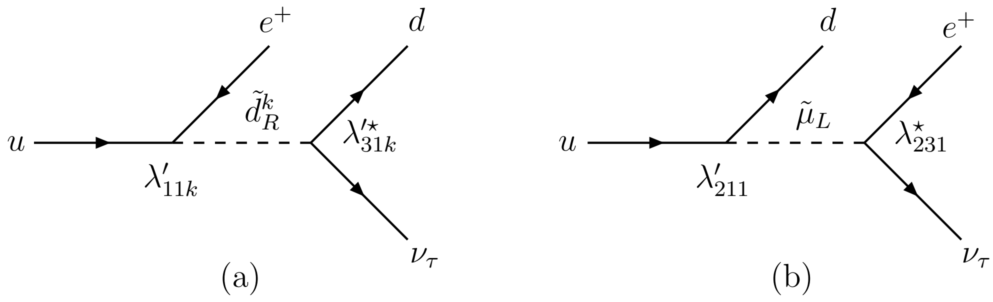

Figure 6.3: Feynman diagrams for $\not{R}_p$ interactions during beta-decay through (a) $\lambda'\lambda'$ and (b) $\lambda\lambda'$ type trilinear product couplings. Substantial event rates are obtained in (a) when $k = 2, 3$.

- The decaying ions may have small transverse momentum due to thermal fluctuations ($k_B T \sim 2.6 \times 10^{-3}$ eV), but this can be safely ignored in comparison with the end-point energy of the beta-decay.

6.3 $\not{R}_p$ Processes

A detailed description of the RPVSM [80, 137] containing renormalizable $\not{L}$ trilinear λ- and λ'-type couplings is given in section 5.2. To impose conservative upper bounds, we work in a minimal $\not{R}_p$ framework where only a pair of such couplings are assumed to be non-zero at a time. For a near-detector, $\not{R}_p$ interactions can come into effect in two ways as described in the following subsections.

6.3.1 ν_τ Production in Beta-decay via $\not{R}_p$ Interactions

$\not{R}_p$ interactions can drive beta-decay producing ν_τ instead of ν_e. ν_τ so produced give rise to τ leptons in the detector which may decay in the leptonic channel producing muons.

Simultaneous presence of λ'_{31k} and λ'_{11k} couplings (see Fig. 6.3(a)) can be responsible for producing a ν_τ in beta-decay. Of these, λ'_{111} is tightly constrained from neutrinoless double beta-decay [143]. But the upper bound on the combination $|\lambda'^{\star}_{31k}\lambda'_{11k}|, k = 2, 3$ is rather relaxed; a limit of $2.4\times 10^{-3}(\tilde{m}/100 \text{ GeV})^2$, $\tilde{m}$ being a common sfermion mass, follows from $\tau^- \longrightarrow e^-\rho^0$ [136, 138]. The corresponding decay amplitude can be written as,

$$M_{\not{R}_p}(u \longrightarrow d e^+ \nu_\tau) \quad = \quad \frac{\lambda'^{\star}_{31k}\lambda'_{11k}}{2(\hat{s} - \tilde{m}^2)}\,[\bar{u}_{\nu_\tau}\gamma_\mu P_L u_e]\,[\bar{u}_d \gamma^\mu P_L u_u]. \tag{6.7}$$

Alternatively, ν_τ can be produced in beta-decay if another combination of $\not{R}_p$ couplings $\lambda^{\star}_{i31}\lambda'_{i11}$ ($i =$ 1, 2) is non-zero (see Fig. 6.3(b)). As mentioned earlier, λ'_{111} is severely constrained. The combination $|\lambda^{\star}_{231}\lambda'_{211}|$ is bounded from above by $1.6 \times 10^{-3}(\tilde{m}/100 \text{ GeV})^2$ arising from the

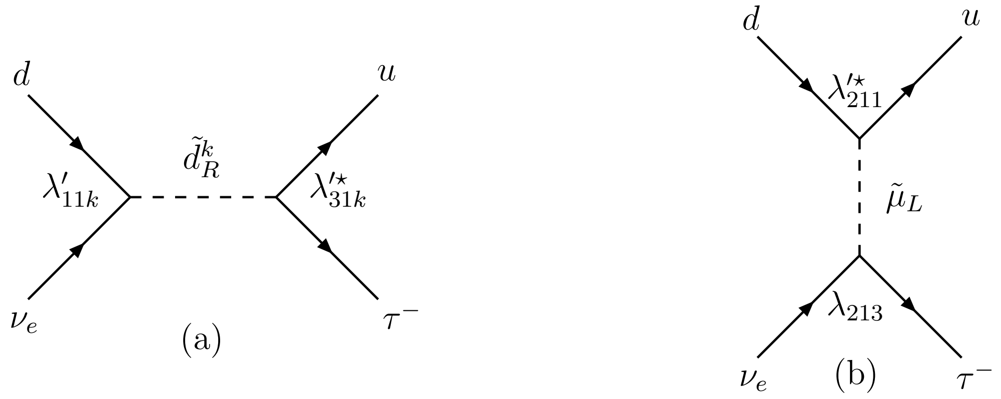

Figure 6.4: Feynman diagrams for tau production from an incoming ν_e beta-beam through (a) $\lambda'\lambda'$ and (b) $\lambda\lambda'$ type trilinear product couplings. Substantial event rates are obtained in (a) when $k = 2, 3$.

decay channel $\tau^- \to e^-\eta^0$ [136, 138], which is not too small to produce an observable effect. The corresponding decay amplitude is given by,

$$M_{\not L}(u \longrightarrow d e^+ \nu_\tau) \;=\; \frac{\lambda^\star_{231}\lambda'_{211}}{(\hat{t} - \tilde{m}^2)}\,[\bar{u}_{\nu_\tau} P_R\, u_e]\,[\bar{u}_d P_L u_u]. \tag{6.8}$$

6.3.2 τ production from ν_e via $\not R$ Interactions

ν_e produced through ordinary beta-decay driven by weak interactions can undergo $\not R$ interactions with the detector producing τ which subsequently decay into muons.

Simultaneous presence of λ'_{31k} and λ'_{11k} couplings can give rise to τ^- in the final state from an incoming ν_e beta-beam (see Fig. 6.4(a)). The amplitude for the corresponding s-channel diagram can be written, after a Fierz transformation, as

$$M_{\not L}(\nu_e\, d \longrightarrow \tau^-\, u) \;=\; \frac{\lambda'^\star_{31k}\lambda'_{11k}}{2(\hat{s} - \tilde{m}^2)}\,[\bar{u}_\tau \gamma_\mu P_L u_{\nu_e}]\,[\bar{u}_u \gamma^\mu P_L u_d]. \tag{6.9}$$

An alternative channel of tau production from an incoming ν_e beam exists (see Fig. 6.4(b)) if a particular combination of the λ and λ' couplings $\lambda_{i13}\lambda'^\star_{i11}$ (i = 2, 3) is non-zero. Here again, λ_{313} is severely constrained from neutrinoless double beta-decay experiments [144]. An upper bound of $1.6 \times 10^{-3}(\tilde{m}/100\ \text{GeV})^2$ applies to the combination $|\lambda_{213}\lambda'^\star_{211}|$, from the decay channel $\tau^- \to e^-\eta^0$ [136, 138]. The amplitude for this t-channel process is

$$M_{\not L}(\nu_e\, d \longrightarrow \tau^-\, u) \;=\; \frac{\lambda_{213}\lambda'^\star_{211}}{(\hat{t} - \tilde{m}^2)}\,[\bar{u}_\tau P_L u_{\nu_e}]\,[\bar{u}_u P_R u_d]. \tag{6.10}$$

In what follows, we categorize the above two kinds of diagrams (a) and (b) in Figs. 6.3 and 6.4 as $\lambda'\lambda'$ and $\lambda\lambda'$ processes, respectively.

Note that, if $|\lambda'^{\star}_{31k}\lambda'_{11k}|,\ k = 2, 3$ is non-zero, tau leptons can be produced at the detector either due to $\not{R}$ interactions affecting beta-decay or due to $\not{R}$ interactions of a ν_e with the detector material. These two equal contributions add in the total rate of tau production.

However, for the $\lambda\lambda'$ process, we see that the $\not{R}$ combinations $|\lambda^{\star}_{231}\lambda'_{211}|$ (which drive the $\not{R}$ beta-decay) and $|\lambda_{213}\lambda'^{\star}_{211}|$ (which is responsible for producing a tau from an incoming ν_e in the detector) are different. As we are following the strategy of taking only two $\not{R}$ couplings non-zero at a time, these contributions, which are of the same magnitude, cannot be present at the same time.

In passing, a few comments are in order :

- In both the diagrams of Fig. 6.4, the incoming ν_e can interact with a $\bar{u}$ quark from the sea to produce a tau. Due to the smallness of the corresponding parton distribution function, this contribution is suppressed but we do include it in the numerical evaluations.
- Here we should mention that the FCNC process, $K^+ \to \pi^+\nu\bar{\nu}$ [145] puts stringent bounds on all the λ' couplings. However, these are basis dependent and hence can be evaded.
- As already noted, the non-observation of the process $\mu \to e\ (Ti)$ severely restricts [80, 136] the possibility of emitting a ν_μ in beta-decay and direct production of muons from an incoming ν_e beam.
- Since the beta-beam energy is ∼ a few GeV, the expected event rate will be essentially independent of the sfermion mass as the bounds on λ, λ' scale with $(\tilde{m}/100\ \mathrm{GeV})^2$.

At this energy range it is important to consider contributions from deep-inelastic, quasi-elastic, and single-pion production channels. To estimate the $\not{R}$ deep-inelastic scattering cross section, we have used CTEQ4LQ parton distributions [146]. $\not{R}$ quasi-elastic scattering and single-pion production cross sections have been evaluated from the corresponding Standard Model cross sections[2] [119, 147] by a rescaling of the couplings. It is noticed that, as Eq. 6.10 is not reducible to a Standard Model-like $(V-A)\otimes(V-A)$ Lorentz structure, in calculating deep-inelastic cross section a factor $\sim 1/3$ appears from polar integration compared to that for Eq. 6.9. For the $\lambda\lambda'$ process we have adopted the same suppression factor for the Standard Model quasi-elastic and single-pion production cross sections as well. Conservatively, we assume that a similar suppression also applies to the case of $\not{R}$ beta-decay. It bears stressing that the effect of the tau mass is felt on the neutrino-nucleus cross section throughout the energy range beyond the τ-threshold and this is included in the analysis.

6.4 Results

A near-detector set-up is qualitatively different from a far-detector as in the former case the storage ring and the detector really 'sees' each other and relative geometric considerations are of much relevance. The observed number of events in a given period of time depends on the choice of the radioactive ion, the boost factor γ and the details of the set-up (which include storage ring parameters, detector configuration and the short base-length between them). As alluded to earlier, the maximum γ available is limited by the storage ring configuration. With a view to optimizing the set-up, the essential inputs are summarized as follows :

---

[2] These cross sections include all nuclear effects for an iron target.

- **Storage Ring Parameters :**

  Total length 6880 m, length of a straight section, $S = 2500$ m, number of beta-decays in the straight section, $N_\beta = 1.1 \times 10^{18}$ per year.

- **Detector Configuration :**

  The detector material is[3] iron ($\rho = 7.87$ gm/cm^3). A detector of mass 5 kton is considered. For a given material, this fixes the length of the detector as the radius is changed. It varies from 202.13 m to 12.63 m as the radius ranges over 1 m to 4 m.

- **Base-length :**

  Results are presented for three representative values of the distance of the detector from the storage ring, $L = 200$ m, 500 m, 1 km.

- **Boost factor γ :**

  The tau production threshold (3.5 GeV) calls for a high γ. We consider $\gamma = 250, 350, 450$ for ^{8}B and as large as 800 for ^{18}Ne with fixed N_β.

The high collimation achievable in the beta-beams encourages the choice of a detector of cylindrical shape coaxial with the storage ring straight section. As γ increases, the $\not{R}$ event rates increase for the following reasons :

1. an increasingly larger part of the beam falls onto the detector,
2. more neutrinos have enough energy to produce a tau lepton,
3. with the more energetic neutrinos the cross section is larger.

The first two effects are demonstrated by Fig. 6.5. The geometry integrated flux, Φ, as defined in Eq. 6.5, represents the beta-beam neutrino flux spectrum falling onto the detector per unit time. It is seen that as γ increases, the total area under the curve also increases, illustrating the first effect. The area under the curves on the right side of the vertical line (the threshold) also increases with γ, in conformity with the second expectation. For a high γ the beam should saturate. However, with the γ used in Fig. 6.5 this is not evident due to the enormous length of the straight section of the storage ring. To collimate the flux emanating from the rear part of the ring a very high γ will be needed.

---

[3] Brief comments are made about a water Čerenkov detector in section 6.4.2.

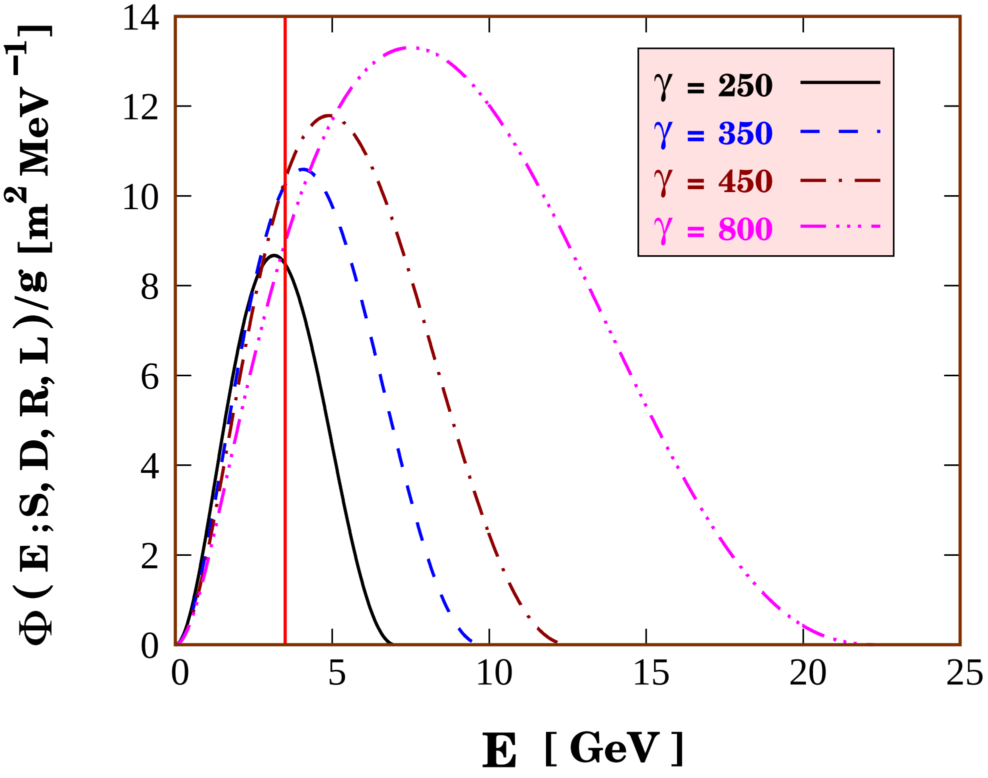

Figure 6.5: Geometry integrated flux $\Phi(E;S,D,R,L)/g$ taking ^{8}B as the decaying ion is plotted against neutrino energy E for different γ for $S = 2500$ m, $D = 202.13$ m, $R = 1$ m, and $L = 200$ m. The vertical line at 3.5 GeV indicates the tau production threshold energy.

As geometry plays a crucial role in optimizing the near-detector set-up, we study the detector length dependence of the expected number of $\not R$ events for different base-lengths and different γ. We consider the contribution coming from the two options – the $\lambda'\lambda'$ and $\lambda\lambda'$ processes – in different panels for every figure, assuming the $\not R$ coupling constants saturate present experimental upper limits.

6.4.1 Choice of Ion Source and Detector

The choice of ^{8}B as the ion source provides the most attractive option due to its high end-point energy. Iron calorimeters are preferred for the smaller size and significant background removal.

To get a glimpse of the number of events one might expect in such a set-up, let us present the following estimate. A 5 kton Fe detector of radius 1 m (length 202.13 m) placed at a distance 200 m from the decay ring can give rise to 92 (24) muon events via the $\lambda'\lambda'$ ($\lambda\lambda'$) process in 5 years for[4] $\gamma = 250$.

---

[4] The corresponding numbers for $\gamma = 350$ are 421 (103).

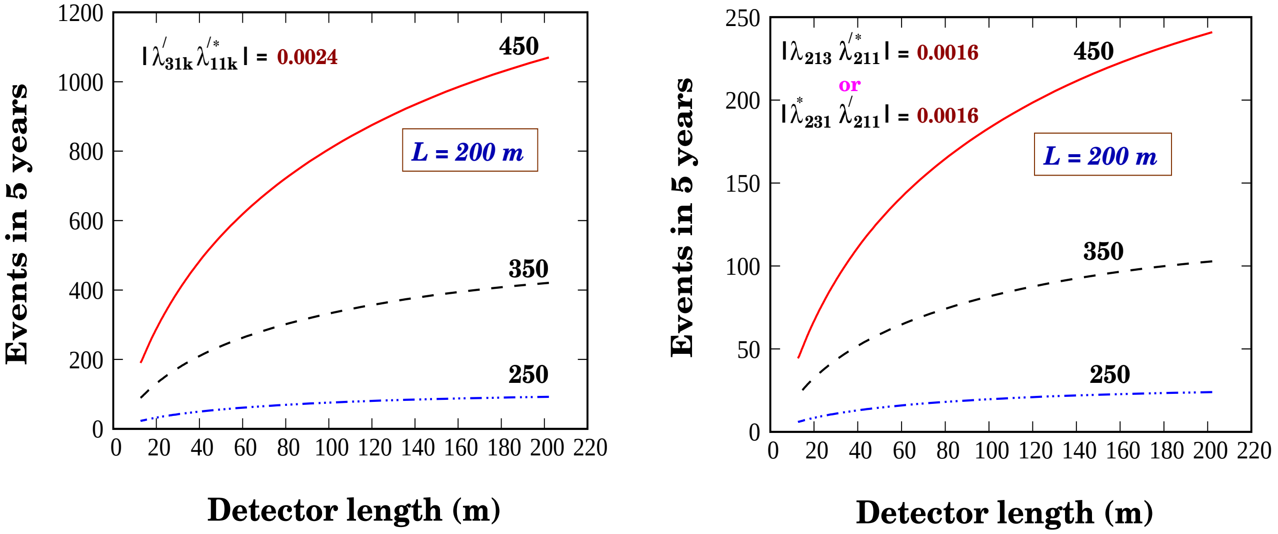

Figure 6.6: Expected number of $\not{R}$ muon events in five years for a 5 kton iron detector vs. the detector length for $\gamma = 250$, 350, and 450 for ^{8}B beta-beam flux. The left (right) panel is for the $\lambda'\lambda'$ ($\lambda\lambda'$) driven process. $k = 2, 3$.

In Fig. 6.6 we exhibit the γ dependence of the expected number of muon events over a five-year period for a fixed base-length of 200 m. Collimation plays a role as is demonstrated by the increase in the number of events for higher γ. As expected, a long detector serves better as it provides more opportunity for a neutrino interaction to occur. However, this increase with the length is not linear; a part of the beam is lost due to the concomitant decrease in the radius (to keep the total mass fixed at 5 kton). In addition, with the increase in detector length as the detector efficiency decreases, the increase in the rates is also somewhat restricted.

It is also of interest to study the base-length dependence of the number of events. The beam spreads with an increase in the base-length, reducing the effective flux hitting the detector. This causes a fall in the number of events (other parameters remaining the same) as shown in Fig. 6.7. It is interesting to note that the increase in the number of events with increase in the length of the detector gets severely diluted at larger base-lengths.

While presenting the expected number of events we assumed the $\not{R}$ couplings saturate the present experimental upper bounds. In case less or even no events are seen, the existing limits on the combinations $|\lambda'^{\star}_{31k}\lambda'_{11k}|, k = 2, 3$, $|\lambda^{\star}_{231}\lambda'_{211}|$ and $|\lambda_{213}\lambda'^{\star}_{211}|$ will be improved. Choosing the minimum number of non-zero $\not{R}$ couplings, one can put conservative upper bounds. In Fig. 6.8 we show the bounds – the region above the curves are disallowed – achievable in the case of 'no-show'[5]. It is seen that to put stringent bounds it is necessary to go for a higher γ and a longer detector.

---

[5] At 95% C.L. this corresponds to not more than 3 events.

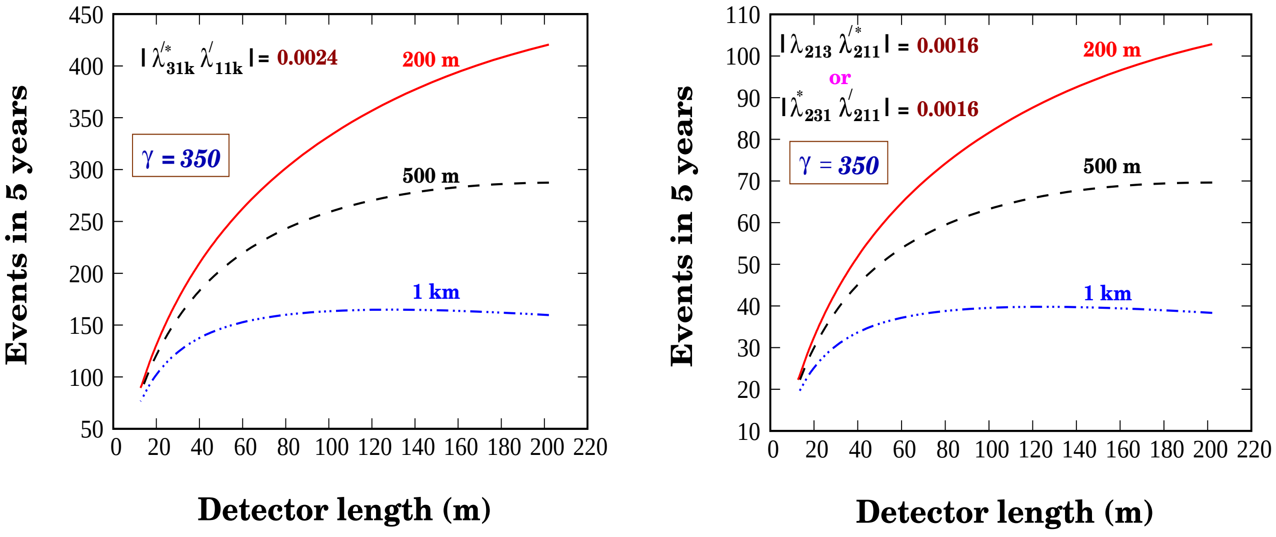

Figure 6.7: Muon signal event rate in 5 years as a function of the detector (Fe) length for three different choices of base-length have been shown for ^{8}B beta-beam flux. The left (right) panel corresponds to the $\lambda'\lambda'$ ($\lambda\lambda'$) driven process. $k = 2, 3$.

6.4.2 Alternative Set-ups

Although so far we have presented results with ^{8}B as the beta-beam source, ^{18}Ne is the most discussed decaying ion in the literature. As mentioned earlier, due to the smaller end-point energy of ^{18}Ne, a high γ is required to cross the τ threshold. Fig. 6.9 depicts the variation in the expected event rate with detector length for ^{18}Ne with $\gamma = 800$ using a 5 kton iron calorimeter. We see that due to high γ for ^{18}Ne, the beam is so collimated that the event rates increase almost linearly with increasing detector length in contrast to the ^{8}B case we have presented. However even in such an extreme scenario, where we use the same storage ring configuration to reach such a high γ, the expected event rates are comparable to that in the ^{8}B case. Hence we conclude that ^{8}B is preferred to ^{18}Ne in exploring lepton number violating signatures with beta-beams.

The use of water Čerenkov detectors with good capability of muon-electron separation and moderate efficiency of neutral current rejection may be an interesting option to see the signals of new physics and to normalize the incoming flux. The disadvantage of this set-up turns out to be the huge background. Consider a 5 kton water Čerenkov detector with radius 2.5 m at a distance 200 m from the decay ring. In five years, this will lead to 45 (12) muon events from τ-lepton decay for $\lambda'\lambda'$ ($\lambda\lambda'$) driven processes from an incoming ^{8}B ν_e beam accelerated with a γ of 250 and with a muon detection threshold of 200 MeV. For the same configuration and duration, one expects roughly 10^8 pions produced from charged and neutral current interactions of the ν_e beam. Muons produced from π decay will thus completely swamp the signal.

The number of signal events may be increased by designing a very long water detector with small radius though this could be technologically challenging. In any case, the background

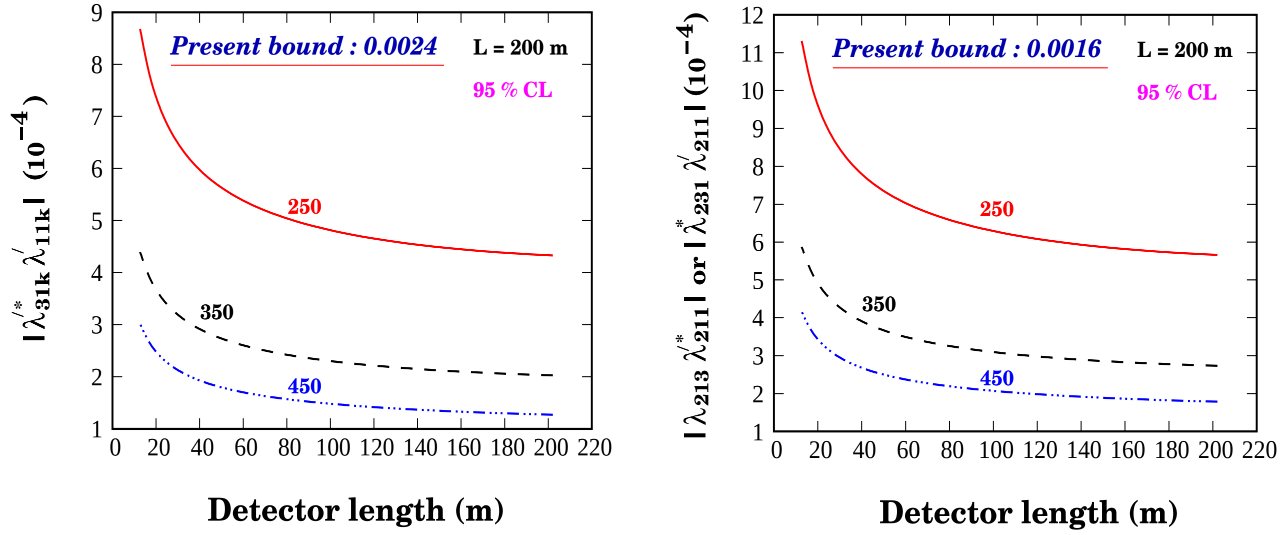

Figure 6.8: Bounds on $|\lambda'^{\star}_{31k}\lambda'_{11k}|$, $k = 2, 3$ ($|\lambda^{\star}_{231}\lambda'_{211}|$ or $|\lambda_{213}\lambda'^{\star}_{211}|$) versus detector size at 95% C.L. for zero observed events is depicted in left (right) panel for $\gamma = 250, 350, 450$. The bounds scale as $(\tilde{m}/100\ \text{GeV})^2$. The results are for a five-year run for a 5 kton Fe detector placed at a distance of 200 m from the front end of the storage ring for ^{8}B beta-beam flux.

events will continue to be very high. So, this option also does not hold much promise. The basic problem of high backgrounds, avoided in the Fe detector, will also plague totally active scintillator based detectors.

6.5 Discussion and Conclusion

Beta-beam experiments may be sensitive to the $\not{L}$ interactions. In the previous chapter it was shown that $\not{R}$ interactions can interfere with pure oscillation signals in long-baseline beta-beam experiments. In this chapter we explore a complementary scenario. It has been proposed that to probe such interactions, an iron calorimeter detector placed close to the storage ring holds promise as it provides essentially a neutrino oscillation free environment. In particular, the combination of a 5 kton cylindrical iron detector placed within a distance of 200 m to 1 km from the decay ring and a neutrino beam from an ^{8}B ion source with γ in the range 250 to 450, running for 5 years is well-suited in this regard. We have examined the impact of non-trivial design details of such a near-detector setup.

At production, low energy beta-decay experiments may get contaminated by tau neutrinos through $\not{R}$ interactions. We show that, this contamination, though small, can be probed using the above set-up. $\not{R}$ interactions can also play a role in such an experiment during the interactions of the beta-beam electron neutrinos with the detector.

It is interesting to explore if $\not{R}$ interactions can affect beta-beam experiments in other ways. For example, we have checked that the impact of these interactions on the μ detection cross

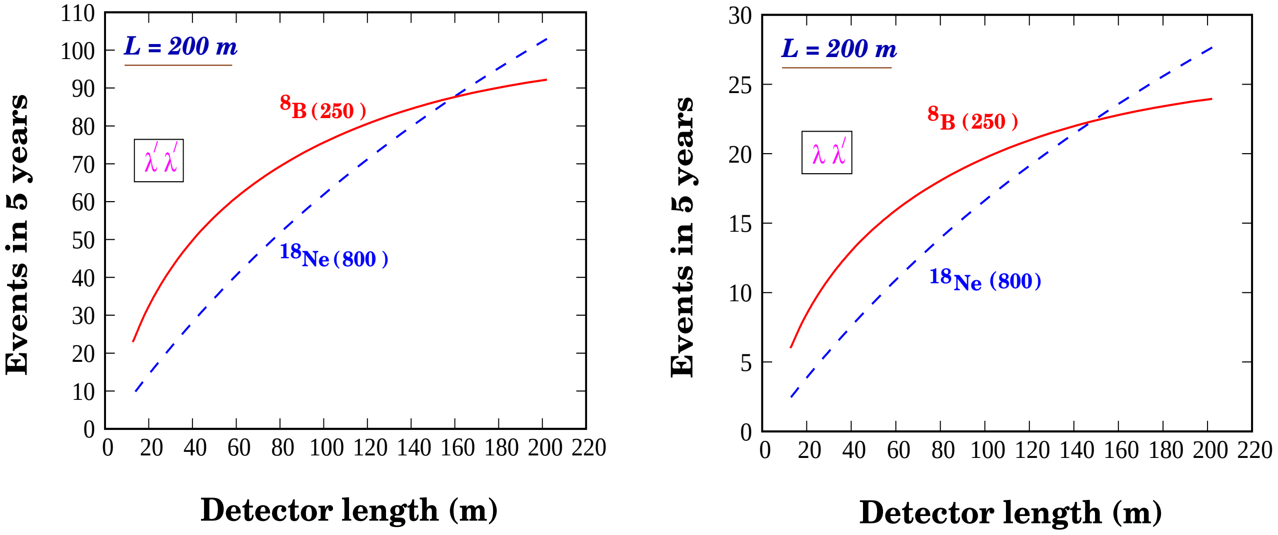

Figure 6.9: Comparison of the muon signal event rates as a function of the detector length for a 5 kton iron calorimeter placed at a distance of 200 m from the storage ring for $\gamma = 800$ (250) with ^{18}Ne (^{8}B). The left and right panels correspond to $\lambda'\lambda'$ and $\lambda\lambda'$ driven processes, respectively.

section is insignificant. As mentioned earlier, ν_μ may be produced in beta-decay through $\not{R}$ interactions but this also is severely suppressed as the corresponding couplings have stringent upper limits.

Results are presented for a neutrino beam. Antineutrino beams can also be produced using ^{8}Li or ^{6}He as sources. In fact, a storage ring design may allow both beams to be present simultaneously. The expected event rates for antineutrinos are of similar order as for the neutrinos.

In conclusion, we find a near-detector setup can be useful for exploring lepton number violating interactions with beta-beams. It may allow us to put stringent bounds on some of these couplings. In the next chapter, we will present a summary of this doctoral work.

Chapter 7

Summary and Conclusions

Neutrino physics is traversing through an exciting phase with lots of new data making this field more interesting. There is an excellent progress in our understanding of the neutrinos over the last ten years or so, thanks to the experiments on neutrino oscillations which confirm the fact that neutrinos have a tiny, but non-zero, mass quite against the expectations of our best theory - the Standard Model. We have now a rough picture of the parameters governing three-flavour oscillations and we are all set to move into the precision regime. There is no doubt that the use of artificial neutrino sources is mandatory in the era of high precision experiments. In this direction the beta-beam is a recently proposed technique of producing a pure, intense and collimated beam of ν_e or $\bar{\nu}_e$ through the beta-decay of completely ionized radioactive ions. My thesis sheds light on the importance of beta-beams in probing some unknown territories in the field of neutrino physics.

We started with a brief description of neutrino properties in the first half of chapter 1 and then we took a glance at the fascinating journey of discovery into one of Nature's most impalpable particles - the neutrino which is the main theme of this thesis. In the second half of chapter 1 we focused on the main sources of neutrinos.

The first part of chapter 2 dealt with a basic introduction to the quantum mechanics of neutrino oscillation in vacuum under both two and three flavour frameworks. Then the importance of matter effects in neutrino oscillations was discussed. In the second half of chapter 2 we took a look at our present understanding of neutrino parameters and we identified the major unknowns in the neutrino sector. Finally we closed chapter 2 by giving a brief note on the future neutrino road-map based on long baseline experiments.

In chapter 3 we expounded in detail the physics reach of an experimental set-up in which the proposed large magnetized iron detector at the INO would serve as the far detector for a beta-beam. If this pure ν_e and/or $\bar{\nu}_e$ beam is shot from some source location like CERN such that the source-detector distance $L \simeq 7500$ km, the impact of the CP phase δ_{CP} on the oscillation probability and associated parameter correlation and degeneracies are almost negligible. This "magical" long baseline beta-beam experiment would have unprecedented sensitivity to the neutrino mass hierarchy and θ_{13}, two of the missing ingredients needed for our understanding of the neutrino sector. With Lorentz boost $\gamma = 650$ and irrespective of the true value of δ_{CP}, the neutrino mass hierarchy could be determined at 3σ C.L. if $\sin^2 2\theta_{13}(\text{true}) > 5.6 \times 10^{-4}$ and we can expect an unambiguous signal for θ_{13} at 3σ C.L. if $\sin^2 2\theta_{13}(\text{true}) > 5.1 \times 10^{-4}$ independent of the true neutrino mass ordering.

In chapter 4 we showed that the earth matter effects in the $\nu_{\rm e} \rightarrow \nu_{\rm e}$ survival probability can be used to cleanly determine the third leptonic mixing angle θ_{13} and the sign of the atmospheric neutrino mass squared difference, Δm^2_{31}, using a beta-beam as a ν_e source.

In chapter 5 we discussed possible new physics scenarios with a beta-beam neutrino source and made a strong physics case for these high-precision experiments. Long baseline neutrino oscillation experiments may well emerge as test beds for neutrino interactions as are present in R-parity violating supersymmetry. We showed that flavour diagonal and flavour changing neutral currents arising therefrom prominently impact a neutrino beta-beam experiment with the source at CERN and the detector at the proposed India-based Neutrino Observatory. These interactions may preclude any improvement of the present limit on θ_{13} and cloud the hierarchy determination unless the upper bounds on $\not{R}$ couplings, particularly λ', become significantly tighter. If $\not{R}$ interactions are independently established then from the event rate a lower bound on θ_{13} may be set. It has been shown that there is scope to see a clear signal of non-standard FCNC and FDNC interactions, particularly in the IH scenario and also sometimes for the NH. In favourable cases, it may be possible to set lower and upper bounds on λ' couplings. FCNC and FDNC interactions due to λ type $\not{R}$ couplings are unimportant.

A detector placed near a beta-beam storage ring can probe $\not{L}$ interactions, as predicted by supersymmetric theories with R-parity non-conservation. This issue has been discussed in great detail in chapter 6. In the presence of $\not{R}$ interactions, ν_τ can be produced during beta-decay leading to tau leptons through weak interactions. Alternatively, electron neutrinos from beta-decay of radioactive ions can produce tau leptons in a nearby detector through these interactions. The muons from the decay of these tau leptons can be readily identified in a small iron calorimeter detector and will signal violation of R-parity.

The study of neutrinos has always landed up with lots of surprises. So we can expect further surprises in store and, obviously, beta-beams can play a leading role in this direction. This doctoral work is an effort to judge the expected performance of a beta-beam neutrino source in the future progress of neutrino physics and also for the hunt for signals of non-standard new physics. We hope that this work will provide a boost to the detailed and thorough R&D of the novel beta-beam neutrino source in future.

Bibliography

[1] W. Pauli, *letter sent to the Tubingen conference*, 4th December, 1930.

[2] F. Reines and C. L. Cowan, Phys. Rev. **113** (1959) 273.

[3] K. Hirata *et al.* [KAMIOKANDE-II Collaboration], Phys. Rev. Lett. **58**, 1490 (1987).

[4] R. M. Bionta *et al.*, Phys. Rev. Lett. **58**, 1494 (1987).

[5] G. G. Raffelt, Ann. Rev. Nucl. Part. Sci. **49**, 163 (1999).

[6] Y. Fukuda *et al.* [Super-Kamiokande Collaboration], Phys. Rev. Lett. **81**, 1562 (1998).

[7] Q. R. Ahmad *et al.* [SNO Collaboration], Phys. Rev. Lett. **89**, 011301 (2002).

[8] K. Eguchi *et al.*, [KamLAND Collaboration], Phys. Rev. Lett. **90**, 021802 (2003); T. Araki *et al.*, [KamLAND Collaboration], Phys. Rev. Lett. **94**, 081801 (2005); S. Abe *et al.* [KamLAND Collaboration], arXiv:0801.4589 [hep-ex].

[9] I. Shimizu, talk at 10th International Conference on Topics in Astroparticle and Underground Physics, TAUP 2007.

[10] L. Wolfenstein, Phys. Rev. D **17**, 2369 (1978); L. Wolfenstein, Phys. Rev. D **20**, 2634 (1979); S. P. Mikheev and A. Y. Smirnov, Sov. J. Nucl. Phys. **42**, 913 (1985) [Yad. Fiz. **42**, 1441 (1985)]; S. P. Mikheev and A. Y. Smirnov, Nuovo Cim. C **9**, 17 (1986).

[11] M. H. Ahn *et al.* [K2K Collaboration], Phys. Rev. Lett. **90**, 041801 (2003).

[12] B. Pontecorvo, Sov. Phys. JETP **26**, 984 (1968) [Zh. Eksp. Teor. Fiz. **53**, 1717 (1967)].

[13] V. N. Gribov and B. Pontecorvo, Phys. Lett. B **28**, 493 (1969).

[14] M. C. Gonzalez-Garcia and M. Maltoni, Phys. Rept. **460**, 1 (2008).

[15] A. Strumia and F. Vissani, arXiv:hep-ph/0606054.

[16] J. N. Bahcall, A. M. Serenelli and S. Basu, Astrophys. J. **621**, L85 (2005).

[17] B. T. Cleveland *et al.*, Astrophys. J. **496**, 505 (1998); J. N. Abdurashitov *et al.* [SAGE Collaboration], J. Exp. Theor. Phys. **95**, 181 (2002) [Zh. Eksp. Teor. Fiz. **122**, 211 (2002)]; W. Hampel *et al.* [GALLEX Collaboration], Phys. Lett. B **447**, 127 (1999).

[18] C. Arpesella *et al.* [Borexino Collaboration], Phys. Lett. B **658**, 101 (2008).

[19] S. Fukuda *et al.* [Super-Kamiokande Collaboration], Phys. Lett. B **539**, 179 (2002);

[20] B. Aharmim *et al.* [SNO Collaboration], Phys. Rev. C **72**, 055502 (2005);

[21] C. V. Achar *et al.*, Phys. Lett. **18**, 196 (1965).

[22] F. Reines *et al.*, Phys. Rev. Lett. **15**, 429 (1965).

[23] M. C. Sanchez *et al.* [Soudan 2 Collaboration], Phys. Rev. D **68**, 113004 (2003).

[24] M. Ambrosio *et al.* [MACRO Collaboration], Phys. Lett. B **517**, 59 (2001).

[25] M. S. Athar *et al.* [INO Collaboration], A Report of the INO Feasibility Study, http://www.imsc.res.in/∼ino/OpenReports/INOReport.pdf.

[26] T. Araki *et al.*, Nature **436**, 499 (2005).

[27] F. Halzen, arXiv:astro-ph/0506248.

[28] G. Zacek *et al.* [CALTECH-SIN-TUM Collaboration], Phys. Rev. D **34**, 2621 (1986).

[29] G. S. Vidyakin *et al.*, JETP Lett. **59**, 390 (1994) [Pisma Zh. Eksp. Teor. Fiz. **59**, 364 (1994)].

[30] Y. Declais *et al.*, Nucl. Phys. B **434**, 503 (1995).

[31] M. Apollonio *et al.* [CHOOZ Collaboration], Phys. Lett. B **466**, 415 (1999).

[32] A. Piepke [Palo Verde Collaboration], Prog. Part. Nucl. Phys. **48**, 113 (2002).

[33] M. Apollonio *et al.*, arXiv:hep-ph/0210192.

[34] A. Guglielmi, M. Mezzetto, P. Migliozzi and F. Terranova, arXiv:hep-ph/0508034.

[35] A. Para and M. Szleper, arXiv:hep-ex/0110032.

[36] D. G. Michael *et al.*, [MINOS Collaboration], arXiv:hep-ex/0607088.

[37] M. Guler *et al.* [OPERA Collaboration], CERN-SPSC-2000-028 (2000).

[38] P. Aprili *et al.* [ICARUS Collaboration], CERN-SPSC-2002-027 (2002).

[39] Y. Itow *et al.*, arXiv:hep-ex/0106019.

[40] D. S. Ayres *et al.* [NOvA Collaboration], arXiv:hep-ex/0503053.

[41] S. Geer, Phys. Rev. D **57**, 6989 (1998) [Erratum-ibid. D **59**, 039903 (1999)].

[42] R. Edgecock, J. Phys. G **29**, 1601 (2003).

[43] M. M. Alsharoa *et al.* [Muon Collider/Neutrino Factory Collaboration], Phys. Rev. ST Accel. Beams **6**, 081001 (2003); N. Holtkamp and S. Geer, Feasibility study of neutrino source based on muon storage ring, ICFA Beam Dyn. Newslett. **21**, 37 (2000); S. Ozaki *et al.*, Feasibility study-II of a muon-based neutrino source, (2001), BNL-52623; P. Gruber (ed.) *et al.*, The study of a European neutrino factory complex, (2002), CERN-PS-2002-080-PP.

[44] A. Donini, D. Meloni and P. Migliozzi, Nucl. Phys. B **646**, 321 (2002); D. Autiero *et al.*, Eur. Phys. J. C **33**, 243 (2004).

[45] P. Zucchelli, Phys. Lett. B **532**, 166 (2002).

[46] For a recent review see C. Volpe, J. Phys. G **34**, R1 (2007).

[47] J. E. Campagne *et al.*, JHEP **0704**, 003 (2007).

[48] S. K. Agarwalla, A. Raychaudhuri and A. Samanta, Phys. Lett. B **629**, 33 (2005).

[49] S. K. Agarwalla, S. Choubey and A. Raychaudhuri, Nucl. Phys. B **771**, 1 (2007).

[50] S. K. Agarwalla, S. Choubey and A. Raychaudhuri, Nucl. Phys. B **798**, 124 (2008).

[51] S. K. Agarwalla, S. Choubey, S. Goswami and A. Raychaudhuri, Phys. Rev. D **75**, 097302 (2007).

[52] S. K. Agarwalla, S. Choubey, A. Raychaudhuri and W. Winter, JHEP **0806**, 090 (2008).

[53] S. K. Agarwalla, S. Choubey and A. Raychaudhuri, arXiv:0804.3007 [hep-ph].

[54] R. Adhikari, S. K. Agarwalla and A. Raychaudhuri, Phys. Lett. B **642**, 111 (2006).

[55] S. K. Agarwalla, S. Rakshit and A. Raychaudhuri, Phys. Lett. B **647**, 380 (2007).

[56] S. K. Agarwalla, S. Choubey and A. Raychaudhuri, AIP Conf. Proc. **981**, 84 (2008);

[57] S. K. Agarwalla, S. Choubey and A. Raychaudhuri, AIP Conf. Proc. **939**, 265 (2007); S. K. Agarwalla, Talk at NuFact08, Valencia-Spain, June 30 - July 5, 2008, http://ific.uv.es/nufact08/

[58] M. Mezzetto, J. Phys. G **29**, 1771 (2003) [arXiv:hep-ex/0302007]. M. Mezzetto, Nucl. Phys. Proc. Suppl. **143**, 309 (2005). M. Mezzetto, Nucl. Phys. Proc. Suppl. **155**, 214 (2006);

[59] A. Donini, E. Fernandez-Martinez, P. Migliozzi, S. Rigolin and L. Scotto Lavina, Nucl. Phys. B **710**, 402 (2005).

[60] A. Donini, E. Fernandez, P. Migliozzi, S. Rigolin, L. Scotto Lavina, T. Tabarelli de Fatis and F. Terranova, arXiv:hep-ph/0511134; A. Donini, E. Fernandez-Martinez, P. Migliozzi, S. Rigolin, L. Scotto Lavina, T. Tabarelli de Fatis and F. Terranova, Eur. Phys. J. C **48**, 787 (2006).

[61] P. Coloma, A. Donini, E. Fernandez-Martinez and J. Lopez-Pavon, JHEP **0805**, 050 (2008).

[62] J. Burguet-Castell, D. Casper, E. Couce, J. J. Gómez-Cadenas and P. Hernandez, Nucl. Phys. B **725**, 306 (2005).

[63] J. Burguet-Castell, D. Casper, J. J. Gómez-Cadenas, P. Hernandez and F. Sanchez, Nucl. Phys. B **695**, 217 (2004).

[64] A. Jansson, O. Mena, S. Parke and N. Saoulidou, arXiv:0711.1075 [hep-ph].

[65] P. Huber, M. Lindner, M. Rolinec and W. Winter, Phys. Rev. D **73**, 053002 (2006).

[66] A. Donini and E. Fernandez-Martinez, Phys. Lett. B **641**, 432 (2006).

[67] D. Meloni, O. Mena, C. Orme, S. Palomares-Ruiz and S. Pascoli, arXiv:0802.0255 [hep-ph].

[68] M. Lindroos, arXiv:physics/0312042; M. Lindroos, Nucl. Phys. Proc. Suppl. **155**, 48 (2006).

[69] http://beta-beam.web.cern.ch/beta%2Dbeam/

[70] J. Bouchez, M. Lindroos and M. Mezzetto, AIP Conf. Proc. **721**, 37 (2004).

[71] The ISS Physics Working Group, arXiv:0710.4947 [hep-ph]. http://www.hep.ph.ic.ac.uk/iss/

[72] C. Rubbia, A. Ferrari, Y. Kadi and V. Vlachoudis, Nucl. Instrum. Meth. A **568**, 475 (2006); C. Rubbia, arXiv:hep-ph/0609235.

[73] Y. Mori, Nucl. Instrum. Meth. A **562**, 591 (2006).

[74] L. P. Ekstrom and R. B. Firestone, WWW Table of Radioactive Isotopes, database version 2/28/99 from URL http://ie.lbl.gov/toi/

[75] B. Autin, R. C. Fernow, S. Machida and D. A. Harris, J. Phys. G **29**, 1637 (2003); F. Terranova, A. Marotta, P. Migliozzi and M. Spinetti, Eur. Phys. J. C **38**, 69 (2004).

[76] M. Apollonio *et al.*, Eur. Phys. J. C **27**, 331 (2003).

[77] E. Aliu *et al.* [K2K Collaboration], Phys. Rev. Lett. **94**, 081802 (2005).

[78] M. C. Gonzalez-Garcia and M. Maltoni, arXiv:0704.1800 [hep-ph]; M. Maltoni, T. Schwetz, M. A. Tortola and J. W. F. Valle, New J. Phys. **6**, 122 (2004), hep-ph/0405172 v6; S. Choubey, arXiv:hep-ph/0509217; S. Goswami, Int. J. Mod. Phys. A **21**, 1901 (2006); A. Bandyopadhyay, S. Choubey, S. Goswami, S. T. Petcov and D. P. Roy, Phys. Lett. B **608**, 115 (2005); G. L. Fogli *et al.*, Prog. Part. Nucl. Phys. **57**, 742 (2006); G. L. Fogli *et al.*, Phys. Rev. D **75**, 053001 (2007).

[79] The plenary talk of Thomas Schwetz at Nufact07, Okayama, Japan.

[80] R. Barbier *et al.*, Phys. Rept. **420**, 1 (2005); M. Chemtob, Prog. Part. Nucl. Phys. **54**, 71 (2005).

[81] B. Pontecorvo, Sov. Phys. JETP **6**, 429 (1957) [Zh. Eksp. Teor. Fiz. **33**, 549 (1957)]; Sov. Phys. JETP **7**, 172 (1958) [Zh. Eksp. Teor. Fiz. **34**, 247 (1957)].

[82] Z. Maki, M. Nakagawa and S. Sakata, Prog. Theor. Phys. **28**, 870 (1962).

[83] L. L. Chau and W. Y. Keung, Phys. Rev. Lett. **53**, 1802 (1984); C. Jarlskog, Z. Phys. C **29**, 491 (1985); C. Jarlskog, Phys. Rev. D **35**, 1685 (1987).

[84] Y. Ashie *et al.* [Super-Kamiokande Collaboration], Phys. Rev. D **71**, 112005 (2005).

[85] J. Dunkley *et al.* [WMAP Collaboration], arXiv:0803.0586 [astro-ph]; E. Komatsu *et al.* [WMAP Collaboration], arXiv:0803.0547 [astro-ph]; C. L. Reichardt *et al.*, arXiv:0801.1491 [astro-ph]; C. Dickinson *et al.*, Mon. Not. Roy. Astron. Soc. **353**, 732 (2004); A. C. S. Readhead *et al.*, Astrophys. J. **609**, 498 (2004); C. J. MacTavish *et al.*, Astrophys. J. **647**, 799 (2006); W. L. Freedman *et al.* [HST Collaboration], Astrophys. J. **553**, 47 (2001); P. Astier *et al.* [The SNLS Collaboration], Astron. Astrophys. **447**, 31 (2006); D. J. Eisenstein *et al.* [SDSS Collaboration], Astrophys. J. **633**, 560 (2005); U. Seljak, A. Slosar and P. McDonald, JCAP **0610**, 014 (2006); P. McDonald *et al.* [SDSS Collaboration], Astrophys. J. **635**, 761 (2005). G. L. Fogli *et al.*, arXiv:0805.2517 [hep-ph].

[86] S. Pascoli, S. T. Petcov and T. Schwetz, Nucl. Phys. B **734**, 24 (2006); S. Choubey and W. Rodejohann, Phys. Rev. D **72**, 033016 (2005).

[87] V. D. Barger, K. Whisnant, S. Pakvasa and R. J. N. Phillips, Phys. Rev. D **22**, 2718 (1980).

[88] A. Cervera, A. Donini, M. B. Gavela, J. J. Gómez-Cadenas, P. Hernandez, O. Mena and S. Rigolin, Nucl. Phys. B **579**, 17 (2000) [Erratum-ibid. B **593**, 731 (2001)].

[89] F. Ardellier *et al.*, arXiv:hep-ex/0405032; F. Ardellier *et al.* [Double Chooz Collaboration], arXiv:hep-ex/0606025.

[90] P. Huber, M. Lindner, M. Rolinec, T. Schwetz and W. Winter, Phys. Rev. D **70**, 073014 (2004) and references therein.

[91] P. Huber, M. Mezzetto and T. Schwetz, JHEP **0803**, 021 (2008).

[92] C. Volpe, J. Phys. G **30**, L1 (2004).

[93] J. Burguet-Castell, M. B. Gavela, J. J. Gómez-Cadenas, P. Hernandez and O. Mena, Nucl. Phys. B **608**, 301 (2001).

[94] H. Minakata and H. Nunokawa, JHEP **0110**, 001 (2001).

[95] G. L. Fogli and E. Lisi, Phys. Rev. D **54**, 3667 (1996).

[96] V. Barger, D. Marfatia and K. Whisnant, Phys. Rev. D **65**, 073023 (2002).

[97] P. Huber and W. Winter, Phys. Rev. D **68**, 037301 (2003).

[98] A. Y. Smirnov, arXiv:hep-ph/0610198.

[99] M. Freund, M. Lindner, S. T. Petcov and A. Romanino, Nucl. Phys. B **578**, 27 (2000).

[100] P. Huber, M. Lindner, M. Rolinec and W. Winter, Phys. Rev. D **74**, 073003 (2006).

[101] B. Autin *et al.*, J. Phys. G **29**, 1785 (2003) [arXiv:physics/0306106].

[102] M. Freund, P. Huber and M. Lindner, Nucl. Phys. B **615**, 331 (2001).

[103] W. Winter, Phys. Lett. B **613**, 67 (2005).

[104] H. Minakata and H. Nunokawa, Phys. Lett. B **413**, 369 (1997); V. Barger, D. Marfatia and K. Whisnant, Phys. Rev. D **66**, 053007 (2002); V. Barger, D. Marfatia and K. Whisnant, Phys. Lett. B **560**, 75 (2003); O. Mena and S. J. Parke, Phys. Rev. D **70**, 093011 (2004); O. Mena Requejo, S. Palomares-Ruiz and S. Pascoli, Phys. Rev. D **72**, 053002 (2005); M. Ishitsuka, T. Kajita, H. Minakata and H. Nunokawa, Phys. Rev. D **72**, 033003 (2005); K. Hagiwara, N. Okamura and K. i. Senda, Phys. Rev. D **76**, 093002 (2007).

[105] P. Huber, M. Lindner and W. Winter, Nucl. Phys. B **645**, 3 (2002); P. Huber, M. Lindner and W. Winter, Nucl. Phys. B **654**, 3 (2003).

[106] A. Donini, D. Meloni and P. Migliozzi, Nucl. Phys. B **646**, 321 (2002); D. Autiero *et al.*, Eur. Phys. J. C **33**, 243 (2004).

[107] A. Donini, E. Fernandez-Martinez and S. Rigolin, Phys. Lett. B **621**, 276 (2005); A. Donini, E. Fernandez-Martinez, D. Meloni and S. Rigolin, Nucl. Phys. B **743**, 41 (2006).

[108] P. Huber, M. Maltoni and T. Schwetz, Phys. Rev. D **71**, 053006 (2005);

[109] P. Huber, M. Lindner, T. Schwetz and W. Winter, Nucl. Phys. B **665**, 487 (2003).

[110] A. M. Dziewonski and D. L. Anderson, Phys. Earth Planet. Interiors **25**, 297 (1981);
S. V. Panasyuk, Reference Earth Model (REM) webpage,
http://cfauves5.harvrd.edu/lana/rem/index.html.

[111] A. Takamura and K. Kimura, JHEP **0601**, 053 (2006).

[112] See for example, A. Bandyopadhyay, S. Choubey, S. Goswami and S. T. Petcov, Phys. Rev. D **72**, 033013 (2005); J. N. Bahcall and C. Pena-Garay, JHEP **0311**, 004 (2003).

[113] R. J. Geller and T. Hara, Nucl. Instrum. Meth. A **503**, 187 (2001).

[114] M. C. Banuls, G. Barenboim and J. Bernabeu, Phys. Lett. B **513**, 391 (2001).

[115] R. Gandhi, P. Ghoshal, S. Goswami, P. Mehta and S. Uma Sankar, Phys. Rev. Lett. **94**, 051801 (2005).

[116] R. Gandhi, P. Ghoshal, S. Goswami, P. Mehta and S. Uma Sankar, Phys. Rev. D **73**, 053001 (2006).

[117] P. Huber, J. Kopp, M. Lindner, M. Rolinec and W. Winter, Comput. Phys. Commun. **177**, 432 (2007); P. Huber, M. Lindner and W. Winter, Comput. Phys. Commun. **167**, 195 (2005).

[118] M. D. Messier, PhD thesis, UMI-99-23965.

[119] E. A. Paschos and J. Y. Yu, Phys. Rev. D **65**, 033002 (2002).

[120] A. Cervera, talk at NuFact07.

[121] K. Anderson *et al.*, arXiv:hep-ex/0402041.

[122] E. K. Akhmedov *et al.*, JHEP **0404**, 078 (2004).

[123] C. K. Jung, AIP Conf. Proc. **533**, 29 (2000).

[124] Y. Itow *et al.*, arXiv:hep-ex/0106019.

[125] A. de Bellefon *et al.*, arXiv:hep-ex/0607026.

[126] G. L. Fogli, E. Lisi, D. Montanino and G. Scioscia, Phys. Rev. D **55**, 4385 (1997); E. K. Akhmedov, A. Dighe, P. Lipari and A. Y. Smirnov, Nucl. Phys. B **542**, 3 (1999); D. Choudhury and A. Datta, JHEP **0507**, 058 (2005); D. Indumathi and M. V. N. Murthy, Phys. Rev. D **71**, 013001 (2005); S. Choubey and P. Roy, Phys. Rev. D **73**, 013006 (2006).

[127] S. Davidson, C. Pena-Garay, N. Rius and A. Santamaria, JHEP **0303**, 011 (2003).

[128] N. Kitazawa, H. Sugiyama and O. Yasuda, arXiv:hep-ph/0606013; A. Friedland and C. Lunardini, Phys. Rev. D **74**, 033012 (2006).

[129] J. W. F. Valle, Phys. Lett. B **199**, 432 (1987); M. M. Guzzo, A. Masiero and S. T. Petcov, Phys. Lett. B **260**, 154 (1991); E. Roulet, Phys. Rev. D **44**, 935 (1991); V. D. Barger, R. J. N. Phillips and K. Whisnant, Phys. Rev. D **44**, 1629 (1991); S. Bergmann, Nucl. Phys. B **515**, 363 (1998); E. Ma and P. Roy, Phys. Rev. Lett. **80**, 4637 (1998); S. Bergmann, M. M. Guzzo, P. C. de Holanda, P. I. Krastev and H. Nunokawa, Phys. Rev. D **62**, 073001 (2000); M. Guzzo, P. C. de Holanda, M. Maltoni, H. Nunokawa, M. A. Tortola and J. W. F. Valle, Nucl. Phys. B **629**, 479 (2002); R. Adhikari, A. Sil and A. Raychaudhuri, Eur. Phys. J. C **25**, 125 (2002).

[130] M. C. Gonzalez-Garcia *et al.*, Phys. Rev. Lett. **82**, 3202 (1999); G. L. Fogli, E. Lisi, A. Marrone and G. Scioscia, Phys. Rev. D **60**, 053006 (1999); S. Bergmann, Y. Grossman and D. M. Pierce, Phys. Rev. D **61**, 053005 (2000); N. Fornengo, M. Maltoni, R. T. Bayo and J. W. F. Valle, Phys. Rev. D **65**, 013010 (2002).

[131] P. Huber and J. W. F. Valle, Phys. Lett. B **523**, 151 (2001); A. Datta, R. Gandhi, B. Mukhopadhyaya and P. Mehta, Phys. Rev. D **64**, 015011 (2001); A. Bueno, M. Campanelli, M. Laveder, J. Rico and A. Rubbia, JHEP **0106**, 032 (2001).

[132] P. Huber, T. Schwetz and J. W. F. Valle, Phys. Rev. D **66**, 013006 (2002).

[133] L. E. Ibáñez and G. G. Ross, Nucl. Phys. B **368**, 3 (1992); H. K. Dreiner, C. Luhn and M. Thormeier, Phys. Rev. D **73**, 075007 (2006).

[134] Y. Enari *et al.* [Belle Collaboration], Phys. Lett. B **622**, 218 (2005).

[135] W. j. Li, Y. d. Yang and X. d. Zhang, Phys. Rev. D **73**, 073005 (2006).

[136] P. Wintz (on behalf of SINDRUM II Collaboration), Proc. of the 14th Intl. Conf. on Particles and Nuclei (PANIC96), (World Scientific 1997, Eds. C. E. Carlson and J. J. Domingo) 458; J. E. Kim, P. Ko and D. G. Lee, Phys. Rev. D **56**, 100 (1997).

[137] P. Fayet, Phys. Lett. B **69**, 489 (1977); G. R. Farrar and P. Fayet, Phys. Lett. B **76**, 575 (1978).

[138] K. Hagiwara *et al.* [Particle Data Group], Phys. Rev. D **66**, 010001 (2002).

[139] GEANT - Detector Description and Simulation Tool CERN Program Library Long Writeup W5013.

[140] D. Casper, Nucl. Phys. Proc. Suppl. **112**, 161 (2002).

[141] J. Serreau and C. Volpe, Phys. Rev. C **70**, 055502 (2004).

[142] Adrian Fabich, private communication.

[143] M. Hirsch, H. V. Klapdor-Kleingrothaus and S. G. Kovalenko, Nucl. Phys. Proc. Suppl. **62**, 224 (1998).

[144] G. Bhattacharyya, H. V. Klapdor-Kleingrothaus and H. Päs, Phys. Lett. B **463**, 77 (1999).

[145] K. Agashe and M. Graesser, Phys. Rev. D **54**, 4445 (1996).

[146] H. L. Lai *et al.*, Phys. Rev. D **55**, 1280 (1997).

[147] E. A. Paschos, L. Pasquali and J. Y. Yu, Nucl. Phys. B **588**, 263 (2000).

List of Publications

1. **Exploration prospects of a long baseline beta beam neutrino experiment with an iron calorimeter detector**,
   Sanjib Kumar Agarwalla, Amitava Raychaudhuri and Abhijit Samanta,
   Phys. Lett. B **629**, 33 (2005); hep-ph/0505015.

2. **Can R-parity violating supersymmetry be seen in long baseline beta-beam experiments?**,
   Rathin Adhikari, Sanjib Kumar Agarwalla and Amitava Raychaudhuri,
   Phys. Lett. B **642**, 111 (2006); hep-ph/0608034.

3. **Probing Lepton Number Violating Interactions with Beta-beams**,
   Sanjib Kumar Agarwalla, Subhendu Rakshit, and Amitava Raychaudhuri,
   Phys. Lett. B **647**, 380 (2007); hep-ph/0609252.

4. **Neutrino mass hierarchy and θ_{13} with a magic baseline beta-beam experiment**,
   Sanjib Kumar Agarwalla, Sandhya Choubey, and Amitava Raychaudhuri,
   Nucl. Phys. B **771**, 1 (2007); hep-ph/0610333.

5. **Neutrino Mixings and Leptonic CP Violation from CKM Matrix and Majorana Phases**,
   S.K. Agarwalla, M.K. Parida, R.N. Mohapatra, and G. Rajasekaran,
   Phys. Rev. D **75**, 033007 (2007); hep-ph/0610333.

6. **Neutrino parameters from matter effects in the ν_e survival probability at long baselines**,
   Sanjib Kumar Agarwalla, Sandhya Choubey, Srubabati Goswami and Amitava Raychaudhuri,
   Phys. Rev. D **75**, 097302 (2007); hep-ph/0611233.

7. **Unraveling neutrino parameters with a magical beta-beam experiment at INO**,
   Sanjib Kumar Agarwalla, Sandhya Choubey, and Amitava Raychaudhuri,
   Nucl. Phys. B **798**, 124 (2008); arXiv:0711.1459 [hep-ph].

8. **Optimizing the greenfield Beta-beam**,
   Sanjib Kumar Agarwalla, Sandhya Choubey, Amitava Raychaudhuri and Walter Winter,
   JHEP **0806**, 090 (2008); arXiv:0802.3621 [hep-ex].

9. **Exceptional Sensitivity to Neutrino Parameters with a Two Baseline Beta-Beam Set-up**,
   Sanjib Kumar Agarwalla, Sandhya Choubey and Amitava Raychaudhuri,
   Accepted in Nucl. Phys. B; arXiv:0804.3007 [hep-ph].